6. SITE 1003[1]

Shipboard Scientific Party[2]

HOLE 1003A

Position: 24°32.746′N, 79°15.642′W

Start hole: 1815 hr, 23 February 1996

End hole: 2200 hr, 24 February 1996

Time on hole: 1 day, 3 hr, 45 min

Seafloor (drill pipe measurement from rig floor, mbrf): 492.5

Total depth (drill pipe measurement from rig floor, mbrf): 738.2

Distance between rig floor and sea level (m): 11.1

Water depth (drill pipe measurement from sea level, m): 481.4

Penetration (mbsf): 245.7

Coring totals:
Type: APC; No: 10; Cored: 87.2 m; Recovered: 91.3%
Type: XCB; No: 17; Cored: 158.5 m; Recovered: 31.2%

Formation:
Unit I: 0–162.1 mbsf; Holocene to late Pliocene
Unlithified to partially lithified mudstones and wackestones with intercalations of packstones and floatstones
Unit II: 162.1–236.5 mbsf; late Pliocene to early Pliocene
Bioturbated, partially lithified wackestones with skeletal debris, slightly dolomitized in upper part decreasing downhole

HOLE 1003B

Position: 24°32.759′N, 79°15.648′W

Start hole: 2200 hr, 24 February 1996

End hole: 1545 hr, 26 February 1996

Time on hole: 1 day, 17 hr, 45 min

Seafloor (drill pipe measurement from rig floor, mbrf): 494.5

Total depth (drill pipe measurement from rig floor, mbrf): 1036.1

Distance between rig floor and sea level (m): 11.2

Water depth (drill pipe measurement from sea level, m): 483.3

Penetration (mbsf): 541.6

Coring totals:
Type: APC; No: 9; Cored: 79.0 m; Recovered: 80.7%
Type: XCB; No: 48; Cored: 462.6. m; Recovered: 26.7%

Formation:
Unit I: 0–156.2 mbsf; Holocene to late Pliocene
Unlithified to partially lithified mudstones and wackestones with intercalations of floatstones
Unit II: 165.9–360.01 mbsf; late Pliocene to early Pliocene
Bioturbated, partially lithified wackestones with skeletal debris, slightly dolomitized in upper part decreasing downhole
Unit III: 368.2–492.7 mbsf; early Pliocene to late Miocene
Gray to light gray wackestones and intercalations of coarse-grained packstones to grainstones that decrease downhole

HOLE 1003C

Position: 24°32.763′N, 79°15.65′W

Start hole: 1545 hr, 26 February 1996

End hole: 1457 hr, 6 March 1996

Time on hole: 8 days, 23 hr, 12 min

Seafloor (drill pipe measurement from rig floor, mbrf): 494.5

Total depth (drill pipe measurement from rig floor, mbrf): 1794.5

Distance between rig floor and sea level (m): 11.2

Water depth (drill pipe measurement from sea level, m): 483.3

Penetration (mbsf): 1300.0

Coring totals:
Type: RCB; No: 88; Cored: 845.8 m; Recovered: 44.7%

Formation:
Unit III: 406–492.7 mbsf; early Pliocene to late Miocene
Gray to light gray wackestones with intercalations of coarse-grained packstones to grainstones that decrease downhole
Unit IV: 492.7–643 mbsf; late Miocene to middle Miocene
Packstones and grainstones grading downhole into wackestones and mudstones
Unit V: 646–915.8 mbsf; middle Miocene
Alternation of greenish-gray wackestones and grayish bioclastic packstones and floatstones
Unit VI: 915.8–1151.38 mbsf; middle Miocene to early Miocene
Wackestones interbedded with packstones and floatstones
Unit VII: 1151.63–1296.4; early Miocene
Gray to greenish gray wackestones with minor, thin beds of black to dark gray siltstones

HOLE 1003D

Position: 24°32.7628′N, 79°15.6498′W

Start hole: 0530 hr, 20 March 1996

End hole: 0730 hr, 24 March 1996

Time on hole: 4 days, 1 hr, 55 min

Seafloor (drill pipe measurement from rig floor, mbrf): 494.5

Total depth (drill pipe measurement from rig floor, mbrf): 1547.2

Distance between rig floor and sea level (m): 11.6

Water depth (drill pipe measurement from sea level, m): 482.9

Penetration (mbsf): 1052.7

Coring totals: None: drilled for logging only

[1]Eberli, G.P., Swart, P.K., Malone, M.J., et al., 1997. *Proc. ODP, Init. Repts.*, 166: College Station, TX (Ocean Drilling Program).
[2]Shipboard Scientific Party is given in the list preceding the Table of Contents.

Previous Chapter Table of Contents Next Chapter

Principal results: Site 1003 is one of five sites along a transect connecting the shallow bank with the deeper water areas. Site 1003 is located on the middle slope of the prograding western margin of the Great Bahama Bank approximately 4 km from the platform edge and 12.6 km from the borehole Clino that was drilled on the banktop from a self-propelled jack-up barge.

A thick Neogene section (1300 m) was cored at Site 1003. The strata consist of a series of mixed pelagic and bank-derived carbonates, with a carbonate content of 92%–97%. In the lower sections, a small amount of fine-grained siliciclastics is admixed in the pelagic intervals. Variations in carbonate accumulation rate indicate pulses of bank-top derived sedimentation. Foraminifer and nannofossil biostratigraphy yielded precise ages of the lithologic units. The good recovery throughout the entire section (overall over 40%), and the abundance of biostratigraphic markers, have made it possible to accomplish two of the primary sea-level objectives. It is possible to define the ages of the Neogene sequence boundaries and to test their consistency with ages determined in the boreholes Unda and Clino, and to retrieve the sedimentary record of the middle to lower slope portions of the prograding sequences. Within the Miocene section there are four hiatuses, ranging from 4 to 1 m.y. in duration. Comparison of the lithostratigraphic unit boundaries and the biostratigraphic breaks displays a good correlation to seismic sequence boundaries previously identified in the prograding slope section. The biostratigraphic data confirm the ages of the upper Miocene to Pleistocene sequences that were determined in the two core borings Unda and Clino on the shallow bank.

Chemistry from interstitial waters yielded interesting depth profiles with abrupt changes across stratigraphic boundaries. These data, in conjunction with the temperature profiles, support fluid movement in stratigraphically defined conduits.

Seven major lithologic units are distinguished. Each of these units displays a general trend from bioturbated mudstones to wackestones at the bottom and an increase of packstones, grainstones, and floatstones toward the top. Within the units, subdivisions are defined based on the facies types and associations, texture, and the major components.

Unit I (0–162.1 mbsf) is of Holocene to latest Pliocene age. It consists of unlithified to partially lithified mudstones, wackestones, packstones, and floatstones. Its base is defined by the sudden appearance of peloids, which is a major component throughout Unit I. Two subunits are recognized. In Subunit IA (0–59.9 mbsf), two intervals of unlithified packstones to floatstones, containing *Halimeda* debris and lithoclasts, are intercalated in unlithified mudstones. In Subunit IB (59.9–162.1 mbsf), an upper aragonite-rich part with some laminated redeposited intervals overlies poorly stratified and bioturbated mudstone to wackestone.

Unit II (159.9–360.01 mbsf) is early Pliocene in age and consists of partially lithified, intensely bioturbated wackestones with some variations in bioturbation and skeletal fragments. The unit is slightly dolomitized (20%–25%) at the top, decreasing downhole to about 10%.

Unit III (368.2–492.7 mbsf, early Pliocene in age) has a characteristic succession of facies that is repeated in the underlying units. The top part of this and the following units is dominated by packstones to grainstones that often display sedimentary structures indicative of turbidites and other mass gravity flow deposits. The background sediments of these packstones and grainstones are bioturbated wackestones. The bottom part of the units are composed of packstone to wackestone alternations of light gray, lithified beds with an average thickness of 30 to 40 cm and darker, greenish to brownish gray, less lithified intervals of 15 to 25 cm thickness. The alternations are moderately to heavily bioturbated and contain planktonic and benthic foraminifers and other bioclasts.

The middle to late Miocene-aged Unit IV (492.7–643 mbsf) is divided into two subunits. Subunit IVA (492.7–591.2 mbsf) is dominated by packstones and grainstones and is characterized by interbedded light gray to grayish laminated, fining-upward beds and greenish to brownish gray, strongly bioturbated beds. Subunit IVB (597.9–643 mbsf) consists of moderately to heavily bioturbated light gray to dark gray, slightly dolomitized bioclastic packstones to grainstones. Components in the packstones and grainstones include planktonic and benthic foraminifers, bioclasts (including rare *Halimeda* debris), and lithoclasts. Subunit IVB is characterized by a cyclic alternation between well-lithified packstones with large well-developed burrows and finer-grained zones with flattened burrows.

Unit V (646–915.8 mbsf) is middle Miocene in age and can be separated into two subunits. Subunit VA (646–738.8 mbsf) consists of laminated, bioclastic packstone and grainstone beds with sharp or scoured bases. Dominant allochems include planktonic and benthic foraminifers. In Subunit VB (742–915.8 mbsf) wackestones and packstones grade downhole into mudstones and wackestones that show a distinct cyclicity of light gray, well-cemented, moderately bioturbated intervals, and strongly bioturbated, dark gray to green layers. Thickness of the cycles ranges from 50 to 200 cm. These darker intervals also contain a small amount of clay- and silt-sized quartz, plagioclase, and clay.

Unit VI (915.8–1151.63 mbsf; early Miocene to middle Miocene in age) is separated into two subunits. The top of Subunit VIA (915.8–973.38) is characterized by a well-defined, irregular surface (hardground). The subunit has intercalations of packstones and floatstones in a background sedimentation of bioturbated, greenish-grayish wackestones and packstones. The background deposits show the same type of cyclicity as Subunit VB. The underlying Subunit VIB (973.89–1151.38) is three times thicker and consists entirely of cyclic alternations of lighter and darker intervals as previously described.

In the lower Miocene Unit VII (1151.63–1296.41 mbsf), the packstone-dominated Subunit VIIA (1151.63–1194.77) is even thinner (43 m) and its packstones are thin-bedded (5–10 cm). In contrast, the underlying cyclic Subunit VIIB (1194.77–1296.41) is more than 100 m thick. In this subunit, the siliciclastic admixture is approximately 5%–7%. Units VII–IV, therefore, show an overall thickening- and coarsening-upward trend in their packstone-dominated subunits, indicating a pulsed, but progressive, progradation of the Great Bahama Bank throughout the Miocene.

Dating the Neogene sedimentary packages that were deposited in an upper bathyal environment on the slope of the western Great Bahama Bank was possible, despite problems of diagenesis and dilution. Most conventional Neogene nannofossil and planktonic foraminifer datum levels that are used in the deep-sea pelagic environment were also found here, and a fine nannofossil-planktonic foraminiferal stratigraphy was established. The sediments recovered at Site 1003 yielded a large number of biohorizons, both from calcareous nannofossils and planktonic foraminifers appearing in proper succession, which is remarkable given the nature of the sedimentary sequence close to the bank. The onset of the modern platform production is documented by a high sedimentation rate during the last 0.9 to 1.0 Ma (10 cm/k.y.) The lower Pleistocene to upper Pliocene interval shows a much slower sedimentation rate of about 2.5 cm/k.y., indicating a decreased input from the banktop. The lower Pliocene section (Units II and III) is highly expanded. During this period, the platform produced a lot of material that was shed onto the upper slope. In contrast, the early late Miocene was characterized by pelagic sedimentation rates of about 3 cm/k.y. This was a time of global cooling and falling sea level that ultimately caused an unconformity separating the lowermost upper Miocene from lower Pliocene. This unconformity coincides with the lithologic break between sedimentological Units III and IV. The Miocene unconformities punctuate periods of high sedimentation rates during which the input from the platform must have been high. For example, the middle Miocene shows a very high sedimentation rate of up to 15 cm/k.y. One unconformity was identified within this interval; planktonic foraminiferal Zones N9 and N10 are missing. The unconformity coincides with the hardground that marks the top of Unit VIA. The lowermost unconformity separating lithologic Unit VIIA from Unit VIIB occurs within nannofossil Zone NN2 and straddles the planktonic foraminiferal Zones N4 and N5.

Sedimentation rates from the lowermost Miocene to the Holocene seem to be controlled by changes in sea level. Thick and expanded intervals during the early and middle Miocene coincide with the generally high sea level of this time. The late Miocene, a time of global cooling and sea-level fall, is recorded in a reduced interval and a subsequent hiatus. The Pliocene sea-level rise resulted in renewed flooding of the Great Bahama

Bank and sedimentation on the slope. The sedimentary successions of more pelagic deposits alternating with more neritic sediments provide evidence of the numerous sea-level changes during the Pliocene and Pleistocene. These sea-level controlled sedimentologic variations are recorded on the seismic data. With one exception, all the sequence boundaries determined prior to drilling coincide either with unit or subunit boundaries. Two unit boundaries occur within seismic sequences, indicating a higher resolution within the sedimentary record. In addition, small-scale sedimentary cycles provide evidence for high-frequency sea-level changes.

The carbonate mineralogy is dominated by aragonite with lesser amounts of high-magnesium calcite (HMC) and dolomite throughout the upper 110 mbsf. Below this depth, corresponding approximately with the Pliocene/Pleistocene boundary, aragonite decreases markedly, HMC disappears, and dolomite becomes more important. Variable amounts of dolomite are present throughout the remainder of the core, commonly occurring below nondepositional surfaces. Small amounts of feldspar are also present in the lower portion of Hole 1003B. Diagenetic minerals such as celestite, native sulfur, and chert are found sporadically throughout, particularly in fractures. Carbonate contents are generally high throughout the samples measured and organic contents are generally low. In the Miocene section, however, carbonate content gradually decreases to 85% and drops to 50% or less in the intervals above sequence boundaries, providing further evidence of reduced carbonate input in these intervals. The packstones to wackestones between 700 and ~1000 mbsf in Hole 1003C possess a strong petroleum odor and have experienced some oil migration.

The pore-water chemistry shows unusual trends that are probably related to lateral movement along more permeable sedimentary units. Although there are gradual changes in most chemical constituents with increasing depth, these changes accelerate across major permeability barriers. The shallowest of these occurs at ~85 mbsf. Below this depth, the salinity starts to increase, reaching values as high as 62 ppt at 820 mbsf. Alkalinity and H_2S also increase across this barrier, while sulfate decreases. Calcium continues to increase throughout the hole while the relative concentration of Mg decreases. Nonsteady state profiles exist for all of the measured constituents (salinity, sulfate, calcium, strontium, ammonium, lithium, fluoride, alkalinity, and magnesium). The C_1/C_N was considered to be anomalous throughout the hole, indicating the presence of migrated hydrocarbons. Alkanes higher than C_2 first appeared below a major change in lithology and formation velocity at 738 mbsf, which in addition to being a seismic reflector, was also a seal. It is probable that the hydrocarbons and bitumen found in the core were generated deep in the section and migrated upward and laterally. As these compounds moved upward, they were oxidized by sulfate reducing bacteria to produce H_2S and consequently lower pH. Decreases in the pH promote the extensive carbonate alteration seen throughout the core.

The log data obtained from Hole 1003D correlate well with the sedimentary succession and can be used to fill in gaps in low recovery zones. With log-to-core correlation, the changes recorded in the logs can be traced to the Great Bahama Bank along the seismic sequence boundaries, providing a tie of the sedimentation patterns at Site 1003 to other drill sites across the platform margin and on the platform top. A general downhole trend of increasing density, resistivity, and sonic velocity, and of decreasing porosity probably results from sediment compaction. However, there is a pronounced change in this trend at 738 mbsf, where the downhole gradient in density, resistivity, and velocity, is offset toward lower values while the porosities increase. This anomalous pattern may be the result of changing sediment composition as well as a diagenetic overprint. Below 738 mbsf, this major lithologic change is apparent in the natural gamma-ray and geochemical (Ca, Al, and Si) logs. The increased frequency and magnitude of the uranium signal is particularly notable. The salinity indicator ratio in the geochemical logs shows a sharp increase below 738 mbsf, implying a more saline formation fluid that is consistent with the high chlorinity measured in pore waters from these depths. Also below 738 mbsf, a notable cyclicity in the gamma-ray and FMS logs correlates to the sedimentation patterns noted throughout much of the Miocene portion of the cores.

BACKGROUND AND OBJECTIVES

Site 1003 was the first of five sites drilled during Leg 166 along the Bahamas Transect. Site 1003 is on the middle slope approximately 4 km from the western platform edge of the Great Bahama Bank and 12.6 km from the borehole Clino drilled on the banktop from a self-propelled jack-up barge (Fig. 1). The angle of the seafloor at Site 1003 is approximately 1.5°. The target horizon was the base of the Neogene, which proved to be more than 1300 mbsf. The seismic data of this portion of the slope show packages of continuous seismic reflections that alternate with channelized and discontinuous reflections (Fig. 2). Channelized intervals were interpreted as packages containing redeposited carbonates, and the more continuous reflections as the distal portions of downlapping clinoforms. Erosional truncations and reflection onlap patterns that identify seismic sequence boundaries were seen farther westward on the seismic line and carried along the reflections to Site 1003. A major erosional truncation that marks the base of seismic sequence Boundary D is still recognized at Site 1003. The downcutting unconformity overlies a seismic transparent zone at 0.75 s (TWT).

The youngest eight seismic sequences, which range in age from the late Miocene to Holocene, were drilled in the shallow drill sites Unda and Clino (Eberli et al., this volume). The core borings from these shallow drill sites provide the sedimentary record of the proximal part of the carbonate sequences. Cores from Site 1003 were drilled to document the facies successions in more distal portions of the sequences. The record of changing sea level was expected to be seen as variable input of platform-derived sediment. Low input to the basinal area occurs generally when platforms backstep or are exposed (Kendall and Schlager, 1981; Handford and Loucks, 1993). The timing of the main redeposition phase in carbonates, however, is still controversial. Classical sequence stratigraphic models predict an increase of mass gravity flow deposits during relative sea-level falls (Sarg, 1988; Vail et al., 1991). In contrast, carbonate sedimentologists point out that offbank transport of sediment is highest during sea-level highstands when the platform is flooded (Mullins, 1983; Droxler and Schlager, 1985; Reymer et al., 1988; Haak and Schlager, 1989; Schlager, 1991). Site 1003 is positioned above thick lower slope sections and thus is the ideal place to evaluate timing and

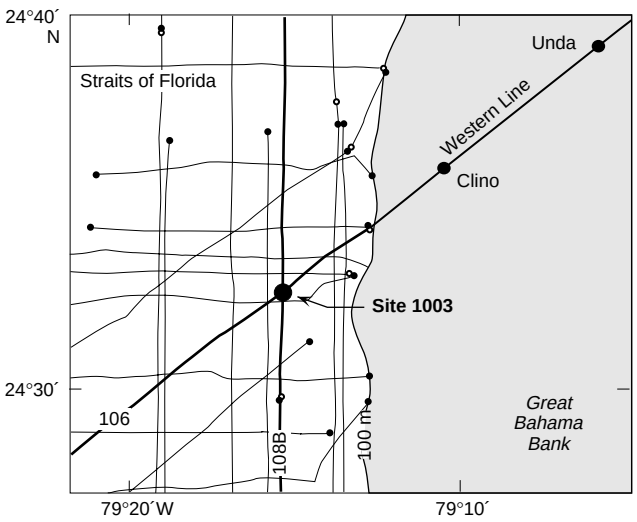

Figure 1. Location map of Site 1003. The site is located on the same seismic line as the two drill sites Unda and Clino that were drilled from a self-propelled jack-up barge on the shallow top of Great Bahama Bank in a water depth of 7 m.

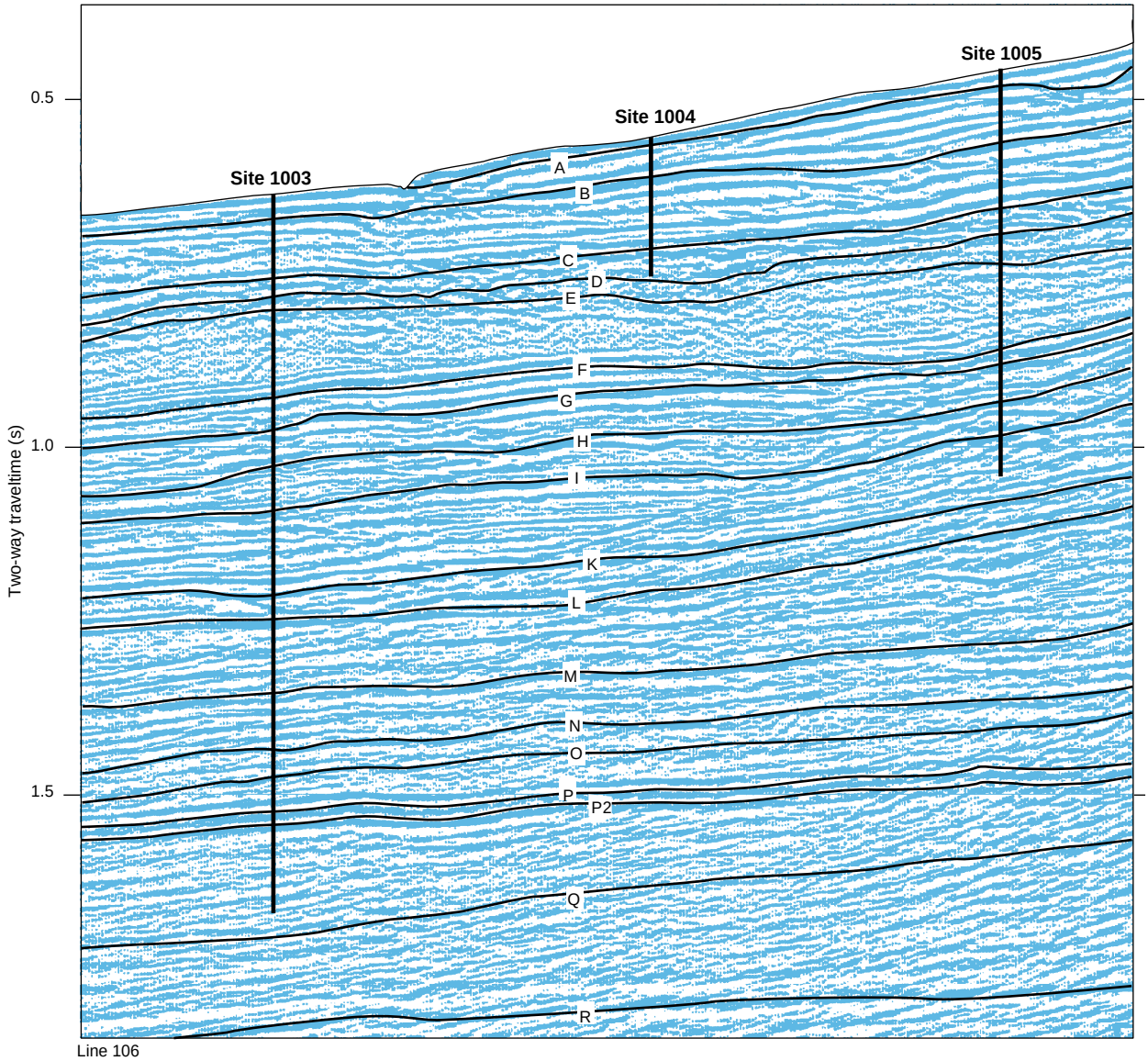

Figure 2. Portion of the high-resolution, multichannel seismic Line 106 that retraced the cross-bank Western Line with the positions of Sites 1003, 1004, and 1005. A downlapping prograding wedge (Sequences *d*–*a*) of latest Pliocene and Pleistocene age overlies an erosional truncation surface (0.75 s TWT at Site 1003) on top of a seismic transparent zone (Sequences *d* and *e*). An underlying thick section of slightly inclined reflections is of Miocene age. Total depth (TD) at Site 1003 was at 1300 mbsf in the lowest Miocene.

amount of mass gravity flow deposits and lowstand vs. highstand deposits.

Site 1003 also served as a distal site for one of two closely spaced transects for the fluid-flow objectives. Evidence for fluid flow was expected to be recorded in temperature and geochemical profiles. Temperature and geochemical measurements in the sediments were designed to detect nondiffusive geothermal gradients that would be indicative of water movement either into or out of the formation.

Summary of Objectives

In regard to sea level, the main objectives of this site were to:

1. Define the ages of the Neogene sequence boundaries;
2. Retrieve the sedimentary record of the middle to lower slope portions of the prograding carbonate sequences;
3. Produce a high-resolution isotope stratigraphy of the Neogene to Holocene;
4. Determine fluid flow using geochemical and geothermal gradients; and
5. Provide a calibration site in which an extended downhole logging program was to be undertaken to produce an optimal correlation between the cores and geophysical data, including a vertical seismic profile (VSP) experiment. The logging program was initially prevented by collapsing hole conditions. To achieve this goal a dedicated logging hole, Hole 1003C, was drilled to a depth of 1052 mbsf.

OPERATIONS

Transit, San Juan to Site 1003 (BT-2/F-2)

The ship departed San Juan at 1709 hr on 20 February 1996. Times reported in the "Operations" sections in this volume are in local time (U.S.A. Eastern Time Zone; UTC – 5 hr). The 857-nmi sea

voyage to the first waypoint of the seismic survey required approximately 68 hr at an average speed of 12.5 kt.

Seismic Survey

A 30-nmi seismic survey was conducted over Sites 1003, 1004, 1005, and 1007 (proposed sites BT-2/F-2, F-3, BT-1/F-1, and BT-3, respectively) in 4.7 hr at 6.3 kt. The ship returned to the GPS coordinates for Site 1003, and a Datasonics commandable retrievable beacon was dropped at 1812 hr on 23 February 1996. The height from sea level to the rig floor was 11.1 m for Hole 1003A, and 11.2 m for Holes 1003B, and 1003C.

Hole 1003A

An APC/XCB bottom-hole assembly (BHA) was attached to monel drill collars. Monel drill collars are intended to minimize remagnetization, allowing magnetic orientation of the APC cores. Hole 1003A was spudded at 2215 hr on 23 February. Core 166-1003A-1H was cut with the drill bit positioned at 490.0 mbrf (478.9 meters below sea level [mbsl]). Core 1H recovered 6.97 m; therefore, the seafloor was defined to be 481.4 mbsl.

Adara heat flow measurements were taken at Cores 3H through 9H. Core orientation using the Tensor tool was performed on Cores 4H through 9H. Using the APC, we cored 77.7 m recovering 69.85 m (89.9% recovery) (Table 1). Recovery was reduced by common hard carbonate layers/nodules and occasional sandy carbonate layers within soft carbonate ooze. Core 9H was a partial stroke with a split core liner and required 60,000 lb overpull to extract the core barrel from the formation. We then switched to the XCB coring method.

XCB cores were cut from Core 10X through 21X (77.7–188.1 mbsf). WSTP temperature measurements were performed after Cores 3X, 6X, 9X, and 22H (Core 22H was an attempt to switch back to APC coring method). Recovery ranged from 0% to 100% (mean = 44%). Cores 17X and 18X had carbonate nodules jammed in the shoe, and Cores 20X and 21X had no recovery in a very soft formation, resulting in heavy backflow.

APC Core 22H was taken from 188.1 to 197.6 mbsf with 103% recovery. The APC barrel stuck and could not be extracted from the formation with 60,000 lb overpull. The bit nozzles became plugged with cuttings that flowed back into the pipe, stalling the rotary. Overpull was gradually increased until circulation and rotation were restored. Although several nozzles remained plugged, XCB coring was resumed.

XCB Cores 23X through 27X were cut from 197.6 to 245.7 mbsf with 1.3% recovery. The bit nozzles remained plugged, and heavy backflow was observed. Consequently, the hole was terminated, and the bit cleared the rig floor at 2200 hr on 24 February.

Hole 1003B

The ship was moved 20 m to the northwest, and Hole 1003B was spudded at 0105 hr, 25 February. Core 1003B-1H was taken with the drill bit positioned at 488.0 mbrf (476.8 mbsl) and recovered 2.99 m; thus, the seafloor was defined to be 483.3 mbsl. APC cores were taken from Core 1H through 9H (0–79.0 mbsf) with 80.7% recovery. No oriented cores were taken. An Adara heat flow measurement was performed at Core 8H. APC coring was terminated at 79.0 mbsf with 60,000 lb overpull.

XCB cores were cut from Core 10X through 57X (79.0–541.6 mbsf) with recovery varying from 0 to 100% (mean = 27%). The WSTP was deployed after Core 11X. Recovery was reduced by moderately hard layers that jammed in the shoe. Recovery was low in formation sections with alternating lithified and unlithified sediments. The pump rate was reduced in soft carbonates to reduce washing and was increased to reduce jamming in harder carbonates. The formation sections became noticeably harder in Cores 34X (310.6 mbsf), 40X (368.2 mbsf), and 52X (483.9 mbsf), with increased drilling time and torque, and reduced recovery. Hole 1003B was terminated, and the bit cleared the rig floor at 1545 hr, 26 February.

Hole 1003C

The ship was moved 10 m northwest of Hole 1003B. Hole 1003C was spudded using the RCB system at 2020 hr on 26 February. The water depth was assumed to be 483.3 mbsl based on adjacent Hole 1003B. The hole was drilled from 0 to 406.0 mbsf. Cores 1003C-1R and 2R were cut from 406.0 to 425.3 mbsf. After retrieval of Cores 1R and 2R, the hole was drilled from 425.3 to 473.5 mbsf. RCB Cores 3R through 88R were then cut from 473.5 to 1300.0 mbsf. From the original approval depth of 1050 mbsf, Hole 1003C was deepened to 1300 mbsf to reach the base of the Neogene, after which coring was terminated. Recovery using the RCB system ranged from 4.1 to 103.0% (mean = 44.7%). At least 21 cores were jammed from fractured core sections wedging in the shoe and liner. A strong petroleum odor was noted in Cores 30R through 41R (732.4–842.0 mbsf), with increasing amounts of heavier hydrocarbons (C_2–C_6) observed in headspace analyses. C_1/C_2 ratios decreased from 23 to 8. However, coring continued because the concentration of gas was very low, and there were no rapid changes in gas concentration or C_1/C_N ratios (C_1/C_2 ratios being already anomalously low from the top of the hole).

During the process of cleaning the hole in preparation for logging, the drill pipe became stuck. We unsuccessfully attempted to free the pipe for 5 hr using up to the maximum overpull allowed for shallow-water drilling (200,000 lb). The pipe was severed at 1008.5 mbsf with an explosive charge. The severed pipe was pulled to 96 mbsf and we dropped a free-fall funnel (FFF). The vibration-isolation tool was deployed with a television camera and sonar to verify positioning of the FFF, and the drill string was pulled out of the hole. An RCB BHA was deployed, and the hole was re-entered for logging. However, the drill pipe became stuck again while attempting to condition the hole, and we were not able to penetrate deeper than 465 mbsf. We encountered similar conditions while pulling up the drill string, which suggested that the upper part of the hole was collapsing. Therefore, we judged it imprudent to make any further attempts to log the hole. Hole 1003C was terminated, and the bit cleared the rig floor at 1457 hr, 6 March.

Hole 1003D

After evaluating hole stability and logging potential at several sites, we decided to return to Site 1003 to drill a dedicated logging hole. The 14.0-nmi transit from Site 1006 to Site 1003 required 4.25 hr. After the ship was positioned on the GPS coordinates (24°32.763′N, 79°15.650′W), a beacon was dropped at 0530 hr, 20 March. A drilling BHA was assembled and run to the seafloor (482.9 mbsl). The hole was drilled to 677.0 mbsf and then conditioned with a short trip from 677.0 to 536.0 mbsf with no overpull or drag. Drilling was resumed from 677.0 to 1052.7 mbsf. A standard wiper trip was performed to 100 mbsf, encountering 2.5 m of soft fill, and the bit was released with a mechanical bit release (MBR). After circulating a sweep of sepiolite mud, the pipe was pulled to 106 mbsf for logging. DIT/sonic, FMS, IPLT, GLT, and WST logs were run to 1052.7 mbsf. After plugging the hole with cement and gel mud, the pipe was pulled and secured for transit at 0723 hr on 24 March. Although the beacon indicated release, it did not surface and could not be retrieved.

LITHOSTRATIGRAPHY

Lithologic Units

Deposits at Site 1003 consist of periplatform oozes, turbidites, and mass-flow deposits. These sediments are interbedded with pelagic intervals composed of oozes and chalks. Deposits generally contain between 92 and 97 wt% carbonate. Carbonate mineralogy was

Table 1. Site 1003 coring summary.

Core	Date (1996)	Time (UTC)	Depth (mbsf)	Length cored (m)	Length recovered (m)	Recovery (%)
166-1003A-						
1H	24 Feb	0320	0.0–7.0	7.0	6.97	99.6
2H	24 Feb	0355	7.0–16.5	9.5	8.72	91.8
3H	24 Feb	0420	16.5–26.0	9.5	9.68	101.0
4H	24 Feb	0505	26.0–35.5	9.5	3.19	33.6
5H	24 Feb	0620	35.5–45.0	9.5	10.08	106.1
6H	24 Feb	0700	45.0–54.5	9.5	9.52	100.0
7H	24 Feb	0735	54.5–64.0	9.5	8.74	92.0
8H	24 Feb	0830	64.0–73.5	9.5	8.71	91.7
9H	24 Feb	0945	73.5–77.7	4.2	4.23	101.0
10X	24 Feb	1055	77.7–84.8	7.1	0.31	4.4
11X	24 Feb	1125	84.8–91.9	7.1	4.06	57.2
12X	24 Feb	1200	91.9–101.6	9.7	3.99	41.1
13X	24 Feb	1315	101.6–111.1	9.5	7.55	79.5
14X	24 Feb	1340	111.1–120.7	9.6	9.57	99.7
15X	24 Feb	1400	120.7–130.3	9.6	6.1	63.5
16X	24 Feb	1525	130.3–139.9	9.6	0.85	8.9
17X	24 Feb	1555	139.9–149.6	9.7	7.59	78.2
18X	24 Feb	1630	149.6–159.2	9.6	5.46	56.9
19X	24 Feb	1745	159.2–168.9	9.7	2.91	30.0
20X	24 Feb	1805	168.9–178.5	9.6	0	0.0
21X	24 Feb	1825	178.5–188.1	9.6	0	0.0
22H	24 Feb	2035	188.1–197.6	9.5	9.76	103.0
23X	24 Feb	2210	197.6–207.2	9.6	0.49	5.1
24X	24 Feb	2235	207.2–216.8	9.6	0.11	1.1
25X	24 Feb	2310	216.8–226.4	9.6	0	0.0
26X	24 Feb	2335	226.4–236.1	9.7	0.16	1.7
27X	24 Feb	2355	236.1–245.7	9.6	0.37	3.9
Coring totals				245.7	129.12	52.6
166-1003B-						
1H	25 Feb	0610	0.0–3.0	3.0	2.99	99.6
2H	25 Feb	0640	3.0–12.5	9.5	8.9	93.7
3H	25 Feb	0700	12.5–22.0	9.5	0.1	1.1
4H	25 Feb	0725	22.0–31.5	9.5	4.03	42.4
5H	25 Feb	0815	31.5–41.0	9.5	8.79	92.5
6H	25 Feb	0845	41.0–50.5	9.5	9.73	102.0
7H	25 Feb	0910	50.5–60.0	9.5	9.88	104.0
8H	25 Feb	0955	60.0–69.5	9.5	9.53	100.0
9H	25 Feb	1025	69.5–79.0	9.5	9.79	103.0
10X	25 Feb	1120	79.0–88.5	9.5	5.09	53.6
11X	25 Feb	1235	88.5–98.1	9.6	9.63	100.0
12X	25 Feb	1310	98.1–107.7	9.6	2.73	28.4
13X	25 Feb	1335	107.7–117.4	9.7	9.57	98.6
14X	25 Feb	1355	117.4–127.1	9.7	1.21	12.5
15X	25 Feb	1415	127.1–136.8	9.7	7.14	73.6
16X	25 Feb	1435	136.8–146.5	9.7	2.02	20.8
17X	25 Feb	1455	146.5–156.2	9.7	0.49	5.1
18X	25 Feb	1515	156.2–165.9	9.7	0.35	3.6
19X	25 Feb	1535	165.9–175.6	9.7	5.6	57.7
20X	25 Feb	1605	175.6–185.3	9.7	8.04	82.9
21X	25 Feb	1625	185.3–195.0	9.7	9.62	99.2
22X	25 Feb	1650	195.0–204.7	9.7	5.97	61.5
23X	25 Feb	1710	204.7–214.3	9.6	5.93	61.8
24X	25 Feb	1735	214.3–224.0	9.7	5.7	58.7
25X	25 Feb	1755	224.0–233.7	9.7	0.23	2.4
26X	25 Feb	1815	233.7–243.3	9.6	0.93	9.7
27X	25 Feb	1845	243.3–252.9	9.6	0.59	6.1
28X	25 Feb	1905	252.9–262.5	9.6	1.79	18.6
29X	25 Feb	1930	262.5–272.2	9.7	1.35	13.9
30X	25 Feb	1950	272.2–281.8	9.6	0	0.0
31X	25 Feb	2010	281.8–291.4	9.6	3.01	31.3
32X	25 Feb	2100	291.4–301.0	9.6	3.27	34.0
33X	25 Feb	2125	301.0–310.6	9.6	0.28	2.9
34X	25 Feb	2150	310.6–320.2	9.6	1.43	14.9
35X	25 Feb	2220	320.2–329.9	9.7	2.95	30.4
36X	25 Feb	2305	329.9–339.4	9.5	4.22	44.4
37X	25 Feb	2335	339.4–349.0	9.6	0.37	3.9
38X	25 Feb	2355	349.0–358.6	9.6	3.23	33.6
39X	26 Feb	0025	358.6–368.2	9.6	1.48	15.4
40X	26 Feb	0100	368.2–377.9	9.7	0.82	8.5
41X	26 Feb	0135	377.9–387.5	9.6	0.5	5.2
42X	26 Feb	0225	387.5–397.1	9.6	0.97	10.1
43X	26 Feb	0300	397.1–406.8	9.7	0.35	3.6
44X	26 Feb	0335	406.8–416.4	9.6	0.6	6.3
45X	26 Feb	0420	416.4–426.1	9.7	0.58	6.0
46X	26 Feb	0515	426.1–435.7	9.6	0.5	5.2
47X	26 Feb	0605	435.7–445.3	9.6	0.47	4.9
48X	26 Feb	0700	445.3–454.9	9.6	1.46	15.2
49X	26 Feb	0750	454.9–464.6	9.7	1.29	13.3
50X	26 Feb	0845	464.6–474.2	9.6	2.16	22.5
51X	26 Feb	0940	474.2–483.9	9.7	0.52	5.4
52X	26 Feb	1045	483.9–493.5	9.6	0.55	5.7
53X	26 Feb	1225	493.5–503.1	9.6	0.33	3.4
54X	26 Feb	1320	503.1–512.7	9.6	2.58	26.9
55X	26 Feb	1430	512.7–522.4	9.7	0.8	8.3
56X	26 Feb	1600	522.4–532.0	9.6	3.08	32.1
57X	26 Feb	1705	532.0–541.6	9.6	1.92	20.0
Coring totals				541.6	187.44	34.6
166-1003C-						
1R	27 Feb	1320	406.0–415.6	9.6	3.88	40.4
2R	27 Feb	1400	415.6–425.3	9.7	1.32	13.6
3R	27 Feb	1750	473.5–483.1	9.6	1.8	18.7
4R	27 Feb	1855	483.1–492.7	9.6	4.25	44.3
5R	27 Feb	1955	492.7–502.3	9.6	1.88	19.6
6R	27 Feb	2050	502.3–511.9	9.6	4.08	42.5
7R	27 Feb	2140	511.9–521.5	9.6	1.43	14.9
8R	27 Feb	2325	521.5–530.5	9.0	2.86	31.8
9R	28 Feb	0030	530.5–540.1	9.6	3.71	38.6
10R	28 Feb	0115	540.1–549.7	9.6	1.5	15.6
11R	28 Feb	0155	549.7–559.3	9.6	1.03	10.7
12R	28 Feb	0300	559.3–568.9	9.6	1.5	15.6
13R	28 Feb	0355	568.9–578.6	9.7	1.66	17.1
14R	28 Feb	0510	578.6–588.3	9.7	3.72	38.3
15R	28 Feb	0615	588.3–597.9	9.6	2.56	26.6
16R	28 Feb	0725	597.9–607.5	9.6	2.72	28.3
17R	28 Feb	0835	607.5–617.1	9.6	3.72	38.7
18R	28 Feb	0950	617.1–626.7	9.6	4.31	44.9
19R	28 Feb	1105	626.7–636.3	9.6	2.07	21.5
20R	28 Feb	1235	636.3–646.0	9.7	6.09	62.8
21R	28 Feb	1505	646.0–655.7	9.7	5.11	52.7
22R	28 Feb	1615	655.7–665.3	9.6	3.71	38.6
23R	28 Feb	1810	665.3–674.9	9.6	1.27	13.2
24R	28 Feb	1935	674.9–684.5	9.6	3.96	41.2
25R	28 Feb	2150	684.5–694.1	9.6	4.03	42.0
26R	28 Feb	2345	694.1–703.6	9.5	5.31	55.9
27R	29 Feb	0240	703.6–713.2	9.6	3.16	32.9
28R	29 Feb	0505	713.2–722.8	9.6	0.67	7.0
29R	29 Feb	0745	722.8–732.4	9.6	4.24	44.1
30R	29 Feb	0945	732.4–742.0	9.6	5.22	54.4
31R	29 Feb	1100	742.0–751.6	9.6	2.34	24.4
32R	29 Feb	1215	751.6–761.2	9.6	8.52	88.7
33R	29 Feb	1325	761.2–770.8	9.6	3.62	37.7
34R	29 Feb	1455	770.8–780.4	9.6	3.86	40.2
35R	29 Feb	1615	780.4–790.1	9.7	8.15	84.0
36R	29 Feb	1725	790.1–799.8	9.7	8.45	87.1
37R	29 Feb	1845	799.8–809.4	9.6	6.74	70.2
38R	29 Feb	2000	809.4–819.0	9.6	7.62	79.4
39R	29 Feb	2125	819.0–828.6	9.6	2.29	23.8
40R	29 Feb	2250	828.6–838.2	9.6	7.01	73.0
41R	01 Mar	0025	838.2–847.9	9.7	4.23	43.6
42R	01 Mar	0140	847.9–857.5	9.6	5.75	59.9
43R	01 Mar	0320	857.5–867.1	9.6	2.56	26.6
44R	01 Mar	0445	867.1–876.7	9.6	5.75	59.9
45R	01 Mar	0615	876.7–886.3	9.6	4.56	47.5
46R	01 Mar	0820	886.3–896.0	9.7	6.27	64.6
47R	01 Mar	0945	896.0–905.6	9.6	0.58	6.0
48R	01 Mar	1115	905.6–915.2	9.6	6.04	62.9
49R	01 Mar	1240	915.2–924.8	9.6	0.59	6.1
50R	01 Mar	1450	924.8–934.5	9.7	2.45	25.2
51R	01 Mar	1710	934.5–944.1	9.6	0.39	4.1
52R	01 Mar	1920	944.1–953.7	9.6	2.69	28.0
53R	01 Mar	2115	953.7–963.4	9.7	1.11	11.4
54R	01 Mar	2255	963.4–973.0	9.6	3.48	36.2
55R	02 Mar	0125	973.0–982.6	9.6	2.88	30.0
56R	02 Mar	0345	982.6–992.2	9.6	2.23	23.2
57R	02 Mar	0540	992.2–1001.8	9.6	2.94	30.6
58R	02 Mar	0810	1001.8–1011.4	9.6	2.91	30.3
59R	02 Mar	1025	1011.4–1021.1	9.7	3.76	38.7
60R	02 Mar	1205	1021.1–1030.7	9.6	4.44	46.2
61R	02 Mar	1345	1030.7–1040.3	9.6	2.38	24.8
62R	02 Mar	1510	1040.3–1050.0	9.7	4.14	42.7
63R	02 Mar	1650	1050.0–1059.6	9.6	2.19	22.8
64R	02 Mar	1820	1059.6–1069.2	9.6	4.37	45.5
65R	02 Mar	2005	1069.2–1078.9	9.7	2.86	29.5
66R	02 Mar	2140	1078.9–1088.5	9.6	7.89	82.2
67R	02 Mar	2325	1088.5–1098.1	9.6	9.3	96.9
68R	03 Mar	0100	1098.1–1107.8	9.7	8.49	87.5
69R	03 Mar	0235	1107.8–1117.4	9.6	1.81	18.8
70R	03 Mar	0410	1117.4–1127.1	9.7	5.66	58.3
71R	03 Mar	0625	1127.1–1136.7	9.6	3.29	34.3
72R	03 Mar	0900	1136.7–1146.3	9.6	9.28	96.6
73R	03 Mar	1050	1146.3–1156.0	9.7	5.11	52.7
74R	03 Mar	1335	1156.0–1165.6	9.6	1.97	20.5
75R	03 Mar	1655	1165.6–1175.2	9.6	0.93	9.7
76R	03 Mar	1940	1175.2–1184.9	9.7	9.45	97.4
77R	03 Mar	2120	1184.9–1194.5	9.6	3.94	41.0
78R	03 Mar	2355	1194.5–1204.1	9.6	4.1	42.7
79R	04 Mar	0225	1204.1–1213.7	9.6	9.22	96.0
80R	04 Mar	0415	1213.7–1223.3	9.6	4.28	44.6
81R	04 Mar	0635	1223.3–1233.0	9.7	5.87	60.5

Table 1 (continued).

Core	Date (1996)	Time (UTC)	Depth (mbsf)	Length cored (m)	Length recovered (m)	Recovery (%)
82R	04 Mar	0925	1233.0−1242.6	9.6	8.91	92.8
83R	04 Mar	1205	1242.6–1252.3	9.7	5.76	59.4
84R	04 Mar	1445	1252.3–1261.9	9.6	6.14	63.9
85R	04 Mar	1815	1261.9−1271.5	9.6	9.41	98.0
86R	04 Mar	2045	1271.5–1281.0	9.5	9.79	103.0
87R	05 Mar	0010	1281.0–1290.7	9.7	8.78	90.5
88R	05 Mar	0300	1290.7−1300.0	9.3	5.76	61.9
Coring totals				845.8	378.06	44.7

166-1003D-
*****Drilled from 0 to 1052.7 mbsf*****

Note: An expanded version of this coring summary table that includes lengths and depths of sections, location of whole-round samples, and comments on sampling disturbance is included on CD-ROM in the back pocket of this volume.

verified using XRD (see "Inorganic Geochemistry" section, this chapter). In the lower part of the sedimentary succession, below 1151 mbsf, a variable but small amount of fine-grained siliciclastics are admixed in thin, silty layers.

Based on trends in textural changes of the deposits, on the major modifier (see "Explanatory Notes" chapter, this volume) and on the occurrence of coarser grained beds, which are interpreted to reflect redeposition by turbidity currents and other mass-flow processes, seven large-scale successions can be distinguished that correspond to sedimentary Units I–VII (Fig. 3). Each of these units shows an upward change from mud-supported to grain-supported textures.

The degree of lithification of the deposits changes downhole (Fig. 3). Unit I consists of an alternation of unlithified and partially lithified deposits, and Unit II of partially lithified to lithified sediments. Except for an interval in Core 166-1003B-49X, with partially lithified wackestones (Unit III), the remainder of the sedimentary succession (Units IV–VII) is lithified.

Lithologic Unit I

Intervals: 166-1003A-1H through 19X-CC, 10 cm; 166-1003B-1H through 18X-CC, 34 cm
Age: Pleistocene to late Pliocene
Depth: 0–162.1 mbsf

Unit I primarily consists of unlithified to partially lithified mudstones, wackestones, packstones, floatstones, and minor nannofossil oozes (Fig. 3). These sediments contain approximately equal amounts of platform-derived mud and calcareous sand mixed with pelagic carbonate components (i.e., periplatform ooze sensu Schlager and James [1978]).

Smear-slide analyses (see Section 4, this volume) show that aragonite needles (5–10 µm) are an important but variable component in the silt-sized fraction of Unit I. The X-ray data are compatible with the smear-slide data and indicate that in the interval from 90 to 140 mbsf the aragonite content of the sediments decreases markedly from as much as 50 to 0 wt% (Cores 166-1003A-12X to 16X; Cores 166-1003B-11X to 16X).

The high amount of peloids (20%–78% of the components) allows Unit I to be separated from the underlying deposits of Unit II, which show a maximum of 5% of this component (Fig. 4). Based on the occurrence of a 9.5-m-thick nannofossil ooze interval in Core 166-1003B-6H, we can divide Unit I into an upper Subunit IA and a lower Subunit IB. Sediments in Subunit IA show a change from pelagic conditions within the lowermost part of the unit to deposits with a strong input of coarse particles in the middle and upper part of the subunit, which are derived from the shallow-water carbonate production area.

Subunit IB consists of an alternation of coarser and finer grained intervals that are rich in platform-derived components. In addition to the downhole disappearance of peloids, the boundary between Subunit IB and Unit II is defined by a downhole textural change from unlithified packstones to wackestones (Fig. 3).

Lithologic Subunit IA

Intervals: 166-1003A-1H through 7H-5, 135 cm; 166-1003B-1H through 7H-CC, 14 cm
Age: Pleistocene
Depth: 0–59.9 mbsf

The upper part of Subunit IA is dominated by unlithified mudstones to unlithified wackestones, with silt- to sand-sized particles (silt- to sand-sized planktonic and benthic foraminifers, peloids, bioclasts, and lithoclasts) in a matrix with aragonite needles, nannofossils, and micrite. These sediments appear mottled as a result of pervasive minor to moderate bioturbation. Intercalated in these deposits are several unlithified packstone to floatstone layers.

The uppermost of these layers is 241 cm thick (Core 166-1003A-2H), and contains abundant *Halimeda* debris, bivalves, gastropods, echinoderms, encrusting red algae, foraminifers, and pteropods. The unlithified floatstone occurs 80 cm above the lower boundary of this interval, most likely the Pleistocene/Holocene boundary (see "Biostratigraphy" section, this chapter), in which interval 166-1003A-2H-6, 75–95 cm is characterized by an inclined contact separating light gray unlithified mudstones above from underlying gray unlithified mudstones below. The other layers (intervals 166-1003A-6H-2, 86–96 cm; 6H-3, 70–72 cm; and 5H-5, 94–102 cm) with coarse-grained debris are thinner (8 to 10 cm) and contain *Halimeda* plates, lithoclasts, and benthic foraminifers. In addition to these well-defined coarser grained layers, cobble-sized components, such as a lithoclast with *Lithophaga* borings, appear floating in the unlithified mudstones (e.g., interval 166-1003A-3H-3, 50–51 cm).

The lower part of Subunit IA is composed of light gray to gray nannofossil ooze. Sand-sized components are minor but include foraminifers, peloids, and shell fragments. The base of the nannofossil ooze defines the contact between Subunits IA and IB.

Lithologic Subunit IB

Intervals: 166-1003A-7H-5, 136 cm, through 19X-CC, 10 cm; 166-1003B-8H-1 through 18X-CC, 34 cm
Age: late Pliocene to Pleistocene
Depth: 59.9–162.1 mbsf

Subunit IB consists of unlithified to (lithified) peloidal mudstones, wackestones, packstones, and floatstones.

The dominant lithologies are wackestones to fine-grained packstones. In addition to peloids, other important components of these deposits include bivalve shell fragments, planktonic foraminifers, pteropods, and echinoderm debris. Minor components include benthic foraminifers and coral fragments. Smear-slide analysis shows that the matrix consists of aragonite needles, micrite, and nannofossils. These sediments are generally poorly stratified and show only a faint color mottling as a result of bioturbation. A thin section of the middle part of Subunit IB (interval 166-1003B-13X-6, 20–22 cm; see Section 5, this volume) consists of packstone to wackestone with a microsparitic to micritic matrix. Allochems are miliolids, planktonic foraminifers, hyaline benthic foraminifers (rare), brown skeletal grains, and other unidentifiable bioclasts.

This type of "background sedimentation" is interrupted by several packstone to floatstone layers indicating redeposition: in interval 166-1003A-11X-2, 95 cm, through 11X-CC, a layer of unlithified floatstone to packstone with *Halimeda* debris floating in a matrix of aragonite needles is present. Sedimentary structures in the layer are characterized by contorted laminae, indicating a slump deposit. This slumped interval is overlain by planar to slightly wavy (low-angle),

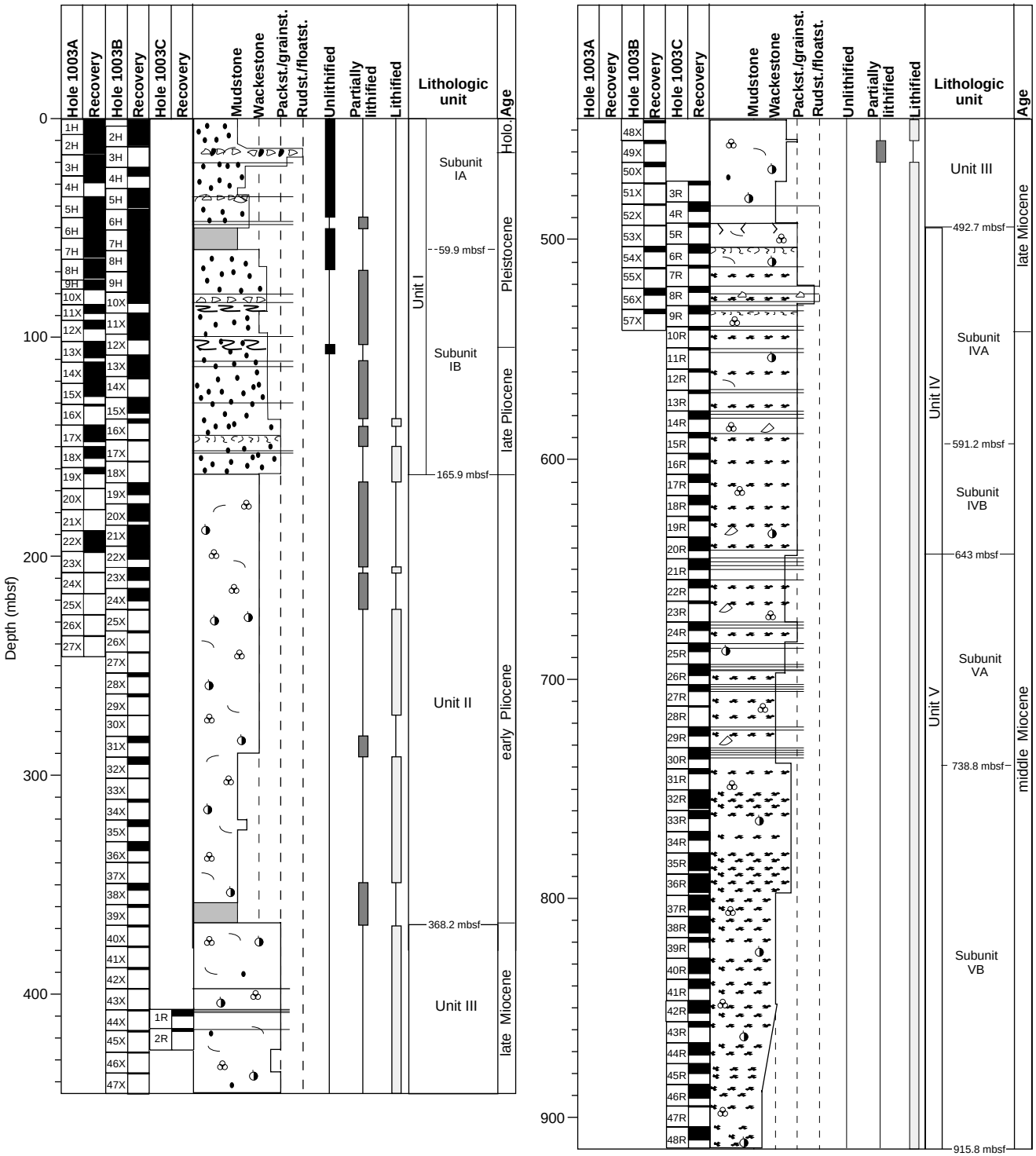

Figure 3. Synthesis of dominant textures and components of the sedimentary succession at Site 1003.

laminated, partially lithified packstones to grainstones with sand- to silt-sized components (bivalve debris, peloids, foraminifers).

Another major packstone layer occurs in interval 166-1003B-12X-2, 56–80 cm, above the Pliocene/Pleistocene boundary (see "Biostratigraphy" section, this chapter). The layer has a lower part with convolute bedding and an upper part with a faint planar lamination. Major components are black lithoclasts, foraminifers, bioclasts, and white mud pebbles.

The remainder of the packstone layers are thin bedded (up to 10 cm thick) and are characterized by normal grading, faint planar lamination, or ripple cross lamination. Components found in these intervals are planktonic and benthic foraminifers, lithoclasts, and bioclasts. A firmground was only observed in one core in Section 166-1003A-17X-5, 5 cm; this firmground shows a sharp, burrowed contact.

Lithologic Unit II

Intervals: 166-1003A-19X-CC, 10 cm, through bottom of Hole 1003A; 166-1003B-19X through 39X

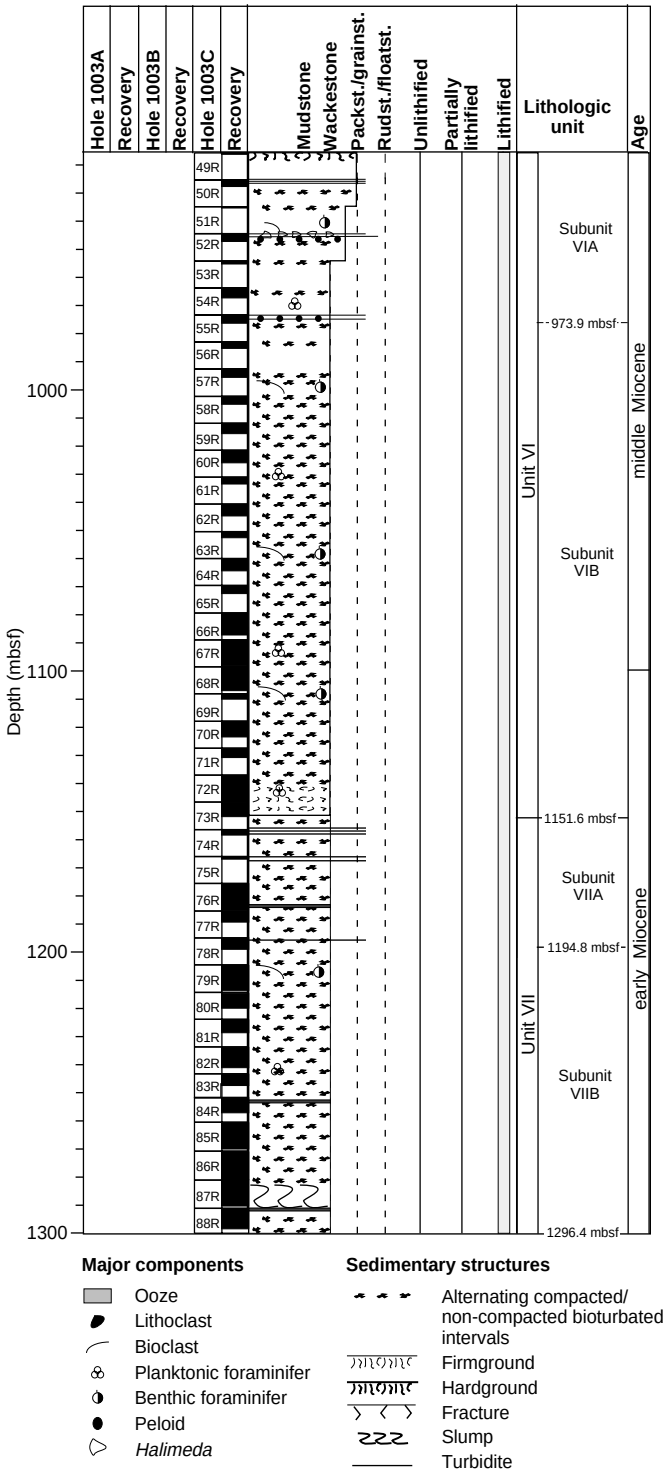

Figure 3 (continued).

Age: early Pliocene to late Miocene
Depth: 162.1–368.2 mbsf

The upper limit of Unit II is defined by the sudden disappearance of peloids in unlithified packstones at the base of Unit I. Unit II consists predominately of light gray, partially lithified wackestones in the upper part and light brownish gray wackestones and mudstones in the lower part. Major components, as determined in thin section (Sample 166-1003B-23X-1, 50–53 cm), include planktonic foraminifers, benthic foraminifers (rotaliids, miliolids), echinoderm-debris, and pteropods. Minor components include sand-sized bioclasts, sand- to silt-sized intraclasts (some have a black color), ostracodes, and tunicate spicules. The deposits of this unit are generally uniform and show a poorly defined color mottling (grayish to dark grayish) as a result of bioturbation. In general, heavily bioturbated intervals are darker in color than weakly bioturbated zones.

Smear-slide data show that dolomite rhombs make up to 25% of the silt- to clay-sized fraction in partially lithified wackestones. The X-ray data are consistent with smear-slide analyses and indicate that dolomite contents in partially lithified wackestones range from 20% to 25%. Below 224 mbsf and at the same level where wackestones in Unit II become lithified, dolomite content drops sharply to 10–15 wt%. The lower limit of Unit II lies at the base of an interval of gray to dark gray nannofossil chalk in Core 166-1003B-39X, which is characterized by discontinuous planar to wavy lamination.

Lithologic Unit III

Interval: 166-1003B-40X through 52X and through 166-1003C-4R-3, 74 cm
Age: late Miocene
Depth: 368.2–492.7 mbsf

Unit III is composed of an upper interval of gray to light gray wackestones, packstones, and grainstones. Packstones and grainstones occur in planar laminated, fining-upward beds, which are up to 30 cm thick. Components in these beds are coarser grained and consist of benthic foraminifers, bivalve fragments, blackened lithoclasts, and *Halimeda* debris. Bivalve fragments are often dissolved and preserved as molds.

Downhole, deposits consist of wackestones to mudstones with benthic and planktonic foraminifers, and bioclasts. The wackestones display a cyclic alternation of lighter (gray), more lithified beds (average thickness, 30–40 cm), and darker (greenish to brownish gray), less lithified intervals (average thickness, 15–25 cm). The less lithified parts of these cycles show an intense bioturbation, whereas the better lithified parts are only moderately bioturbated. In general, deposits of Unit III are slightly dolomitized.

Lithologic Unit IV

Interval: 166-1003C-5R through 20R
Age: late Miocene to middle Miocene
Depth: 492.7–643 mbsf

The upper limit of Unit IV is placed above an interval with celestite-filled, subvertical fractures (interval 166-1003C-5R-1, 103–125 cm). Fracture tops are crosscut by overlying sediments (Fig. 5).

Two subunits are differentiated in Unit IV. The upper part of Unit IV, Subunit IVA, is characterized by the occurrence of laminated, normally graded packstone to grainstone beds. Subunit IVB, which forms the lower part of Unit IV, consists of bioturbated and structureless packstones. In some cores (e.g., 166-1003C-18R) fractures are filled with native sulfur.

Lithologic Subunit IVA

Interval: 166-1003C-5R through 15R
Age: late Miocene to middle Miocene
Depth: 492.7–591.2 mbsf

The uppermost part of this subunit consists of packstones and grainstones. This interval is characterized by an interbedding of up to 34-cm-thick, light grayish to grayish, laminated, fining-upward beds (Fig. 6), and greenish to brownish gray, strongly bioturbated intervals.

The lower part of the light grayish to grayish beds is composed of packstones to grainstones that grade upward into fine-grained packstones and wackestones. Components in the graded beds are plank-

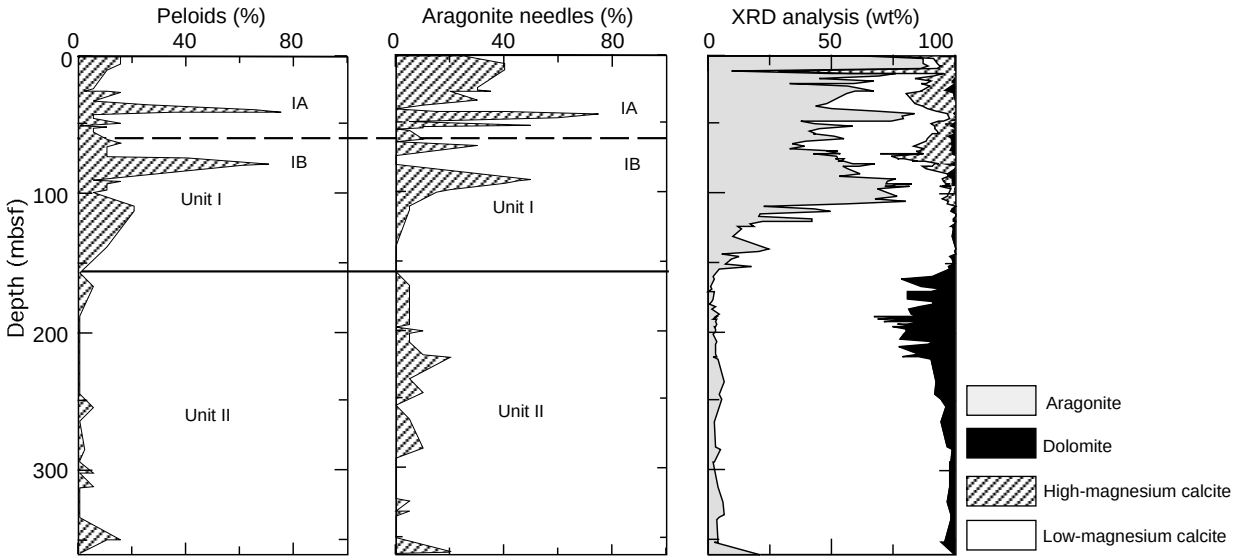

Figure 4. Percent abundance of peloids and aragonite needles in sediments of Hole 1003B (visual estimation in smear slides). Plot on the right-hand side of the figure shows carbonate mineralogies as determined by XRD (see "Inorganic Geochemistry" section, this chapter).

tonic and benthic foraminifers, lithoclasts, and rare *Halimeda* debris. Molds indicate that other bioclasts (e.g., bivalves) were also part of the original component assemblage. The strongly bioturbated, darker intervals (Fig. 7) consist of fine-grained packstones that contain planktonic and benthic foraminifers, rare pteropods, and bioclasts, some of them preserved as moldic porosity. Foraminifer tests in the packstone-to-grainstone intervals are cemented, whereas intraparticle porosity has been preserved in foraminifers. Foraminifer inner-chamber walls show only very thin rims of blocky to bladed cement. Firmgrounds characterized by sharp, burrowed contacts occur within the upper part of Subunit IVA: in Sections 166-1003B-54X-2, 10 cm, and 166-1003C-9R-3, 33 cm.

Lithologic Subunit IVB

Interval: 166-1003C-16R through 20R
Age: middle Miocene
Depth: 597.9–643 mbsf

Subunit IVB consists of moderately to heavily bioturbated light gray to dark olive gray, slightly dolomitized bioclastic packstones to grainstones. Components consist of planktonic and benthic foraminifers and bioclasts. Molds indicate that other bioclasts (e.g., bivalves) were also part of the original component assemblage.

The depositional pattern of Subunit IVB is characterized by a cyclicity that consists of an alternation of two lithologic members. First, gray, well-lithified packstone beds with large, well-defined burrows, and second, darker (greenish), and finer grained intervals with flattened burrows. The thickness of an individual cycle varies between 100 and 150 cm.

Lithologic Unit V

Interval: 166-1003C-21R through 30R
Age: middle Miocene
Depth: 646.0–915.8 mbsf

Unit V consists of grayish to greenish gray mudstones to packstones. The occurrence of laminated and normally graded packstone to grainstone beds in the upper part of the unit allows differentiation of this part of the sedimentary succession (Subunit VA) into a lower part (Subunit VB) that consists of bioturbated mudstones to packstones. In some intervals of the unit, darker, chertified horizons occur (e.g., in intervals 166-1003C-24R-2, 40–45 cm, and 25R-3, 32–37 cm). In general, the deposits of Unit V are slightly dolomitized. The upper limit of the zone, which contains high concentrations of high molecular hydrocarbons (735 mbsf; see "Organic Geochemistry" section, this chapter), coincides with the boundary between Subunits VA and VB.

Lithologic Subunit VA

Interval: 166-1003C-21R through 30R
Age: middle Miocene
Depth: 646.0–738.8 mbsf

Subunit VA is characterized by the occurrence of laminated (planar, wavy, and ripple lamination) bioclastic packstone and grainstone beds with sharp or scoured bases. Dominant allochems are planktonic and benthic foraminifers. Molds indicate that other bioclasts (e.g., bivalves) were also part of the original component assemblage. Within individual beds, a lower laminated part grades upward into an increasingly burrowed upper part. These beds are interbedded with bioclastic wackestones to fine-grained bioclastic packstones that are moderately to heavily bioturbated. Some of these zones (e.g., in Core 166-1003C-22R) are rich in blackened planktonic foraminifers, benthic foraminifers, and echinoid spines.

Lithologic Subunit VB

Interval: 166-1003C-31R through 49R-1, 60 cm
Age: middle Miocene
Depth: 742.0–915.8 mbsf

This subunit consists of wackestones to packstones grading downhole into mudstones to wackestones. The deposits show a distinct cyclicity between light gray, well-cemented, moderately bioturbated intervals, and dark gray to green layers that are strongly bioturbated. The light intervals consist of slightly dolomitized wackestones with planktonic and benthic foraminifers. The darker zones consist of less lithified wackestones with abundant planktonic foraminifers, fine-grained bioclasts, and disseminated organic matter.

The thickness of individual cycles ranges from 50 to 200 cm. Most of the cycles are symmetric, and color changes from the light intervals to the darker intervals are gradual and occur over a 5- to 10-cm zone (Fig. 8). Burrows in the darker intervals show a distinct flattening as a result of compaction, whereas burrows in the slightly do-

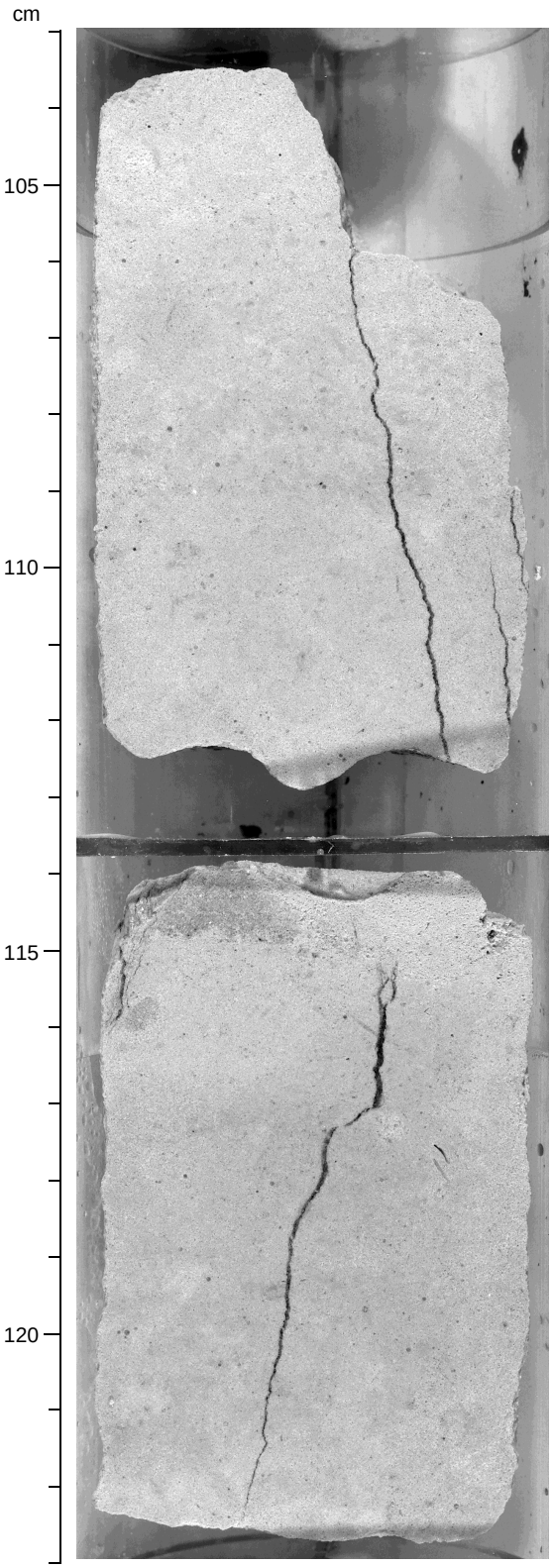

Figure 5. Celestite-filled fractures in the uppermost part of Unit IV (interval 166-1003C-5R-1, 103–123 cm). Note that the lower fracture (115–122.5 cm) was partially eroded before deposition of the overlying sediments.

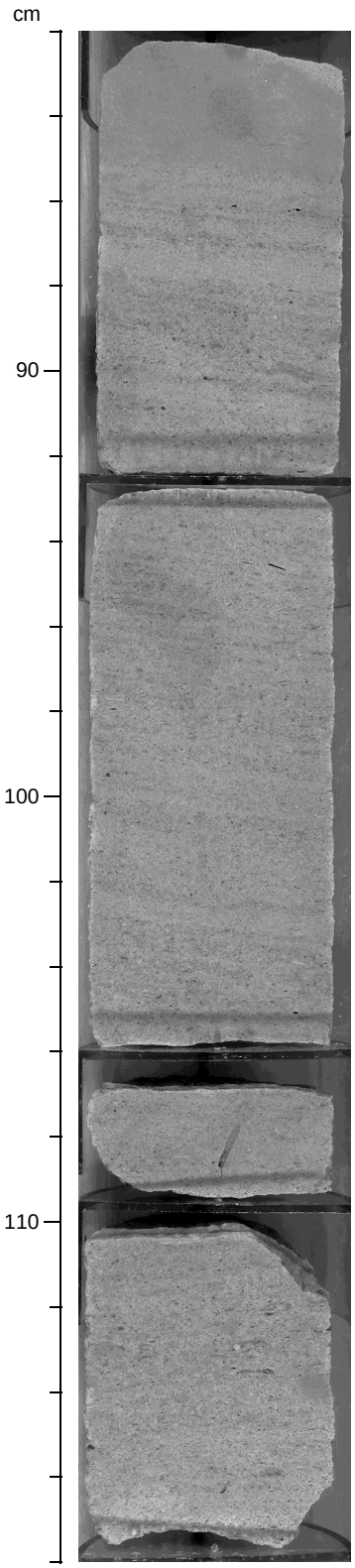

Figure 6. View of a fining-upward, laminated packstone bed of Subunit IVA (interval 166-1003C-9R-3, 82–118 cm). Note intraclasts at 113 and 114 cm and moldic porosity at 94.5 cm (bivalve debris). White dot at 112.8 cm is a miliolid.

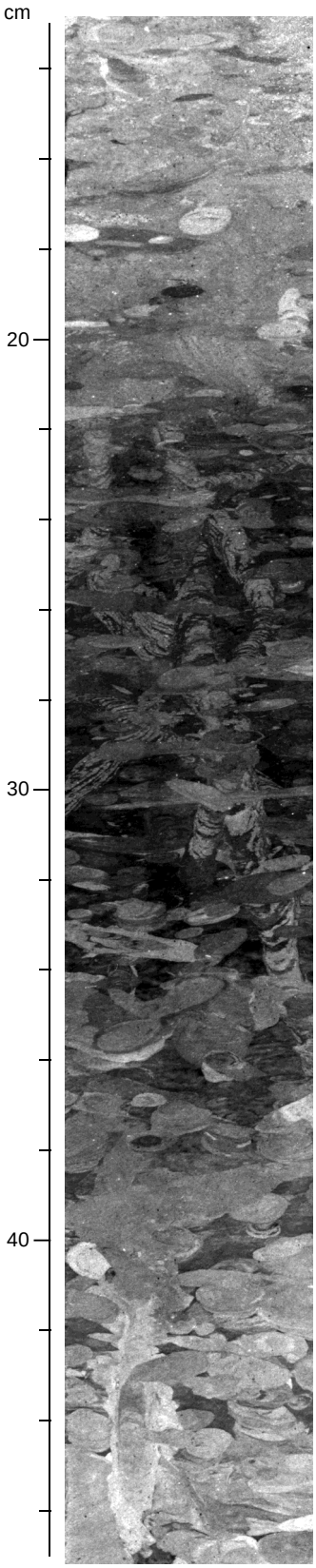

Figure 7. Heavily bioturbated dark gray interval in Subunit IVA (interval 166-1003C-6R-3, 13–47 cm).

lomitic wackestones are well preserved. Some cycles, however show a slight asymmetric pattern as in Core 166-1003C-48R that displays a 60-cm-thick zone with *Thalassanoides*-type burrows in the upper part of the lighter interval. This upper zone displays a well-defined contact to the overlying sediments. Thin-section analysis of Sample 166-1003C-48R-2, 95–99 cm, shows that the light intervals consist of biowackestones with planktonic foraminifers, shell fragments, rotaliid benthic foraminifers, rare peloids, and rare ostracodes.

The darker, greener parts of the cycles yield between 5% to 7% clay (insoluble acid residue). In thin section (e.g., Sample 166-1003C-48R-3, 77–81 cm), these intervals also appear as biowackestones with bioclasts and planktonic and benthic foraminifers (e.g., the neritic genus *Amphistegina*). Bioclasts show a brownish stain, and some planktonic foraminifers show a brownish infill. The biowackestone displays a faint lamination, and bioclasts are rotated due to compaction of the deposits. The base of Subunit VB is placed above a gray packstone with a hardground in Section 166-1003C-40R-1, 60 cm.

Lithologic Unit VI

Interval: 166-1003C-49R-1, 60 cm, through 73R-5, 20 cm
Age: middle to early Miocene
Depth: 915.8–1151.38 mbsf

The top of Unit VI is characterized by a well-defined, irregular surface with borings (hardground). The deposits of Unit VI consist of bioclastic wackestones as well as packstones to floatstones. Based on the occurrence of packstone and floatstone beds, two subunits (VIA and VIB) are differentiated.

Lithologic Subunit VIA

Interval: 166-1003C-49R-1, 60 cm, through 55R-1, 84 cm
Age: middle Miocene
Depth: 915.8–973.38 mbsf

Subunit VIA consists of an alternation between moderately bioturbated greenish grayish wackestones with foraminifers, bioclasts, and darkened grains (lithoclasts) and grayish bioclastic packstones to floatstones. Bioclastic packstones to floatstones are arranged in up to 55-cm-thick, fining-upward beds. Within Subunit VIA, the abundance of these beds decreases downhole. Components in the floatstones and packstones, as determined in thin section (Sample 166-1003C-50R-2, 43–46 cm), include *Halimeda* debris, intraclasts (>3-cm rip-up clasts), bivalve debris (preserved as molds), benthic foraminifers (rotaliids, *Heterostegina*?), planktonic foraminifers, bryozoans, and echinoderm debris.

Bioclastic wackestones of Subunit VIA are moderately to strongly bioturbated. Planktonic foraminifers and bioclasts are the major components of these sediments. Deposits show the same type of cyclicity as described in Subunit VIB. Clay content in the darker intervals averages 1%–4%. In Section 166-1003C-50R-2, 5 cm, a fracture with calcium carbonate occurs (according to the XRD data; see “Inorganic Geochemistry” section, this chapter). The base of Subunit VIA is below the lowest packstone bed in Section 166-1003C-55R-1, 84 cm.

Lithologic Subunit VIB

Interval: 166-1003C-55R-1, 84 cm, through 73R-5, 20 cm
Age: middle to early Miocene
Depth: 973.89–1151.38 mbsf

Subunit VIB consists of gray to grayish green wackestones with foraminifers and bioclasts. Light–dark cycles, as described in Subunit VB, characterize the sedimentary succession of this subunit. In the lower part of the subunit (Cores 166-1003C-72R and 73R), the cycles show a strong asymmetry, which results in bioturbated firmgrounds at the tops of grayish, well-cemented horizons (Fig. 9). Clay content in the darker interval averages 1%–5%. The carbonate content de-

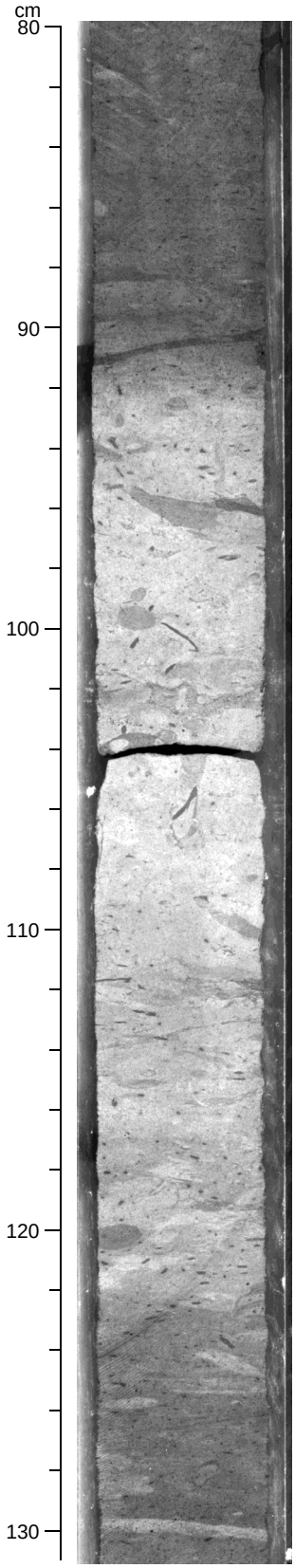

Figure 8. Interval 166-1003C-66R-4, 80–131 cm, shows a well-cemented interval, with large burrows of the cycles occurring in Units VII–IV. Note the gradual changeover from the light, well-cemented zone to the darker, more clay rich part of the cycle.

creases from approximately 95% at the top of Subunit VIB to values in the 80s and some horizons with 40%–50% at the bottom (see "Inorganic Geochemistry" section, this chapter).

Lithologic Unit VII

Interval: 166-1003C-73R-5, 20 cm, through 88R-4, 150 cm
Age: early Miocene
Depth: 1151.38–1296.41 mbsf

Unit VII consists of gray to greenish gray wackestones with foraminifers and bioclasts. A minor lithology consists of black to dark gray siltstones. The occurrence of bioclastic packstone beds differentiates the upper part from a lower part without packstones.

Lithologic Subunit VIIA

Interval: 166-1003C-73R-5, 20 cm, through 78R-1, 27 cm
Age: early Miocene
Depth: 1151.38–1194.77 mbsf

Subunit VIIA consists of gray to dark green foraminifer wackestones that display the same type of cyclicity as the overlying deposits. The subunit is characterized by minor amounts of bioclastic packstone-to-grainstone beds with thicknesses of up to 10 cm. The major components in these beds are foraminifers, bivalve debris, and unidentifiable bioclasts.

Lithologic Subunit VIIB

Interval: 166-1003C-78R-1, 27 cm, through 88R-4, 150 cm
Age: early Miocene
Depth: 1194.77–1296.41 mbsf

Subunit VIIB is the basal sedimentary package recovered at Site 1003. It consists of gray and greenish gray wackestones with bioclasts and foraminifers. Deposits display the light-dark cyclicity described in the overlying units. In intervals 166-1003C-76R-2, 37–44 cm, and 84R-5, 0–2 cm, however, intervals between the gray, well-cemented layers consist of planar laminated, black, muddy siltstones. Clay and silt fractions consist of quartz, feldspar, sponge spicules, radiolarian debris, and calcareous nannofossils. In these darker intervals, carbonate content decreases in some cases to 65%.

Interval 166-1003C-87R-2, 125 cm, to 87R-4, 137 cm, consists of slumped, gray, foraminifer wackestones and laminated, dark gray to grayish green wackestones to claystones. Below this slumped interval, sedimentary cycles as described in the overlying units occur down to the bottom of the cored interval.

Interpretation

Two main sedimentary associations can be distinguished in the sedimentary succession at Site 1003: (1) phases with high amounts of neritic particles exported from the platform, and (2) phases with low amounts of neritic influx leading to pelagic and hemipelagic sedimentation. High neritic input into the basin occurred by two different mechanisms: (1) in the form of typical periplatform oozes that are platform-derived, shallow-water mud and sand mixed with pelagic carbonate; and (2) by turbidity currents that result in the formation of graded, laminated packstone-to-grainstone beds.

At Site 1003, the respective phases of different degrees of neritic input varied through time. Units II to VII record these variations as a large-scale succession, with a repeating pattern of uphole changes in the textures from more matrix-supported sediments to more grain-supported sediments. In most of the successions, this evolution is linked to the occurrence of turbidites in the upper part of the cycles (e.g., Unit V). Each of the successions starts at its base with a phase of starvation of neritic input. These episodes are reflected either as pelagic sediments (calcareous nannofossil-rich sediments) with increased siliciclastic input (lower part) or as firmgrounds and hardgrounds. A preliminary interpretation of this large-scale cyclicity is

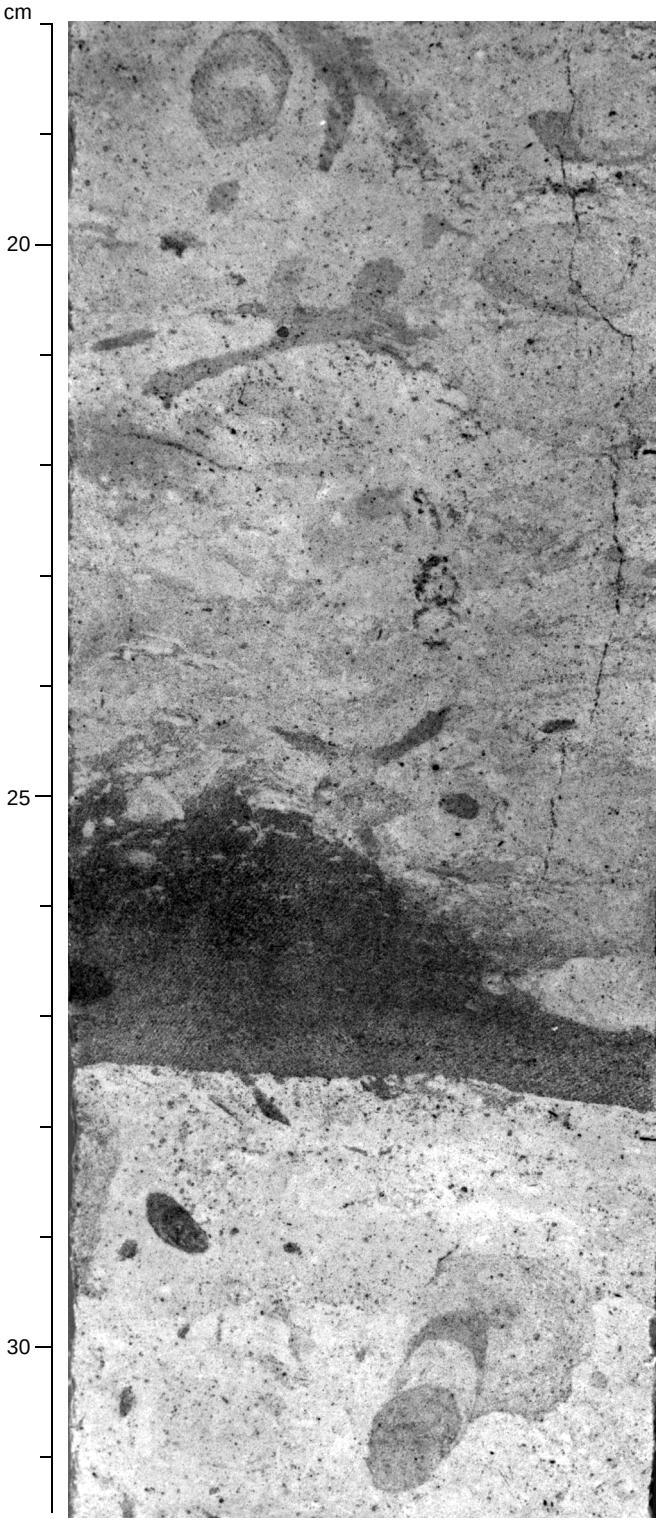

Figure 9. Firmground in the lowermost part of Unit VI (interval 166-1003C-72R-1, 18–31.5 cm). Note the sharp, burrowed contact between light gray wackestones and gray wackestones at 28 cm.

that the starved intervals correspond to phases when platform-derived input decreased either as a result of platform exposure or as a response to backstepping of the neritic carbonate production zone, thus minimizing sediment export to the basin. The gradual change toward more grain-supported textures upsection reflects the gradual progradation of the shallow-water area. On the basis of the preliminary data, it is not possible to state whether the laminated packstones to floatstones (calciturbidites) record only highstand shedding, or if there are also substantial amounts of sediments shed during lowstands. Analyses of the composition of the redeposited beds are needed to solve this question.

Short-term cycles superimposed on the large-scale cyclicity occur from Unit VII through Unit IV. These cycles consist of an alternation of better-cemented beds and less cemented, compacted beds (see, e.g., the description of Subunit VB). A preliminary interpretation of this small-scale cyclicity is that the better-cemented intervals reflect higher neritic input with higher primary aragonite contents. The compacted zones record phases of decreased neritic input, resulting in sediments with fewer metastable carbonates and, thus, lower diagenetic potentials.

In addition to the long-term cyclic evolution of the Bahama Bank, the sedimentary succession at Site 1003 also records an important turnover in the quality of the neritic carbonate production. At the boundary between Units II and I, there is a sudden change from a skeletal association to an association dominated by peloids. This turnover also has been observed from other boreholes in the region (e.g., Hole Clino; Kenter et al., in press; Eberli et al., this volume) and coincides with the ramp-to-platform transition of the Bahama Bank. It indicates a change in the sediment-producing organisms that might be related to changes in the climate or paleoceanography.

BIOSTRATIGRAPHY

Sediments recovered from the three holes cored at Site 1003 provide a record for the Pleistocene through the lowermost Miocene. The abundance of calcareous nannofossils and planktonic foraminifers varies throughout the recovered sequence. Both groups are abundant throughout the Pleistocene interval, but preservation deteriorates in the lower Pliocene sediments and is variable in the Miocene sections. Age-diagnostic calcareous nannofossils provide a well-constrained age model for the upper Pleistocene interval. Both nannofossil and planktonic foraminiferal events were used to date the upper Pliocene sequence. Upper Pliocene calcareous nannofossils and planktonic foraminifers are rare to abundant. The preservation is moderate to poor, with most specimens showing varying degrees of overgrowth. Specimens from both groups are rare with moderate to poor preservation below the upper Pliocene sequence.

Age-diagnostic late Miocene foraminifers of Zone N17 and nannofossils of Zone NN11 were not found at Site 1003, indicating an hiatus near the Miocene/Pliocene boundary. The first occurrence of *Globigerinoides conglobatus* (6.2 Ma) in Sample 166-1003B-38X-CC (352.3 mbsf) and last occurrences of *Discoaster neohamatus*, *Discoaster bellus*, and the large form of R*eticulofenestra pseudoumbilicus* (8.7 Ma) in the adjacent Sample 166-1003B-39X-1, 41–43 cm, (359.01 mbsf) provide a minimum estimate of 2.5 m.y. for the duration of the hiatus. The absence of the nannofossil marker species *Discoaster quinqueramus* in sediments from Site 1003 is consistent with this interpretation, although an interval of poor preservation just above the unconformity at this site is uppermost Miocene at Site 1007.

The lowermost upper, middle, and lower Miocene sediments are characterized by moderately to poorly preserved nannofossils and planktonic foraminifers; abundances vary from barren to abundant. The more terrigenous intervals in the lower Miocene sequence contain more abundant, better preserved microfossils. Stratigraphic subdivisions are based on nannofossil and planktonic foraminiferal biohorizons identified in the Miocene sequence. Three unconformities were found within the Miocene succession (see “Sedimentation Rates,” this section). Dating the recovered, expanded, and well-defined Neogene sedimentary packages, which were deposited in an upper bathyal environment near the edge of the carbonate-producing shallow-water Great Bahama Bank, is possible, although the effects of diagenesis and dilution make it difficult. Most conventional Neo-

gene nannofossil and planktonic foraminiferal datum levels used for deep-sea pelagic sediments are present at Site 1003, and a fine nannofossil-planktonic foraminiferal stratigraphy was established. Bioevents used to assign zonations are listed in Tables 2 and 3.

The Pleistocene section contains well-preserved, in situ benthic foraminiferal biofacies (200–500 m paleodepth) with diverse platform-derived species. The upper Pliocene section contains reworked deep-water Eocene species. The lower Pliocene yields in situ upper bathyal (200–600 m) benthic foraminiferal assemblages with poor to moderate preservation that contain fewer and less diverse platform-derived taxa than in the Pleistocene section. The change from low-diversity, sparse, transported shallow-water benthic foraminifers in the lower Pliocene section to diverse, common, transported shallow-water benthic foraminifers in the Pleistocene reflects a change from a ramp-type platform to a flat-topped platform (Reijmer et al., 1992). Miocene laminated intervals yield transported Oligocene to lower Miocene benthic foraminiferal biofacies that contain several shallow-water taxa.

Calcareous Nannofossils

Calcareous nannofossils in Holes 1003A and 1003B are moderately to poorly preserved except in the uppermost Pleistocene samples and in the lower Miocene clayey samples. Zonal boundaries at Site 1003 are listed in Table 2 and shown in Figure 10.

The first occurrence of *Emiliania huxleyi*, which indicates the NN20/21 boundary (0.25 Ma), occurs in Sample 166-1003A-1H-CC. The last occurrence of *Pseudoemiliania lacunosa*, which defines the NN19/20 boundary (0.41 Ma), occurs in Sample 166-1003A-7H-CC. On the basis of these results, Sample 166-1003A-1H-CC can be correlated with Zone NN21, and the intervals from Samples 166-1003A-2H-CC through 6H-CC and 166-1003A-7H-CC through 13X-CC are assigned to Pleistocene Zones NN20 and NN19, respectively. The lowest occurrence of *Gephyrocapsa caribbeanica* defines the NN18/19 boundary (1.72 Ma) and was found between Samples 166-1003A-13X-CC and 14X-CC. In the stratotype section in Italy, the first appearance of *G. caribbeanica* occurs just above the Pliocene/Pleistocene boundary and is used here to define this boundary. The distribution of calcareous nannofossil flora in Hole 1003B is similar to that in Hole 1003A.

Gephyrocapsa parallela, which first appears just above the Jaramillo Event, was found in and above Samples 166-1003A-9H-CC and 166-1003B-10X-CC. The concurrent range of *G. parallela* and *Reticulofenestra asanoi* is between 0.95 and 0.85 Ma. Because *R. asanoi* was not found in these samples, this level must be younger than 0.85 Ma. Large-form *Gephyrocapsa* spp. (larger than 6 µm) last

Table 2. Calcareous nannofossil bioevents.

Event	Age (Ma)	Interval (cm)	Depth* (mbsf)
B *E. huxleyi* (NN20/21)	0.25	1003B-2H-CC to 1003A-3H-CC	14.14
T *P. lacunosa* (NN19/20)	0.41	1003A-6H-CC to 1003B-7H-CC	57.23
T *R. asanoi*	0.85	1003B-10X-CC to 1003A-11X-CC	86.46
T *Gephyrocapsa.* spp. (large)	1.20	1003A-12X-CC to 1003B-11X-CC	96.98
B *G. caribbeanica* (NN18/19)	1.72	1003A-13X-CC to 1003B-14X-CC	113.19
T *D. tamalis*	2.75	1003B-15X-CC to 1003B-16X-CC	136.51
T *R. pseudoumbilicus* (NN15/16)	3.66	1003A-18X-CC to 1003B-18X-CC	155.79
T *D. neohamatus*	8.7	1003B-38X-CC to 1003B-39X-1, 41–43	359.01
T *D. hamatus* (NN9/10)	9.40	1003B-52X-CC to 1003C-5R-1, 38–40	488.75
B *D. hamatus* (NN8/9)	10.7	1003C-8R-1, 89–90, to 1003C-10R-1, 72–73	531.60
B *C. coalitus* (NN7/8)	11.3	1003C-10R-1, 72–73, to 1003C-13R-1, 48–49	555.10
T *C. floridanus* (NN6/7)	13.2	1003C-34R-2, 128–129, to 1003C-35R-5, 0–3	780.00
T *S. heteromorphus* (NN5/6)	13.6	1003C-42R-CC to 1003C-43R-CC	856.84
T *H. ampliaperta* (NN4/5)	15.6	1003C-63R-CC to 1003C-64R-CC	1058.06
T *S. belemnos* (NN3/4)	18.3	1003C-68R-CC to 1003C-69R-CC	1108.08
B *S. belemnos* (NN2/3)	19.2	1003C-75R-CC to 1003C-76R-2, 41–42	1171.86
B *D. druggii* (NN1/2)	23.2	1003C-82R-3, 70–75, to 1003C-83R-CC	1242.52

Notes: B = base, T = top. * = average depth for the interval; for actual interval depth, see coring summary on CD-ROM. Average depth was used for constructing Figure 10.

Table 3. Planktonic foraminiferal bioevents.

Event	Age (Ma)	Interval (cm)	Depth* (mbsf)
T *G. obliquus*	1.3	1003A-12X-CC to 1003B-12X-CC	98.36
T *G. extremus*	1.77	1003B-12X-CC to 1003B-13X-CC	109.05
B *G. truncatulinoides* (N21/22)	2.0	1003A-14X-CC to 1003A-15X-CC	123.75
T *G. exilis*	2.2	1003A-16X-CC to 1003B-15X-CC	132.70
T *G. miocenica*	2.3	1003A-16X-CC to 1003B-15X-CC	132.70
T *D. altispira*	3.09	1003B-16X-CC to 1003B-17X-CC	142.90
T *Sphaeroidinellopsis* spp.	3.12	1003B-17X-CC to 1003A-17X-CC	147.24
B *G. tosaensis* (N20/21)	3.2	1003A-17X-CC to 1003A-18X-CC	151.27
T *G. margaritae* (N19/20)	3.58	1003A-18X-CC to 1003A-18X-CC	159.33
T *G. nepenthes*	4.18	1003A-22X-CC to 1003A-23X-CC	197.98
B *G. conglobatus*	6.2	1003B-38X-CC to 1003C-39X-CC	355.61
B *N. humerosa*	8.5	1003B-38X-CC to 1003C-39X-CC	355.61
T *G. mayeri* (N14/15)	11.4	1003C-13R-1, 48–49, to 1003C-14R-2, 37–40	561.04
B *G. nepenthes* (N13/14)	11.8	1003C-19R-2, 40–42, to 1003C-20R-2, 13–14	630.52
T *Fohsella* (N12/13)	11.9	1003C-20R-2, 13–14, to 1003C-21R-2, 16–19	641.30
B *Fohsella fohsi* (N11/12)	12.7	1003C-37R-CC to 1003C-39R-CC	802.55
T *Fohsella praefohsi* (N10/11)	13.6	1003C-47R-CC to 1003C-50R-1, 14–16	910.76
T *P. sicana*	14.8	1003C-47R-CC to 1003C-50R-1, 14–16	910.76
B *O. universa* (N8/9)	15.1	1003C-47R-CC to 1003C-50R-1, 14–16	910.76
B *P. sicana*	16.4	1003C-66R-CC to 1003C-67R-3, 114–116	1089.72
T *C. dissimilis*	17.3	1003C-66R-CC to 1003C-67R-3, 114–116	1089.72
B *G. insueta*	18.8	1003C-72R-3, 27–29, to 1003C-72R-3, 34–36	1140.00
B *G. altiapertura*	20.5	1003C-78R-2, 128–129, to 1003C-79R-5, 94–96	1204.13
T *G. kugleri*	21.5	1003C-78R-2, 128–129, to 1003C-79R-5, 94–96	1204.13

Notes: B = base, T = top. * = average depth for the interval; for actual interval depth, see coring summary on CD-ROM. Average depth was used for constructing Figure 10.

appears in the Cobb Mountain Event and was found in Sample 166-1003B-11X-CC.

Samples 166-1003A-14X-CC through 16X-CC and 166-1003B-13X-CC through 15X-CC are characterized by the occurrence of *P. lacunosa* and the absences of *G. caribbeanica* and *Gephyrocapsa oceanica.* The overall abundance of calcareous nannofossils is rare, and discoasters were not found in the samples in this interval, allowing only a tentative correlation to the upper Pliocene Zones NN16 through NN18. Below this interval down to Samples 166-1003A-18X-CC and 166-1003B-17X-CC, calcareous nannofossil assemblages contain *Discoaster surculus, Discoaster asymmetricus, Discoaster pentaradiatus, Discoaster tamalis,* and *P. lacunosa. D. tamalis* last appears in the upper part of Zone NN16 (2.75 Ma), assigning the intervals between Samples 166-1003A-16X-CC and 18X-CC and between Samples 166-1003B-15X-CC and 17X-CC to the lower part of Zone NN16.

Samples 166-1003A-19X-CC through 27X-CC contain abundant specimens of *Sphenolithus abies* and *Reticulofenestra pseudoumbilicus,* which last appear at the Zone NN15/16 boundary (early Pliocene/late Pliocene boundary, 3.66 Ma). As the assemblages in these samples also contain *D. asymmetricus,* this interval is correlated to the lower Pliocene Zone NN14 to NN15. Below this interval, calcareous nannofossils are poorly preserved, and no marker species were found until Sample 166-1003B-38X-CC.

Samples 166-1003B-39X-1, 41–43 cm, 49X-1, 9–10 cm, and 166-1003C-1R-3, 51–54 cm, are characterized by the occurrences of *D. neohamatus, D. bellus,* and large-form *R. pseudoumbilicus.* This interval can be assigned to the lower upper Miocene Zone NN10 (lower part). Samples 166-1003C-3R-2, 27–30 cm, through 8R-1, 89–90 cm, are assigned to the lowermost upper Miocene Zone NN9 on the basis of the presence of both *Discoaster hamatus* and *Catinaster calyculus.* Sample 166-1003C-10R-1, 72–73 cm, is characterized by the occurrence of *Catinaster coalitus,* the lowest occurrence of which defines the Zone NN7/8 boundary. The top of *Coccolithus miopelagicus,* which is situated at the Zone NN7/8 boundary, was also found in Sample 166-1003C-13R-1, 48–49 cm. On the basis of the stratigraphic distributions of these two species, the Zone NN7/8 boundary is placed between Samples 166-1003C-10R-1, 72–73 cm, and 13R-1, 48–49 cm. *Cyclicargolithus floridanus,* which last appears at the Zone NN6/7 boundary, occurs in samples below Sample 166-1003C-35R-5, 0–3 cm. The highest occurrences of *Sphenolithus heteromorphus, Helicosphaera ampliaperta,* and *Sphenolithus belemnos,* each of which defines the lower to middle Miocene nannofossil Zones NN3, NN4, and NN5, were detected in Samples 166-1003C-43R-CC, 64R-CC, and 69R-CC, respectively. The base of S. belemnos, which is situated at the Zone NN2/3 boundary, was found in Sample 166-1003C-75R-CC.

The lowest occurrence of *Discoaster druggii,* which defines the boundary between Zones NN1 and NN2, is not clear because of poorly preserved discoasters. However, *Sphenolithus capricornutus* last appears in Zone NN1, and was found in Sample 166-1003C-83R-CC. Therefore, the Zone NN1/2 boundary is situated between Samples 166-1003C-82R-3, 70–75 cm, and 83R-CC. The bottom three samples from Hole 1003C are characterized by abundant *Cyclicargolithus abisectus,* few to rare *Discoaster deflandrei,* and the absence of Oligocene nannofossil species. On the basis of these results, the bottom of Hole 1003C is correlated to the lowermost Zone NN1, situated just above the Oligocene/Miocene boundary.

Planktonic Foraminifers

Planktonic foraminifers recovered from Site 1003 are generally rare and poorly preserved in the samples examined except for the Pleistocene sequence and the more terrigenous intervals within the lower Miocene sequence. The high carbonate production and shedding from Great Bahama Bank dilute the pelagic biogenic sediment components to the extent that the planktonic foraminifers show scattered occurrences, particularly in the lower Pliocene and/or uppermost Miocene. As a result of the rarity of some age-diagnostic species, it was not always possible to place the zonal boundaries with certainty; however, the timing of the planktonic foraminiferal biohorizons is consistent with the nannofossil biostratigraphy. Samples from all three holes were examined at this site. Planktonic foraminiferal events are listed in Table 3 and shown in Figure 10.

Hole 1003A contains moderately to well-preserved late Pliocene to Pleistocene age planktonic foraminiferal assemblages (Zones N19–22). The base of Zone N22 (2.0 Ma) is located between Cores 166-1003A-14X and 15X on the basis of the first occurrence of the zonal marker *Globorotalia truncatulinoides* in Sample 166-1003A-14X-CC. The first occurrence of *Globorotalia tosaensis,* which delineates the N20/21 boundary (3.2 Ma), was found in Sample 166-1003A-17X-CC. Typically diverse late Pliocene age planktonic foraminiferal faunas, including *Globorotalia limbata, Globorotalia exilis, G. tosaensis,* and *Neogloboquadrina humerosa,* are present in Cores 166-1003A-15X through 17X. Additional useful bioevents, including the last occurrences of *Dendoglobigerina altispira* (3.0 Ma) and *Sphaeroidinellopsis* spp. (3.12 Ma), were identified within this interval in Sample 166-1003B-17X-CC. The first occurrence of *Globorotalia miocenica* lies in Sample 166-1003A-18X-CC, which indicates the lower boundary of Zone N20 (3.6 Ma).

Planktonic foraminifers are rare to common in the upper part of the lower Pliocene sequence, and preservation ranges from poor to good. Planktonic foraminiferal faunas within Cores 166-1003B-18X through 26X are assigned to Zone N19 on the basis of the presence of *Globorotalia margaritae* and *Globorotalia tumida.* The last occurrence of *Globigerina nepenthes* (4.18 Ma) and the lowest occurrence of *G. conglobatus* (6.2 Ma) were found in Samples 166-1003A-23X-CC and 1003B-38X-CC, respectively. It is difficult to place the Miocene/Pliocene boundary on the basis of planktonic foraminifers because *G. tumida* is absent in the lower Pliocene sediment. *G. conglobatus* ranges into the upper Miocene, and therefore, it is possible that uppermost Miocene sediments are above the unconformity.

Planktonic foraminiferal specimens are generally rare and poorly preserved in Cores 166-1003B-39X through 54X, which makes zonal assignment difficult in this interval. Sample 166-1003B-39X-1, 41–43 cm, contains upper Miocene N16 planktonic foraminifers, including *Globorotalia acostaensis, Globorotalia lenguaensis,* and *Globorotalia merotumida.* There is no evidence for the presence of upper Miocene Zone N17 within this interval because *N. humerosa* (first occurrence at 8.5 Ma) is absent. Samples 166-1003C-6R-CC and 8R-CC contain numerous *Neogloboquadrina continuosa* and *G. merotumida* specimens, but no *N. acostaensis.* Zones N15 and N16 are not differentiated in these samples.

The upper/middle Miocene boundary is identified on the basis of the first occurrence of the nannofossil species *D. hamatus.* The first occurrence of *N. acostaensis,* which is time equivalent, is unreliable as a result of its scattered occurrence in this section (see also above). The top of *Globorotalia mayeri* was found in Sample 166-1003C-14R-2, 37–40 cm, marking the upper limit of Zone N14. The first appearance of *G. nepenthes* defines the base of Zone N14 and occurs between Samples 166-1003C-19R-CC and 20R-CC. Zone N13 is the "gap" between the first appearance of *G. nepenthes* and last occurrence of *Fohsella* spp. delineating the lower boundary. In Hole 1003C, only Sample 166-1003C-20R-CC is assigned to this zone.

The middle Miocene *Fohsella* bioseries, which forms the basis for the middle Miocene N9–12 zonation, is represented by most species at Site 1003, except that the early evolution of the lineage is missing. The first occurrence of *Fohsella praefohsi,* which correlates to the lower limit of Zone N11, coincides with the first appearance of *Orbulina universa* in Sample 166-1003C-47R-CC and marks the base of Zone N9. Zones N9 and N10 are absent, indicating that there is either an extremely condensed section or an unconformity within the lower middle Miocene section.

The lower/middle Miocene boundary is identified by the first occurrence of *Praeorbulina sicana* between Samples 166-1003C-66R-CC and 67R-3, 114–116 cm. This level also marks the upper limit of

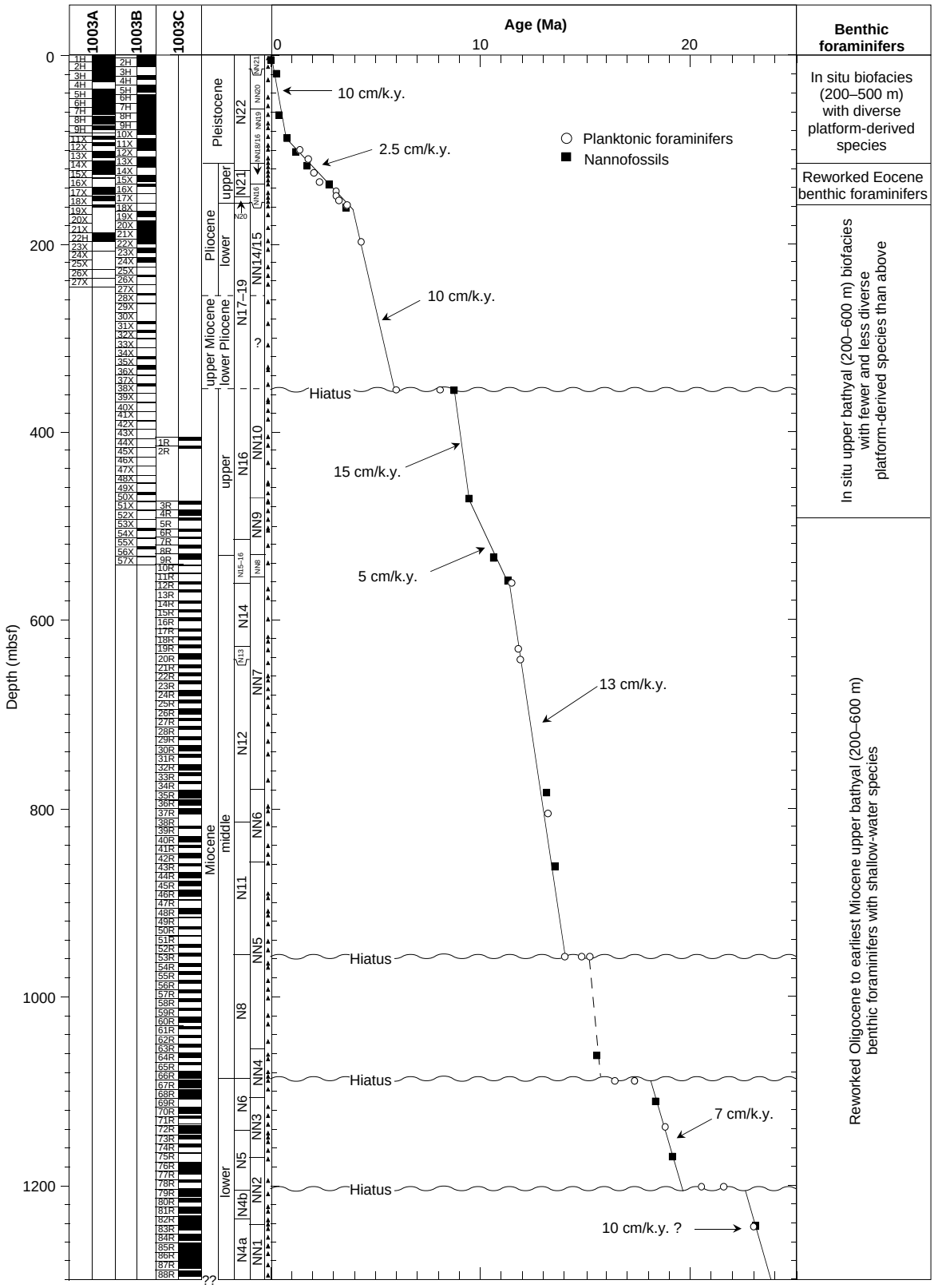

Figure 10. Calcareous nannofossil and planktonic foraminiferal zonation and benthic foraminiferal faunal changes for Site 1003. Recovery for each hole is shown adjacent to the cores (black shading). Solid triangles mark the position of samples examined for stratigraphy and benthic foraminiferal faunas. The age-depth plot is based on the biohorizons in Table 2.

Zone N6. The last occurrence of *Catapsydrax dissimilis*, the indicator of the lower boundary of Zone N7, and the first occurrence of *P. sicana* occur in adjacent samples, indicating that Zone N7 is missing. The first occurrence of *Globigerinatella insueta*, which correlates with the lower boundary of Zone N6, was found in Sample 166-1003C-72R-3, 27–29 cm. The next biohorizon recognized is the first occurrence of *Globigerinoides altiapertura* (20.5 Ma) in Sample 166-1003C-78R-2, 121–123 cm. Rare *Globorotalia kugleri* specimens were found in Sample 166-1003C-79R-5, 94–96 cm. The top of its age range is 21.5 Ma, and thus another hiatus or very condensed section separates Zones N4 and N5.

Samples from the bottom of Hole 1003C are characterized by the presence of the earliest early Miocene planktonic foraminiferal assemblages. The Oligocene/Miocene boundary is indicated by the first occurrence of *G. kugleri*. Only rare specimens of this species were found in the bottom section and cannot be relied upon to mark the boundary. Specimens of Oligocene character occur, including *Globigerina ciperoensis*, but this species is known to cross the boundary. We cannot place the boundary on the basis of the distribution of the age-diagnostic species of planktonic foraminifers.

Benthic Foraminifers

The Pleistocene section at Hole 1003A yields well-preserved benthic foraminiferal faunas that contain *Bulimina marginata* (~30–600 m), *Cibicidoides incrassatus* (~100–600 m), *Planulina foveolata* (~100–500 m), *Planulina ariminensis* (~100–800 m), and *Sigmoilopsis schlumbergeri* (>200 m) (van Morkhoven et al., 1986), indicating a paleodepth of ~200–500 m (within the upper bathyal zone). Other common taxa typical of the upper bathyal assemblages in this section include *Bolivina* spp., *Buliminamexicana, Cassidulina carapitana, Cassidulina laevigata, C. incrassatus, Cibicidoides pachyderma, Fursenkoina* spp., *Globobulimina notovata, Gyroidinoides* spp., *Hoeglundina elegans, Laticarinina pauperata, Lenticulina* spp., *Melonis barleeanum, Nonionella* spp., *Osangularia* sp., *Plectofrondicularia* spp., *Quinqueloculina* spp., *Reusella spinulosa, Siphonina* spp., *Sphaeroidina bulloides, Stilostomella* spp., *Textularia* spp., *Tritaxia* spp., *Uvigerina mediterranea, Uvigerina proboscidea, Vaginulinopsis decorata*, and *Vulvulina spinosa*.

The Pleistocene section also contains diverse, platform-derived shallow-water taxa, including *Amphistegina lessonii, Articulina* sp., *Asterigerina carinata, Baculogypsinoides* sp., *Buliminella elegans, Cornuspira* spp., *Discorbinella* spp., *Discorbis micens, Discorbis* spp., *Elphidium* spp., *Lamarckina scabra, Lenticulina americana spinosa, Neocornubina* sp., *Patelina* spp., ?*Patellinella* sp., *Robertinoides bradyi, Spiroloculina* sp., and *Tretomphalus* spp. Sample 166-1003A-8H-CC contains only *A. carinata*, with no other benthic or planktonic foraminifers present.

Samples 166-1003A-14X-CC and 18X-CC contain upper bathyal Pliocene–Pleistocene faunas with transported deep-water Eocene benthic foraminifers (>1000 m paleodepth; Tjalsma and Lohmann, 1983), including *Aragonia capdevilensis, Bulimina bradbury*, and *Bulimina tuxpamensis*. It is likely that the older specimens were transported from uplifted sections that were exposed on land, possibly from Cuba (Lidz and McNeill, 1995). Core-catcher samples examined from the interval between the samples containing Eocene contaminants yielded depauperate benthic foraminiferal faunas with poor preservation.

Lower Pliocene samples from Holes 1003A and 1003B yield upper bathyal assemblages (200–600 m) with poor to moderate preservation that contain fewer, less diverse platform-derived faunal components than the overlying section (*A. carinata* is the predominant shallow-water contaminant). The in situ Pliocene faunas are also less diverse than the Pleistocene assemblages at Hole 1003A, possibly as a result of poor preservation. In spite of the lower diversity, several species (*C. incrassatus*, ~100–600 m; *Hanzawaia mantaensis*, ~200–1000 m; and *P. ariminensis*, ~100–800 m) indicate an upper bathyal paleodepth (200–600 m). The absence of several paleodepth markers that are present in the Pleistocene section probably reflects their global stratigraphic ranges (e.g., the global first appearances of *B. marginata* [N21] and *P. foveolata* [N18]; van Morkhoven et al., 1986) rather than a paleobathymetric change from the Pliocene to the Pleistocene.

Miocene core-catcher samples from Hole 1003C generally were too indurated to process shipboard for foraminifers. Samples were taken from the uppermost portions of laminated intervals within split cores because these samples were soft enough to be processed. As a result of this sampling bias, Miocene samples examined from Hole 1003C yielded probable in situ benthic foraminifers along with transported Oligocene to early Miocene age deepwater benthic foraminiferal biofacies that contain several shallow-water taxa. The reefal species *A. carinata* and *A. lessonii* are present throughout much of Hole 1003C, and the shallow-water taxon *Elphidium* spp. is present in several samples. The older reworked species (some indicating upper bathyal paleodepths) found in samples from Hole 1003C include *B. tuxpamensis* (last occurrence [LO] N9; >200 m), *Cibicidina walli* (LO N10; 200–600 m), *Cibicorbis herricki* (LO N13; 100–600 m), *Cibicidoides barnetti* (LO N10), *Cibicidoides compressus* (LO N16; 200–1000 m), *Cibicidoides eocaenus* (LO N5), *Cibicidoides havanensis* (LO N10; >200 m), *Cibicidoides micrus* (LO P21b), *Neoeponides campester* (LO N13; 200–600 m), *Planulina ambigua* (LO N5; ~200–1000 m), *Planulina costata* (LO N5; ~200–1000 m), *Planulina mexicana* (LO N13; 100–800 m), *P. subtenuissima* (LO N9; 200–600 m), *Rectuvigerina transversa* (LO N12), and *Siphonina tenuicarinata* (LO N10) (biostratigraphic and paleobathymetric ranges after van Morkhoven et al. [1986] and Katz and Miller [1993]).

Sedimentation Rates

The sediments at Site 1003 yield a large number of biohorizons, from both calcareous nannofossils and planktonic foraminifers, all of which appear in proper succession. This finding is remarkable given the nature of the sedimentary sequences close to a shallow-water carbonate bank. Drilled at the shelf break, the Clino borehole shows evidence that episodic shedding of platform-derived sediments to the margin occurred during sea-level highstands (Lidz and McNeill, 1995). These highstand intervals are unusually expanded as a result of the high sedimentation rates and are interrupted by much thinner intervals with low sedimentation rates (see Eberli et al., this volume). The thinner intervals represent shutdown of the "carbonate factory," when input of material was restricted to pelagic biogenic components and terrigenous material (Kenter et al., in press). On the slopes north of Little Bahama Bank and in Exuma Sound, these condensed sections correlate to eustatic lowstands (Shipboard Scientific Party, 1988).

Age vs. depth is plotted for Site 1003 in Figure 10. The sedimentation rate is high at the top of the section during the last 0.8–0.9 m.y. (10 cm/k.y.). Platform production and shedding began to affect this site at about that time. The lower Pleistocene to upper Pliocene interval shows a much slower sedimentation rate of about 2.5 cm/k.y., suggesting limited platform and pelagic sedimentation. Slow late Pliocene sedimentation was documented at all Leg 101 slope sites and was related to a period of sea-level lowering and, thus, there was no shedding of bank-top derived sediments (Melillo, 1988; Watkins and Verbeek, 1988).

The sedimentation rate in the lower Pliocene and uppermost Miocene–lower Pliocene interval is high at Site 1003, up to 10 cm/k.y., which is a minimal estimate. The duration of the hiatus, marking the lower boundary of this interval, is at least 2.5 m.y., but it may represent a longer period of time. A high sedimentation rate of 15 cm/k.y. was calculated for the upper Miocene (NN10) interval before the hiatus. In contrast, the lower upper Miocene is characterized by "pelagic" sedimentation rates of about 5 cm/k.y. This was a period of global cooling and falling sea level (Haq et al., 1987) that ultimately pro-

duced an unconformity separating the lowermost upper Miocene from the uppermost Miocene–lower Pliocene interval at Site 1003. The unconformity coincides with a lithologic change observed in the cores (see "Lithostratigraphy" section, this chapter).

In general, the middle Miocene shows a very high sedimentation rate, up to 13 cm/k.y. One unconformity was identified within the middle Miocene, coinciding with the lithologic change from Subunit VIA to Subunit VIB (see "Lithostratigraphy" section, this chapter). Planktonic foraminiferal Zones N9 and N10 are missing. A similar unconformity was found at the lower/middle Miocene boundary. Below the boundary, the sedimentation rate is high, similar to that above the boundary. The lowermost unconformity separating lithologic Subunit VIA from Subunit VIB occurs within nannofossil Zone NN2 and straddles the boundary of planktonic foraminiferal Zones N4 and N5. The lowermost Miocene similarly displays a high sedimentation rate.

The Miocene unconformities punctuate periods of high sedimentation rates, during which the input from the platform must also have been high. The significance of the Miocene hiatuses is unclear, but there is an intriguing pattern that may be caused by a combination of sea-level fall and changes in oceanic regime.

PALEOMAGNETISM

Shipboard paleomagnetic measurements were conducted at Holes 1003A, 1003B, and 1003C. As a result of the uncertainty in polarity, unrecovered intervals, low remanence intensity, and magnetometer measurement problems, correlation to the geomagnetic polarity time scale (GPTS) was limited. Two tentative reversal boundaries could be correlated in the upper part of the holes. However, shipboard measurements of these polarity zones are poorly defined and are in need of confirmation. Archive-half cores were analyzed at 10-cm intervals at a 10-mT AF demagnetization level in the pass-through cryogenic magnetometer until the intensity was too low (thought to be about 2 mA/m) to give reliable directional data. Several discrete samples were measured on the spinner magnetometer at the NRM level, but they failed to yield polarity reversals and had intensities that were near the detection limit of the instrument. It was judged that additional AF and thermal demagnetization at a shore-based laboratory were necessary to ascertain reliable polarity.

Magnetic intensities of Holes 1003A and 1003B ranged from about 10 mA/m to less than 0.1 mA/m (Fig. 11). The majority of the intensities were between about 1 and 0.1 mA/m, with slightly stronger intensities near the top 100 mbsf in both cores. These intensities are near the cryogenic magnetometer sensitivity level for reliable intensity and directional data in split-core samples. In Hole 1003C, intensities of lithified sediments were also below the measurement threshold of the cryogenic magnetometer (i.e., <1 mA/m). Therefore, whole-core measurements in the cryogenic magnetometer were discontinued.

One area of interest in the intensity record (and also in the magnetic susceptibility data; see below) was the interval above 100 mbsf. This interval (especially in Hole 1003B) shows two pronounced intensity highs (Fig. 12). These two intensity spikes are near 10 mA/m intensity after 10-mT AF demagnetization. The origin of these intensity spikes is unknown, but it may relate either to a diagenetic zone that produced authigenic pyrite, or to a period of increased iron mobilization that enhanced in situ iron oxide production. The low magnetic intensities throughout most of the core, the generally diamagnetic character of the whole-core susceptibility measurements, and two saturation isothermal remanent magnetization (SIRM) acquisition tests (Samples 166-1003C-68R-2, 10–12 cm, and 88R-1, 54–57 cm; Fig. 13), suggest that the remanence may be carried by single-domain magnetite. The carrier of magnetic remanence, especially in the lower part of Hole 1003C where the clay content increases, will be confirmed by shore-based rock-magnetic study.

A composite magnetic susceptibility record for the three holes at Site 1003 was generated by whole-core MST measurements (Fig. 14, corrected for spikes at core boundaries). Susceptibility was for the most part diamagnetic (negative), which is characteristic of carbonate dominated sediments (see Shipboard Scientific Party, 1991). A proposed fine-grained magnetite remanence carrier is consistent with these diamagnetic susceptibility results, as susceptibility is grain-size dependent in magnetite (Maher, 1988). Several positive susceptibility spikes are prominent in the composite record. The above-mentioned spikes at about 80 mbsf are found in Holes 1003A and 1003B and may represent some distinct geochemical reaction zone. Between about 200 and 1075 mbsf, the susceptibility is predominantly diamagnetic, although numerous positive susceptibility spikes occur. Below about 1000 mbsf, the susceptibility spikes become stronger and more frequent and may be related to clay-rich lithologies in the highly cyclic, white-green limestone successions. These stronger susceptibility cycles may also be related to the input of slightly coarser grained magnetic material of detrital origin, as the carbonate weight percentage drops below 80% in several zones between 1000 and 1300 mbsf.

Magnetostratigraphically, only two possible reversal datums could be tentatively identified in the upper part of Holes 1003A and 1003B. Identification of possible normal and reversed polarities were based on the rather weak criteria of continuous, positive inclination zones for normal polarity and scattered, mixed inclination angles for potential reverse polarity zone (caused by incomplete AF demagnetization of a weak overprint). It should be stressed that these polarity zones need to be confirmed with measurement of the discrete samples. The two possible correlations from the upper part of Holes 1003A and 1003B are the Brunhes/Matuyama reversal boundary (at 0.78 Ma) and perhaps the top of the Olduvai Subchron (1.77 Ma). The Brunhes/Matuyama boundary is tentatively placed at about 77 mbsf (Core 9H) in Hole 1003A and at about 76 mbsf (Core 9H) in Hole 1003B. The predominantly normal polarities above this boundary are correlated to the Brunhes Chron, therefore, with an age less than 0.78 Ma. This correlation is based on several calcareous nannofossil last occurrences (large *Gephyrocapsa* spp. at 1.20 Ma; *Reticulofenestra asanoi* at 0.85 Ma; and *Pseudoemiliania lacunosa* at 0.41 Ma) and one late Pleistocene first occurrence (*Emiliania huxleyi* at 0.25 Ma). Poor core recovery and uncertain inclination values preclude definitive positioning of the boundary based on shipboard measurements alone. The second possible correlation occurs in Hole 1003A in Cores 14X and 15X, where a continuous normal polarity in-

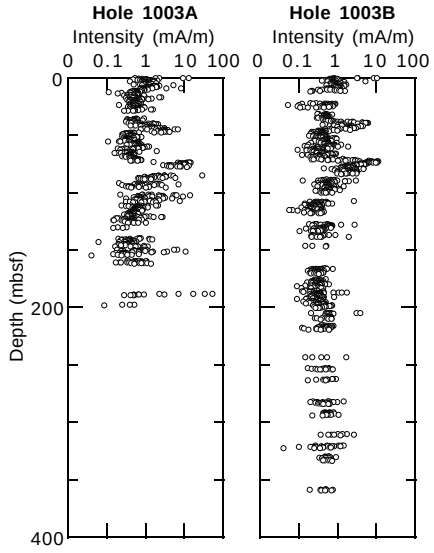

Figure 11. Archive-half magnetic intensity after AF demagnetization at 10-mT for the interval from 0 to 400 mbsf in Holes 1003A and 1003B.

terval was encountered that may be correlative with the top of the Olduvai Subchron (1.77 Ma). The top of this normal polarity interval at 112 mbsf is better defined than the base because of the low recovery. The best biostratigraphic tie-points include the bracketing of the normal polarity zone between the first occurrence of *Globorotalia truncatulinoides* (2.0 Ma) and the disappearance of *Globigerinoides fistulosus* (1.77 Ma), as well as the first occurrence of *Gephyrocapsa caribbeanica* (1.72 Ma) at about 109 mbsf, just above the normal polarity interval, which would be at 1.77 Ma (the top of the Olduvai Subchron). However, this interval in Hole 1003B showed a less definitive polarity.

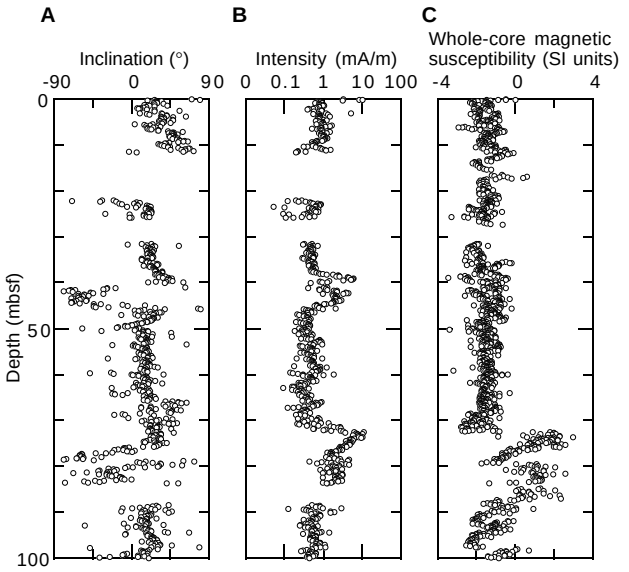

Figure 12. **A.** Inclination after 10-mT AF demagnetization for the interval from 0 to 100 mbsf in Hole 1003B. **B.** Magnetic intensity after 10-mT AF demagnetization in the same interval, showing two intensity peaks, the lower of which could be correlated with Hole 1003A. **C.** Whole-core magnetic susceptibility for the same interval, showing a zone of high susceptibility from 70 to 90 mbsf.

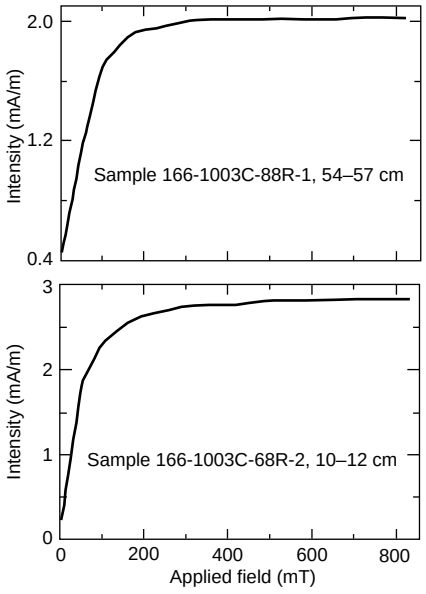

Figure 13. Isothermal remanent magnetization acquisition curve for Samples 166-1003C-68R-2, 10–12 cm (compacted, green foraminifer wackestone) and 88R-1, 54–57 cm (white, foraminifer wackestone). Remanence acquisition is consistent with a fine-grained magnetite, perhaps with a large single-domain component.

ORGANIC GEOCHEMISTRY

At Site 1003, the shipboard organic geochemistry program included determinations of inorganic carbon, total carbon, total nitrogen, total sulfur, and Rock-Eval pyrolysis, in addition to safety monitoring for hydrocarbon gases. The analytical procedures are described in the "Explanatory Notes" chapter (this volume).

Volatile Hydrocarbons

At Site 1003, concentrations of volatile hydrocarbons were routinely measured from every core using the standard ODP headspace sampling technique. Methane (C_1) concentrations showed a steady increase from 11 ppm at 61.6 mbsf to 206 ppm at 118.6 mbsf (Table 4 on CD-ROM; Fig. 15). At greater depths, high methane concentrations (>1000 ppm) were observed between 1024.1 and 1147.5 mbsf. Ethane (C_2) was detected at 71.50 mbsf (Table 4 on CD-ROM), and the C_1/C_2 shows a decreasing trend from 41 at 71.5 mbsf in Hole 1003A to 7 at 1296.4 mbsf in Hole 1003C (Fig. 15).

Higher molecular weight gases (C_{2+}) were detected below 735.3 mbsf down to the base of the hole (Table 4 on CD-ROM). An aromatic odor accompanied each core below Core 166-1003C-30R. The presence of high molecular weight hydrocarbon gases in this interval can be seen in Figure 15, in which the C_1/C_{2+} ranges from 1 to 16. Samples from this lower interval exhibited surface fluorescence when placed in a hexane/ethanol solution. In addition, many of the deeper cores show evidence of oil staining (see "Lithostratigraphy" section, this chapter).

Inorganic and Organic Carbon, Total Sulfur, and Total Nitrogen

Carbonate data for Site 1003 are presented in Figure 16 and Table 5 on CD-ROM. The total carbonate concentration varies from 90 to 99 wt% in the upper 490 m (Pleistocene and Pliocene interval). In the Miocene interval (below 490 mbsf), the carbonate concentration ranges from 32 to 100 wt% (Fig. 16).

Seventy-one samples with low carbonate content were selected for total carbon, total sulfur, and total nitrogen analysis. Total organic carbon (TOC) at Site 1003 varies from 0.0 to 4.1 wt% (Fig. 16). High

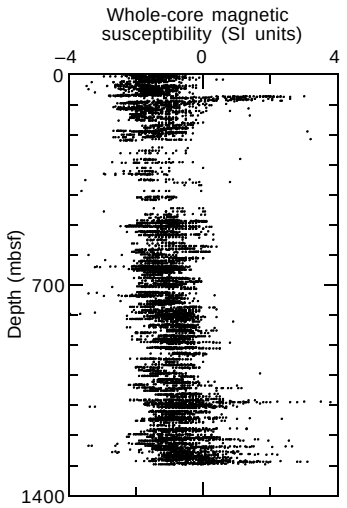

Figure 14. Composite magnetic susceptibility profile from Holes 1003A, 1003B, and 1003C. The data were edited to remove core end effects, such as spikes caused by drilling contamination.

concentrations (>1.0 wt%) in the Pliocene–Pleistocene section occur from 72.91 to 82.41 mbsf in Hole 1003B (73.91 mbsf in Hole 1003A). In the Miocene interval, high TOC enrichment (4.1 wt%) is observed at 773.4 mbsf in Hole 1003C. At greater depths, the TOC concentration decreases to about 1 wt%.

Total sulfur (TS) concentrations are generally low (<1 wt%) in the Pliocene–Pleistocene section. In the Miocene, TS concentrations vary from 0 to 5 wt% (Fig. 16C). Intervals with high TS concentrations (>2 wt%) are confined to the carbonate-poor and dark-colored intervals.

Characterization and Maturity of Organic Matter

Thirty-six samples with TOC greater than 0.5 wt% were characterized by Rock-Eval pyrolysis. The results are reported in Table 6 on CD-ROM and Figure 17. T_{max} ranges from 382° to 428°C at Site 1003, with no systematic increase with depth (Fig. 17). The amount of free hydrocarbons (S_1) increases below 735 mbsf in Hole 1003C (Fig. 17), where light molecular weight hydrocarbons in headspace gases were observed (Fig. 15).

Discussion

The low C_1/C_2 (<100) in the headspace gases below 71.5 mbsf at Site 1003 lies within the abnormal range defined by Emeis and Kvenvolden (1986). This indicates that the hydrocarbon gases below 71.5 mbsf are probably of thermogenic origin. However, the organic matter at Site 1003 is immature with respect to petroleum genesis (T_{max} < 430°C), and therefore indicates that the hydrocarbons were not produced in situ, but migrated from deeper sources.

The original TOC variations in the sediment also seem to be influenced by the migration of hydrocarbons. Enrichments in TOC are normally confined to dark-colored intervals. Samples from dark-colored intervals from Hole 1003C (733.28 and 1143.05 mbsf) also have significantly higher TS concentrations (>2 wt%) compared with samples from greenish and lighter colored intervals (Fig. 18). This may indicate that the majority of the organic matter in the dark intervals originates from the migration of oils rather than in situ organic matter.

The enrichment of C_{2+} in headspace gases and the greater amount of free hydrocarbons (S_1) seen below 735 mbsf in Hole 1003C roughly coincides with the boundary between lithologic Subunits VA and VB at 738.8 mbsf (see "Lithostratigraphy" section, this chapter). Subunit VA is characterized by high sonic velocities (see "Physical Properties" section, this chapter) and may have acted as a seal for vertical hydrocarbon migration.

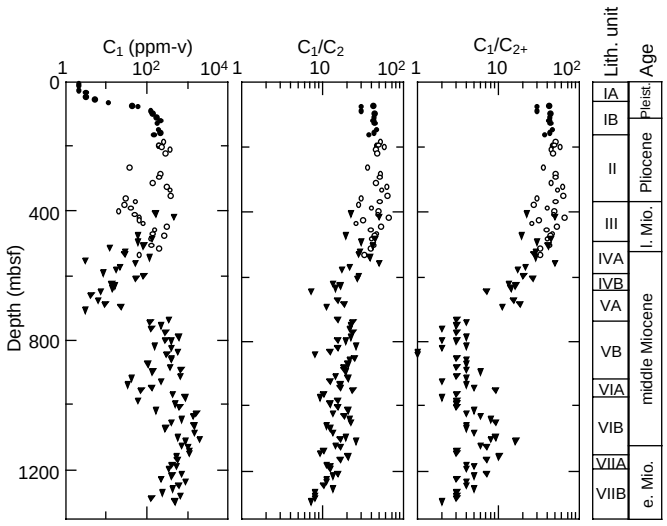

Figure 15. Methane concentrations (C_1), methane/ethane (C_1/C_2) ratios, and methane/higher molecular weight hydrocarbon (C_1/C_{2+}) ratios of headspace gases from Site 1003. Hole 1003A = solid circles, Hole 1003B = open circles, and Hole 1003C = solid triangles.

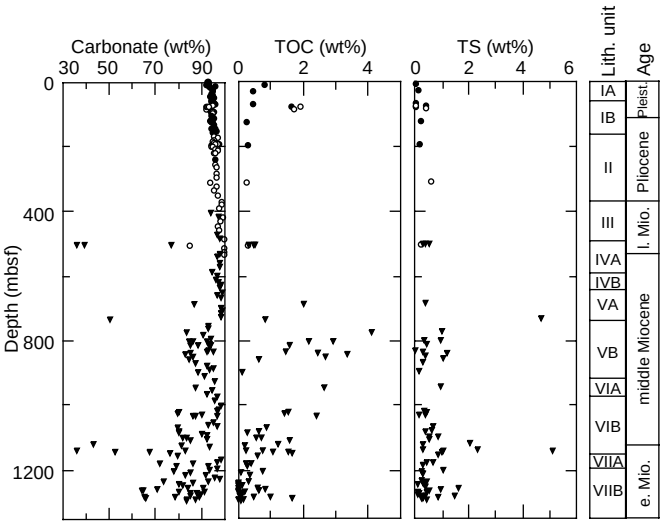

Figure 16. Concentration of carbonate, total organic carbon, and total sulfur at Site 1003. Symbols as in Figure 15.

INORGANIC GEOCHEMISTRY

At Site 1003, 50 interstitial water and surface-seawater samples were collected (Table 7). Concentration gradients of interstitial water parameters (Fig. 19) and profiles normalized to surface seawater (Fig. 20) suggest a combination of localized reaction zones and horizontal fluid flow within lithologic boundaries. The major lithologic boundaries are shown in Figure 19 along with the profiles of dissolved interstitial water constituents.

Approximately 270 samples were analyzed by XRD and subjected to a quantitative determination of bulk carbonate mineralogy. The results are presented in Figure 21 and Table 8 on CD-ROM.

Interstitial Waters

Salinity, Chloride, Sodium, and Potassium

The typically conservative parameters salinity, chloride (Cl^-), sodium (Na^+), and potassium (K^+) exhibit little change in the first 61.5 mbsf of Hole 1003A, but subsequently rise sharply to 200 mbsf (Fig. 19). Gradual increases occur thereafter; a maximum concentration of K^+, near twice that of seawater, is reached near 700 mbsf.

The nearly twofold increase in the normally conservative interstitial water constituents observed at depth in Site 1003 may result from several processes: (1) the horizontal flow of a high-salinity fluid originating on the Great Bahama Bank; (2) the occurrence of chemical reactions involving hydrates (although these normally lead to decreased salt concentrations); or (3) the presence of an evaporitic deposit at depth that leads to an upward migration of a high-salinity brine. The Na^+ profile generally follows that of salinity and Cl^-, although there is an apparent depletion of seawater normalized Na^+ near 200 mbsf and again near 900 mbsf (Fig. 20). Similarly, the dissolved K^+ displays conservative behavior in the upper 800 m of Site 1003, with the seawater normalized concentrations becoming depleted below 900 mbsf (not shown in Figure 20). This depletion coincides with negative gradients in seawater normalized magnesium (Mg^{2+}) and calcium (Ca^{2+}) (Fig. 20).

Table 7. Composition of interstitial waters from Site 1003.

Core, section, interval (cm)	Depth (mbsf)	pH	Alk (mM)	Sal	Cl^- (mM)	Na^+ (mM)	Mg^{2+} (mM)	Ca^{2+} (mM)	SO_4^{2-} (mM)	HPO_4^{2-} (µM)	NH_4^+ (mM)	H_4SiO_4 (µM)	K^+ (mM)	Li^+ (µM)	Sr^{2+} (µM)	F^- (µM)	Fe^{2+} (µM)
166-1003A-	0			36.0	578	501.7	56.3	10.8	30.1			<1	11.1	28	94	72	
1H-1, 145–150	1	7.70	2.17	36.0	580	497	55.9	11.4	29.8	1.5	0.11	56	11.1	28	97	74	4
1H-2, 145–150	3	7.69	2.56	36.0	577	494	55.4	10.8	29.7	0.9	0.08	26	10.7	26	93	75	5
1H-3, 145–150	4	7.71	2.74	36.0	578	498	55.5	10.9	30.6	0.8	0.13	40	10.9	27	94	76	1
1H-4, 145–150	6	7.65	2.68	36.0	578	495	55.6	10.6	29.2	0.9	0.14	42	11.0	26	96		6
2H-1, 145–150	8	7.61	2.79	36.0	576	491	55.5	10.8	30.4	0.9	0.18	51	11.0	30	98	76	6
2H-2, 145–150	10	7.74	2.92	36.0	576	489	55.9	11.0	29.1	0.9	0.17	62	11.2	31	98	78	7
2H-3, 145–150	11	7.67	2.52	36.0	575	496	55.4	10.9	30.6	0.8	0.12	47	10.7	31	99	79	5
2H-6, 145–150	15	7.67	2.40	36.0	574	489	55.5	10.9	30.2	0.8	0.09	69	10.8	28	121	96	5
3H-5, 145–150	24	7.69	2.55	36.0	575	491	55.8	11.6	30.0	0.7	0.10	69	11.1	30	140	105	4
4H-2, 140–150	29	7.69	2.51	36.0	575	487	54.9	11.3	29.3	1.1	0.12	69	11.3	29	119	96	8
5H-5, 140–150	43	7.69	3.16	36.5	582	492	55.3	10.7	29.3	1.0	0.31	74	11.2	31	239	158	7
6H-5, 140–150	52	7.84	5.35	37.0	595	501	55.8	11.2	28.4	1.4	0.71	112	11.6	45	270	193	8
7H-5, 140–150	62	7.84	5.22	38.5	620	522	56.4	9.9	26.1	2.5	1.31	184	11.8	51	409	351	10
8H-5, 140–150	71	7.81	17.79	41.0	655	568	55.9	9.6	22.6	3.4	2.55	260	12.9	71	789	424	8
9H-1, 140–150	75	7.89	18.37	42.0	666	564	54.2	9.5	21.8	4.6	2.77	262	13.5	74	851	443	9
11X-1, 140–150	86	7.87	25.00	43.0	708	585	51.5	10.3	18.7	4.8	3.91	316	13.1	89	1005	499	12
12X-2, 140–150	95	7.95	26.03	44.0	721	610	52.4	10.8	18.0	4.2	4.53	321	14.2	86	999	519	13
13X-4, 140–150	108	7.89	27.82	46.0	743	616	50.2	11.6	16.9	3.1	5.62	325	14.3	94	999	521	11
14X-5, 140–150	119	7.79	25.57	47.0	774	639	49.6	12.2	17.1	3.0	5.29	352	15.5	95	1027	532	13
15X-3, 135–150	125	7.80	28.27	47.0	778	641	48.9	12.2	17.3	3.4	6.81	364	15.4	100	1235	507	12
17X-4, 135–150	146	7.79	26.79	47.5	789	702	48.0	12.4	16.2	2.2	7.10	400	15.7	99	1136	456	13
18X-3, 135–150	154	7.85	27.88	47.0	804	661	47.6	12.8	16.0	2.2	7.83	420	16.0	107	1284	423	10
19X-1, 135–150	161	6.67	27.52	46.0	794	652	47.5	12.6	16.2	11.6	7.23	429	15.5	113	1152	368	13
22H-5, 135–150	195	6.52	29.82	49.5	821	676	48.2	14.6	15.6	10.6	7.82	483	16.4	110	1182	338	12
166-1003B-																	
20X-4, 135–150	181	6.65	30.40	49.5	816	675	47.8	13.7	15.5	10.1	7.81	586	16.1	108	1187	332	12
21X-5, 135–150	193	7.71	29.18	50.0	820	681	48.0	14.0	15.8	7.2	8.04	628	16.4	113	1195	332	25
22X-3, 135–150	199	7.82	27.73	49.0	828	686	48.4	14.3	16.2	14.4	8.22	523	16.4	116	1137	334	12
23X-2, 135–150	208	7.84	27.69	49.5	828	684	48.6	14.3	16.5	13.2	8.15	515	16.7	114	1095	340	11
24X-3, 135–150	219	7.74	25.68	49.5	823	677	49.1	14.7	16.5	1.6	7.66	494	16.3	110	1098	343	13
31X-1, 135–150	283	7.80	18.36	49.0	815	666	52.7	18.1	23.1	1.9	6.12	494	15.8	97	742	318	15
32X-2, 135–150	294	6.70	20.26	51.5	854	703	52.6	20.5	22.2	8.0	6.83	397	16.4	91	796	313	15
35X-1, 135–150	322	7.79	20.82	52.5	867	713	53.8	22.5	22.8	14.4	6.44	464	17.7	94	834	316	21
36X-2, 135–150	333	6.69	19.08	52.0	855	716	54.7	22.3	24.3	7.9	6.02	452	17.0	88	800	307	17
39X-1, 100–117	360	7.71	17.85	53.5	883	730	54.8	23.3	23.0	4.9	5.93	485	17.6	86	854	317	17
48X-CC, 5–15	446			57.0	928	778	53.6	31.4	24.2	3.3	3.69	439	17.8	99	708	239	16
49X-1, 25–40	455	7.75	14.16	57.0	907	757	55.6	31.5	27.9	2.8	3.51	582	17.2	90	749	276	20
50X-1, 135–150	466	7.69	13.95	58.0	952	809	55.5	34.9	28.4	5.5	3.61	728	17.8	89	742	268	21
54X-1, 135–150	504			45.5	744	627	49.3	25.1	24.5	1.4	1.22	766	13.8	98	383	140	
166-1003C-																	
22R-3, 34–44	659			60.0	982	823	58.5	43.6	35.2		1.59	766	17.1	98	557	213	
25R-1, 38–42	685			62.0	995	831	62.2	45.6	38.7		1.22	552	16.7	94	530	209	
30R-4, 35–45	737			60.0	974	813	55.7	41.6	32.1		2.47	754	18.2	99	697	206	
32R-7, 0–16	760			59.0	964	799	54.7	41.1	33.0		2.51	942	16.8	105	791	220	
34R-4, 0–19	774			61.0	1001	848	53.8	43.8	33.0		2.89	1001	18.5	115	788	231	
39R-1, 120–131	820			62.0	1018	854	54.8	43.7	32.2		3.01	997	18.4	128	771	209	
48R-4, 113–126	910	7.72	12.51	60.0	1023	844	44.1	30.3	9.3		3.81	992	18.6	182	1384	285	
58R-1, 58–62	1002			58.0	982	820	33.5	29.0	4.8		10.00	936	16.9	300	2946	278	
60R-3, 0–9	1024			57.5	1005	847	27.8	17.1	2.9		13.10	808	16.5	343	3654	253	
61R-2, 0–10	1032			57.0	974	825	30.0	17.1	4.3		12.26	777	14.6	341	3804	234	
66R-4, 56–70	1084			62.0	1069	902	29.1	19.8	4.0			840	14.5	428	4380	118	

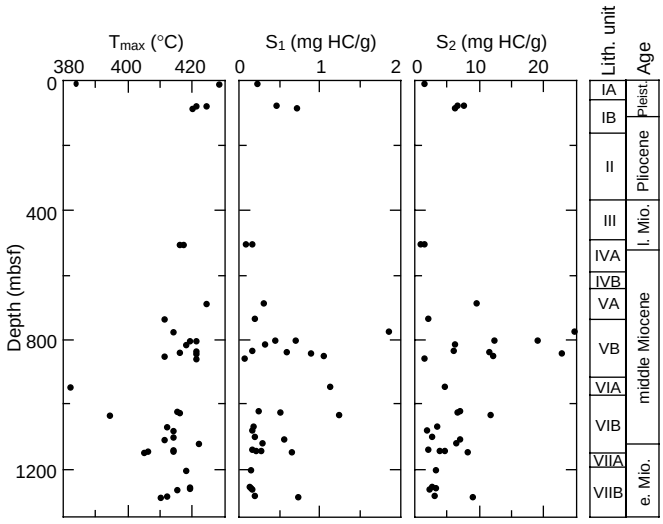

Figure 17. Plot of T_{max}, S_1, and S_2 from Site 1003.

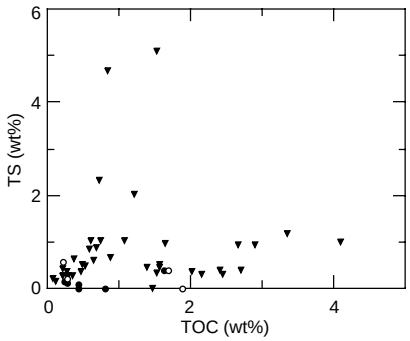

Figure 18. Total organic carbon vs. total sulfur for sediments at Site 1003. Symbols as in Figure 15.

Overall, changes in the Na^+ and K^+ gradients coincide with those of salinity, and Cl^- and appear to be influenced primarily by depth within the sediments and, to a lesser extent, by lithologic boundaries. In the lowermost section of Hole 1003C, the observed decrease in normalized K^+ may possibly be attributed to ion-exchange reactions associated with clay minerals (e.g., Gieskes, 1983; De Carlo, 1992). The zone in which the K^+ concentration begins to decrease coincides with the boundary between lithologic Units V and VI.

Calcium, Magnesium, Strontium, and Lithium

Little change occurs in the concentrations of Ca^{2+}, Mg^{2+}, and Li^+ in the upper 60 mbsf of Site 1003 (Fig. 19). Below 60 mbsf, dissolved Ca^{2+} increases from approximately 11 mM to near 45.6 mM at 645 mbsf. As shown by the increasing normalized Ca^{2+} profile (Fig. 20), this increase is not only due to the increased salinity of the interstitial water. Below 800 mbsf, Ca^{2+} concentrations decrease to a low of 19.8 mM 1084 mbsf.

Increases in dissolved Ca^{2+}, variable concentration gradients downhole, as well as an approximate 25-mM increase in the normalized Ca^{2+} by 700–800 mbsf all suggest that several processes control the concentration of dissolved of Ca^{2+}. Below 700 mbsf within lithologic Units V and VI (see "Lithostratigraphy" section, this chapter), dissolved Ca^{2+} concentrations decrease by nearly a factor of 3 and return to near-seawater concentrations (Fig. 20), whereas the Na^+ and Cl^- content of the interstitial water continues to increase slightly. Over this depth interval, however, the molar Mg^{2+}/Ca^{2+} remains at a relatively narrow range of 1.2–1.7.

The dissolved Mg^{2+} concentration profile (Fig. 19) is relatively flat in the upper 50 mbsf and displays only a small decrease between 60 and 100 mbsf. Normalized Mg^{2+} concentrations indicate a large depletion over the first 100 mbsf of Hole 1003A (Fig. 20), reaching nearly 40% by 200 mbsf. Between 300 and 600 mbsf, dissolved Mg^{2+} returns to a near-seawater concentration of 55 mM, but the normalized Mg^{2+} concentration remains low and subsequently decreases further between 700 and 1083 mbsf. As observed for other major ions, changes in the Mg^{2+} gradient coincide with significant changes in lithology and the occurrence of low-permeability sills (see "Physical Properties" section, this chapter). The low normalized Mg^{2+} concentrations may be explained either by the input of an NaCl-rich fluid or by reactions that remove Mg^{2+} from solution. Magnesium is possibly removed from solution during dolomitization, particularly in the aragonite-rich sediments of the upper 200 mbsf. This interpretation is consistent with mineralogical results (Fig. 21).

Dissolved Sr^{2+} concentrations vary widely at Site 1003, and exhibit the highest concentrations (4.4 mM) measured at any DSDP or ODP site. The previous highest values (~3 mM) were recorded on Leg 133 (Davies, McKenzie, Palmer-Julson, et al., 1991). Strontium concentrations rise sharply to 1.3 mM by 154 mbsf. Between 220 and 680 mbsf, a decrease to approximately 530 µM is particularly apparent in the normalized Sr^{2+} profile (Fig. 20). Within lithologic Unit VI (see "Lithostratigraphy" section, this chapter), a sharp rise occurs from 1.4 mM near 900 mbsf to 4.4 mM Sr^{2+} at 1083 mbsf, and coincides with extensive SO_4^{2-} reduction (discussed below). The latter observation suggests that Sr^{2+} concentrations at Site 1003 are limited by the solubility of celestite ($SrSO_4$) (Baker et al., 1982; Baker and Bloomer, 1988), with the pore-water Sr^{2+} mainly supplied by the dissolution of aragonite (Baker, 1986; Swart and Guzikowski, 1988; Swart and Burns, 1990). Celestite was observed within the interval between 200 and 500 mbsf (see "Lithostratigraphy" section, this chapter), a fact confirmed by XRD analysis.

The dissolved Li^+ concentration profile (Fig. 19) is similar to that of Sr^{2+}, with Li^+ rising from 28 to 116 µM near 200 mbsf. Within lithologic Units V and VI, Li^+ continues to increase, reaching 428 µM by 1083 mbsf. Both the normalized Sr^{2+} and Li^+ profiles are extremely steep in this section of Hole 1003C, suggesting a possible lithologic control. It is possible that both elements are released to the pore water from the sediments during recrystallization of biogenic carbonates, although the abundance of Li in biogenic carbonates may not be sufficient to account for all of the Li^+ observed here (C.F. You, pers. comm., 1996). Dissolved Li^+ concentrations are known to be influenced by (1) the early diagenesis of opal-A, (2) the recrystallization of biogenic carbonate, and (3) reactions involving clay minerals (e.g., Gieskes, 1983). Concentrations of Li^+ at Site 1003 are substantially higher than previously observed in either carbonate-dominated or mixed carbonate/siliciclastic sediments (e.g., Gieskes, 1983; De Carlo, 1992).

Alkalinity, Sulfate, Ammonium, Phosphate, and Iron

The titration alkalinity, ammonium (NH_4^+), and phosphate (HPO_4^{2-}) (Fig. 19) all exhibit similar trends in the first 200 mbsf of Site 1003. Both the alkalinity and NH_4^+ profiles are characterized by broad maxima, with concentrations returning gradually to approximately one-half their peak values by 450 mbsf. Their profiles are slightly offset depthwise from one another, with alkalinity and HPO_4^{2-} reaching their respective maxima at shallower depths than NH_4^+. The offset in the NH_4^+ maxima relative to that of alkalinity may result from the oxidation of CH_4 rather than from in situ marine organic matter. One alkalinity titration performed on a sample collected at 910 mbsf had a value of 12.5 mM.

The sharp increase in alkalinity between 52 and 107 mbsf coincides with a decrease in the sulfate (SO_4^{2-}) concentration over this range. A strong odor of H_2S was also noted upon core recovery. The presence of nearly 2% total organic carbon (TOC) (see "Organic Geochemistry" section, this chapter) in the sediments where the alka-

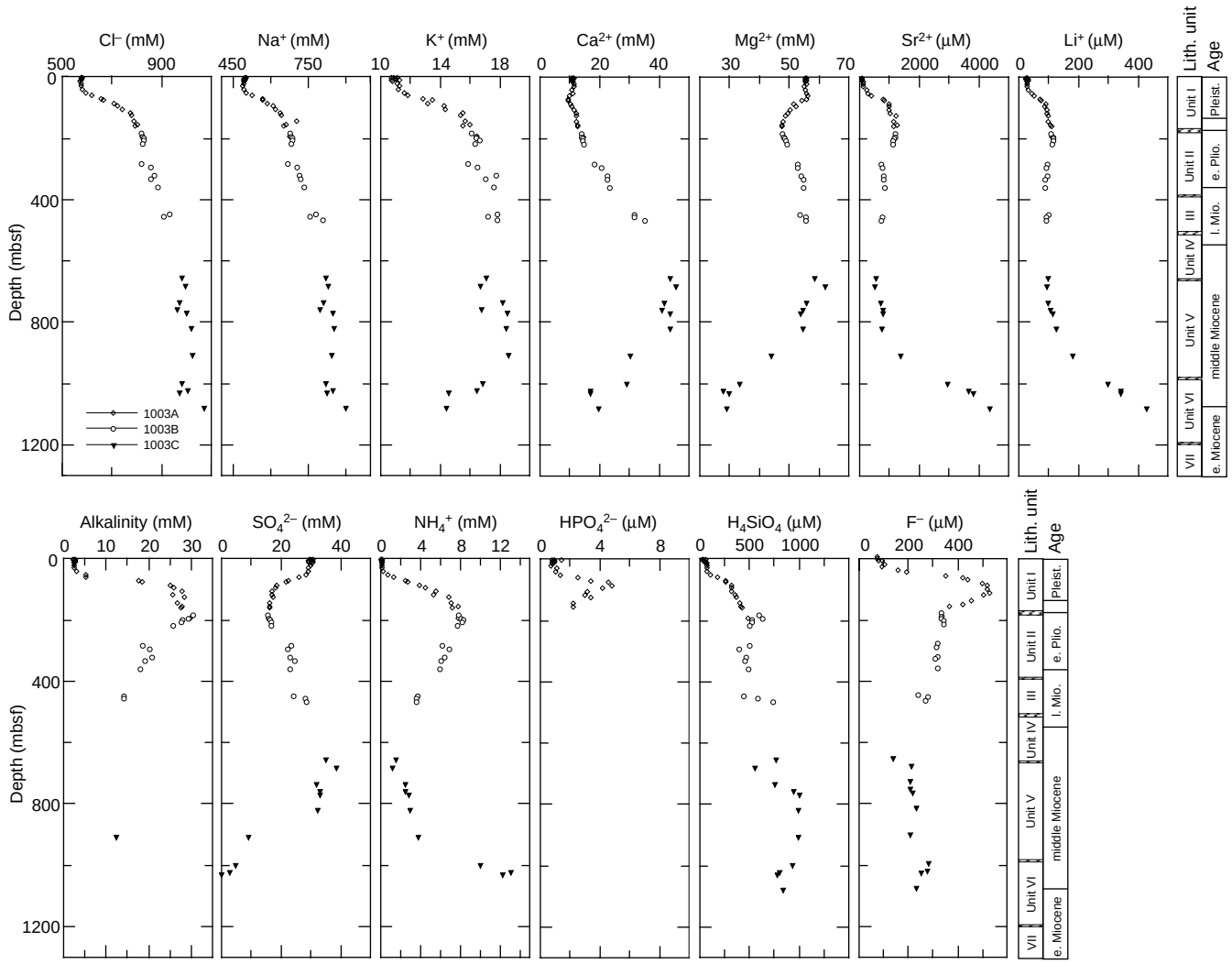

Figure 19. Depth profiles of interstitial water constituents at Site 1003.

linity maximum is observed, suggests that SO_4^{2-} reduction associated with the oxidation of organic matter accounts for the observed trend (e.g., Claypool and Kaplan, 1974). Between 180 and 680 mbsf, sulfate (SO_4^{2-}) concentrations increase to 38.6 mM, although seawater normalized concentrations remain substantially depleted over this interval. Elemental sulfur was observed in the core between 450 and 700 mbsf, immediately above the zone in which SO_4^{2-} becomes nearly depleted and where H_2S, CH_4, and higher weight alkanes increase substantially (see "Organic Geochemistry" section, this chapter). The elemental sulfur may form when H_2S diffuses upward and reacts with SO_4^{2-}.

NH_4^+ concentrations increase gradually in the range of 1.6–3.0 mM between 650 and 820 mbsf. A sharp increase to nearly 13 mM occurs at 1024 mbsf. This increase coincides with the zone in which SO_4^{2-} is strongly depleted and higher molecular weight alkanes are observed (see "Organic Geochemistry" section, this chapter). The NH_4^+ profile may also be controlled by the oxidation of organic matter.

The HPO_4^{2-} concentrations display considerable scatter, with concentrations always below 15 µM. The scatter may be attributed to the presence of HS^-, which interferes with the spectrophotometric determination of HPO_4^{2-}. Possible controls on the concentration of HPO_4^{2-} include oxidation of organic matter, the formation or dissolution of carbonate fluorapatite (CFA), and sorption reactions on $CaCO_3$. The well-defined peak in the HPO_4^{2-} profile within the upper section of Hole 1003A occurs within an interval that contains blackened, possibly phosphatized grains (see "Lithostratigraphy" section, this chapter).

Dissolved iron (Fe^{2+}) was determined on undiluted alkalinity splits of samples collected in the upper 466 mbsf of Site 1003. Concentrations exhibit an increase with depth from approximately 4 to 21 µM. The precision and accuracy of the results may be negatively impacted by large changes in salinity and potential contamination during sample handling associated with the alkalinity titrations. Nonetheless, the observed increase with depth is consistent with the release of Fe^{2+} to solution as the sediments become reducing.

Silica and Fluoride

The dissolved silica (H_4SiO_4) profile (Fig. 19) exhibits several trends at Site 1003. The first trend displays a relatively steady range in concentration from 50 to 75 µM within the first 50 mbsf, followed by an increase to approximately 600 µM by 200 mbsf. The second trend (200–450 mbsf) exhibits slightly lower concentrations near 500 µM. Three closely spaced samples near 460 mbsf form a third trend, with H_4SiO_4 increasing sharply to 738 µM. This suggests that a local maximum in silica may exist near 500 mbsf, just below the boundary of lithologic Units IV and V (see "Lithostratigraphy" section, this chapter). A fourth silica trend occurs deeper in the hole and is characterized first by a decrease to 552 µM at 685 mbsf, a return to values of nearly 1000 µM between 685 mbsf and 800 mbsf, and finally a gentle decrease downhole to approximately 800 µM at 1083 mbsf.

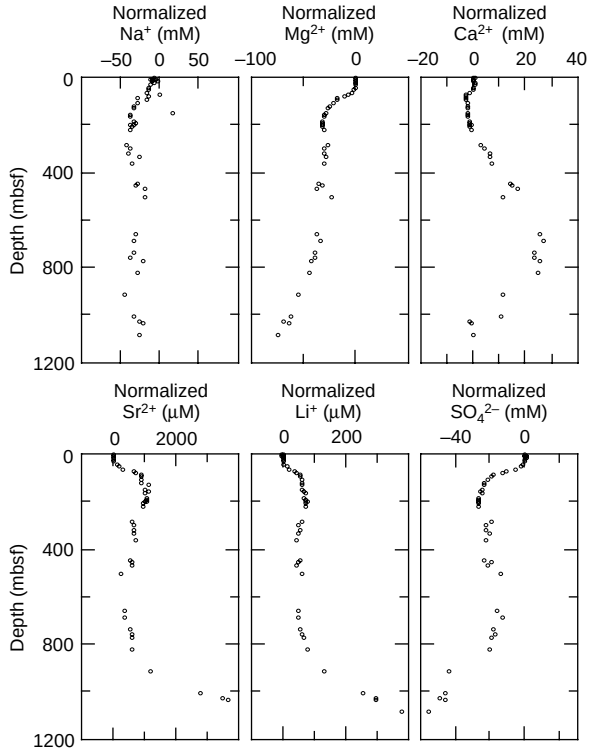

Figure 20. Seawater-normalized depth profiles of selected interstitial water constituents at Site 1003.

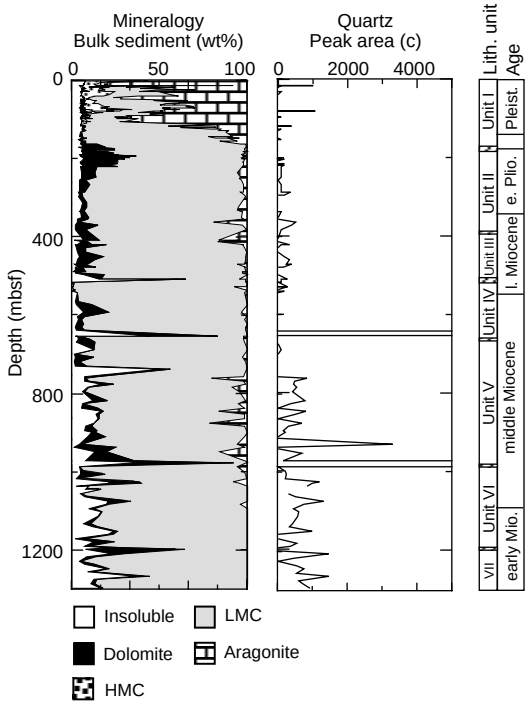

Figure 21. Quantitative X-ray mineralogy of sediments from Site 1003 showing the relative weight percent abundances of carbonate minerals and acid-insoluble residues and peak area counts for the quartz 110 reflection.

Silica concentrations at Site 1003 may reflect early diagenesis of biogenic opal in the upper section of Hole 1003A and a transition from opal-CT to chert in the sparsely sampled sections of Hole 1003C. Siliceous spicules occur in the upper part of Hole 1003A (see "Biostratigraphy" section, this chapter), whereas chertified intervals were observed in a number of cores near 800 mbsf (see "Lithostratigraphy" section, this chapter). Peak concentrations of dissolved H_4SiO_4 (1200 µM) are commonly observed in deep-sea sediments in the transition zones between opal-CT and quartz (e.g., Gieskes, 1983; De Carlo, 1992). Thus, our observations are consistent with the occurrence of the various levels of silica diagenesis.

Summary of Interstitial Water Results

The profiles of interstitial water constituents at Site 1003 are controlled by a number of chemical reactions, including the oxidation of organic matter, the recrystallization of biogenic carbonates to dolomite and diagenetic calcite, silica diagenesis, and possibly ion-exchange reactions in clay minerals and phosphorite formation. In addition, sharp changes in the depth gradients of many constituents, as well as significant departures from reaction-controlled elemental ratios, are suggestive of fluid flow.

Mineralogy

The carbonate mineralogy of Site 1003 (Fig. 21) is dominated by aragonite and low-magnesium calcite (LMC); dolomite and high-magnesium calcite (HMC) are present in lower abundances. Aragonite is most common in the upper 150 mbsf, where it comprises up to 80 wt% of the carbonate minerals. This mineral occurs in lesser amounts downcore. Up to 20 wt% HMC occurs within the upper 100 mbsf, although trace amounts are present to 150 mbsf. Small amounts of dolomite were found between 50 and 150 mbsf. Below 150 mbsf, significant amounts (up to 60 wt% in selected intervals) of dolomite were measured. Below 150 mbsf, aragonite needles were observed only in brownish sediments (see "Lithostratigraphy" section, this chapter) that were typically softer (less lithified) than the dolomite-rich intervals.

Celestite ($SrSO_4$), sulfur, and quartz were also observed by XRD. Although weak quartz reflections were observed in most samples analyzed throughout the sedimentary column, only two samples exhibited greater than 5 wt% quartz. These samples are from two very dolomite-rich intervals near 650 and 975 mbsf (Fig. 21) in which quartz accounts for greater than 50 wt% of the composition. This most likely represents cryptocrystalline quartz because large quantities of detrital quartz do not occur at this site. The occurrence of cherts and/or quartz near 800 mbsf is consistent with the observed dissolved silica profile.

Although the mineralogical analyses performed did not quantify the abundance of clay minerals present in Hole 1003C, qualitative observations suggest that they may increase downcore. For example, a cyclicity between hard grayish-white layers and less lithified and finely laminated greenish material was observed in middle Miocene sediments at Site 1003 (see "Lithostratigraphy" section, this chapter). Four samples exemplifying a single cycle were subjected to qualitative XRD after dissolution of the carbonate minerals with dilute HCl. All four samples contain 15-Å smectite, with a higher abundance in the greener layers. Total carbonate accounts for approximately 90% of the material in this particular core interval (see "Organic Geochemistry" section, this chapter).

PHYSICAL PROPERTIES

Measurements of physical properties at Site 1003 were made on whole cores utilizing the MST and on discrete samples from split cores. Thermal conductivity was measured only on unconsolidated whole-round cores. The vertical spacing of the MST measurements

was maintained at 15 cm for the NGR and at 5 cm for velocity, GRAPE density, and magnetic susceptibility. The NGR sensor was switched off in sediments with a gamma-ray emission below the background level of 6 cps. In indurated sediments, the PWL on the MST was switched off. The frequency of the discrete velocity measurements in the unconsolidated and consolidated intervals was two per section, with one sample per section taken for index properties. In the semilithified to lithified sediment, the intervals between the velocity measurements decreased to 10 to 20 cm.

The following descriptions focus on the downhole variation in petrophysical properties and their correlation with lithostratigraphy. Downhole trends in thermal conductivity will be described separately. Variations in magnetic susceptibility are described in the "Paleomagnetism" section (this chapter).

Index Properties, GRAPE Density, and *P*-Wave Velocity

Tables 9 through 14 on CD-ROM summarize the index properties, GRAPE density, discrete velocity measurements, and NGR for Site 1003. Figures 22 and 23 show the combined results of the petrophysical measurements for the entire Site 1003 and the shallow interval, down to 200 mbsf, respectively.

P-wave velocity shows large positive deviations downhole from a gradual, nearly linear baseline gradient of approximately 0.1 km/s per 100 m (solid line in Fig. 22). Similarly, porosity shows an inverse trend, with large negative excursions on a downhole baseline trend of –2.5%/100 m. The deviation from these baseline trends varies in different intervals downcore, which allows us to define five petrophysical units (Figs. 22, 23), each characterized by a specific trend in petrophysical properties. In most cases, the petrophysical units have sharp, abrupt boundaries that correspond to lithologic unit boundaries and hiatuses in biostratigraphy.

Petrophysical Unit I extends down to 370 mbsf. *P*-wave velocity from the DSV (solid line in Fig. 22) shows a nearly linear increase with depth from 1.5 km/s at the seafloor to 1.8 km/s at approximately 200 mbsf. Three deviations are observed in the other petrophysical properties. First, a sharp, abrupt downcore increase of density from approximately 1.6 to 1.9 g/cm^3 at the base of petrophysical Subunit Ia (12 mbsf) correlates to a downcore increase in grain size. The base of this unit also coincides with an interval that may represent the Pleistocene/Holocene boundary. Second, a downcore decrease in density and coeval positive shift in magnetic susceptibility are observed at 70 mbsf, within petrophysical Subunit Ib (12–118 mbsf). These shifts correlate with a downcore change from unconsolidated to partially lithified sediment and an increase in grain size. Third, a minor positive deviation in velocity, with values up to 2.5 km/s, is present in the interval between approximately 120 and 152 mbsf (petrophysical Subunit Ic; Fig. 23). Its base correlates with the base of lithologic Unit I and represents a downcore lithologic change from foraminifer wackestone to packstone to foraminifer nannofossil chalk. Petrophysical Subunit Id ranges from 152 to 370 mbsf and shows a gradual downcore increase in sonic velocity up to approximately 1.9 km/s, a density of 2.0 to 2.2 g/cm^3, and a decrease in porosity to 45%. The boundary to petrophysical Unit II is marked by an increase in the range of petrophysical properties. The boundary between petrophysical Units I and II coincides with the lithologic transition from lithified pack- to grainstone of lithologic Unit III to the overlying foraminifer nannofossil chalk of Unit II (see "Lithostratigraphy" section, this chapter).

Petrophysical Unit II (370–730 mbsf) has two subunits that are each characterized by a downcore increase in velocity. Both porosity and density show corresponding decreasing and increasing trends, respectively, over the same interval. Near the top of Subunit IIa (370–530 mbsf), velocities are between 1.5 and 4.0 km/s, densities between 1.9 and 2.3 g/cm^3, and porosities range from approximately 35% to 50%. Downcore, velocities increase to values of between 2.0 and 5.0 km/s. Similarly, porosity decreases to values between 10% and 45%. The top of the lower high-velocity zone in petrophysical Subunit IIa (at about 480 mbsf) coincides with the transition from lithologic Unit III to Unit IV and the upper Miocene to lower Pliocene boundary.

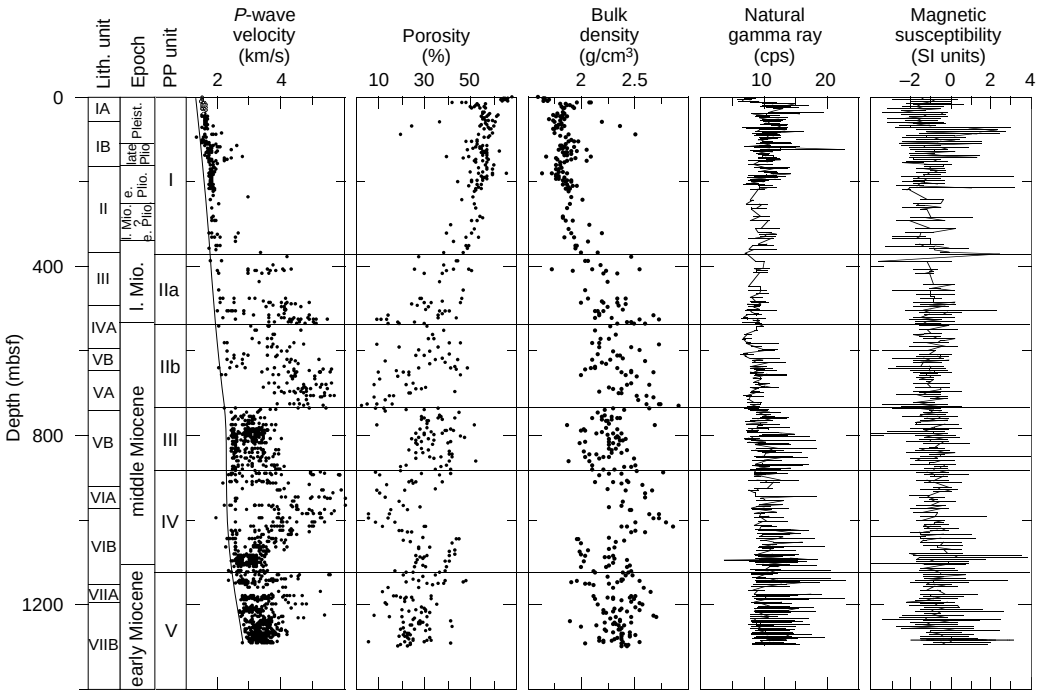

Figure 22. Combined plot of *P*-wave velocity from discrete measurements using the DSV and velocity frame, porosity, bulk density, NGR, and magnetic susceptibility from Holes 1003A, 1003B, and 1003C. Lithologic units and downhole anomalies in velocity, density, and porosity are indicated along with age.

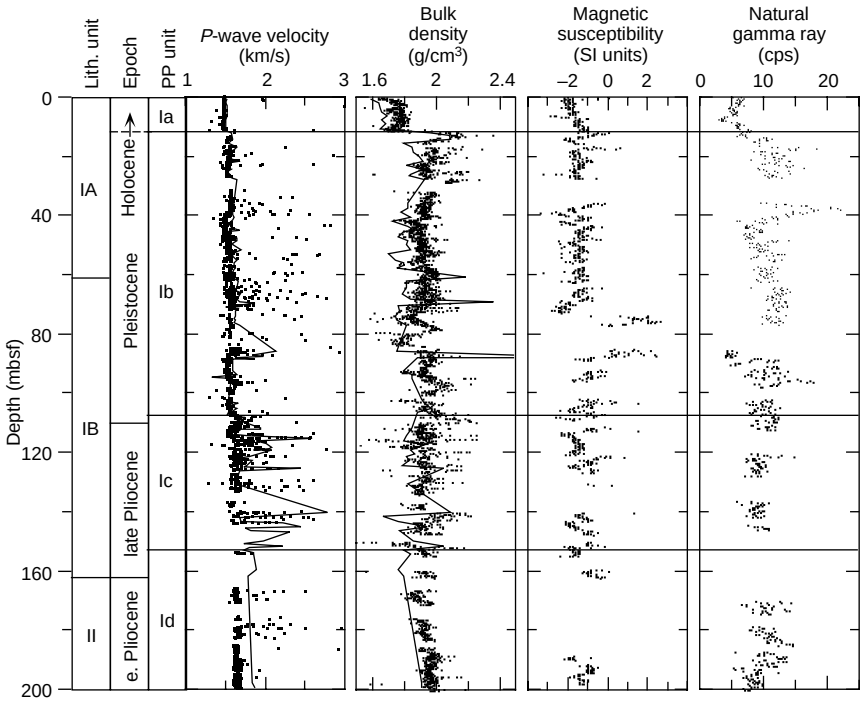

Figure 23. Summary of *P*-wave velocity and bulk density (discrete measurements [solid lines] and MST-data [dots]), magnetic susceptibility, and natural gamma ray for the interval to 200 mbsf. GRAPE density, PWL velocity, and magnetic susceptibility include data from Holes 1003A and 1003B. GRAPE density values were corrected for the mass-attenuation effect of water in high-porosity sediments (see "Explanatory Notes" chapter, this volume).

Subunit IIb shows a similar trend in petrophysical properties: a gradual downcore change to higher velocities and densities and lower porosities. The boundary between petrophysical Subunits IIa and IIb corresponds to the presence of numerous firmgrounds and hardgrounds near the top of lithologic Subunit IVA. The upper part of the high-velocity zone at the base of Subunit IIB (at approximately 630 mbsf) occurs just above the boundary between lithologic Unit IV and Unit V. This boundary is marked by a downcore transition from packto grainstone to wackestone to packstone and by the occurrence of turbidites. The downcore transition of petrophysical Subunit IIb (530–730 mbsf) to the underlying Unit III is characterized by the most abrupt and significant changes in velocity, porosity, and density. The velocity range decreases downhole from 4 to 5.5 km/s at the base of Subunit IIb to 2.2 to 4.0 km/s in the top of Unit III. Porosity and density show a similar abrupt change across this boundary. This petrophysical boundary (at 730 mbsf) coincides with the transition from lithologic Subunit VA to Subunit VB, a downcore change from foraminifer wackestone with abundant turbidites to massive packstone to grainstone.

Petrophysical Unit III (730–880 mbsf) has a constant and narrow velocity range from 2.5 to 4.0 km/s, porosity variation between 20% and 45%, and density between 2.1 and 2.6 g/cm^3. Unit III corresponds to lithologic Subunit VB, which consists of alternating greenish and white foraminiferal wackestone. The transition to underlying petrophysical Unit IV is an abrupt shift to higher velocities, ranging from 2.1 to 6.0 km/s. This transition coincides with a gradual downcore change from wackestone to mudstone, about 40 m above the boundary between lithologic Subunit VB and Subunit VIA.

Petrophysical Unit IV (880–1120 mbsf) shows a downcore decrease in velocity range from 2.5 to 5.0 km/s near the top toward 2.5 to 3.5 km/s at the base. In this unit, porosity changes in a similar manner, from 15 to 20% near the top to 25% to 40% at the base. The lower boundary with petrophysical Unit V (1120 to approximately 1290 mbsf) is sharp and abrupt. It is approximately 30 m above the transition from the fine-grained wackestone of lithologic Unit VI to the wackestone with turbidites of the underlying Unit VII. The transition between petrophysical Unit IV to Unit V is close to the lower to middle Miocene boundary.

Petrophysical Unit V has a downcore-decreasing velocity range, from approximately 2.5 to 5.5 km/s near the top toward 3.0 to 4.0 km/s near the base. Porosity shows a similar pattern, whereas density shows only a subtle decrease. The lower interval of petrophysical Unit V corresponds to the foraminiferal wackestone of lithologic Subunit VIIB.

An example of the high-frequency lithologic and petrophysical variations that are typical for lithologic Subunits IVB, VIB, and VIIB is presented in Figure 24. The alternation of burrowed light gray and greenish wackestone is clearly reflected in measurements of color intensity, natural gamma intensity, sonic velocity, bulk density, and magnetic susceptibility (see also "Lithostratigraphy" section, this chapter). White layers have higher density and velocity values, up to 2.0 g/cm^3 and from 2.5 to 3.5 km/s, respectively, than the greenish layers, which are characterized by density and velocity values of about 1.8 g/cm^3 and 2.5 km/s, respectively. Excursions in gamma-ray intensity within this core are well above the background value of 6.0 cps and range from 12 to 18 cps in the light gray layers to less than 10 cps in the greenish wackestone. As visible on the petrophysical and lithologic logs, the boundaries between the layers are gradual. Variations in magnetic susceptibility may vary locally and are not as clearly defined.

Shear Strength

Shear strength at Site 1003 was measured using the miniature vane shear device. Measurements were made for Hole 1003A down to a depth of 115 mbsf, where the sediment became semilithified and was no longer suitable for shear-vane testing. Measurements are listed in Table 15 on CD-ROM.

Shear strength at Site 1003 generally varies between 5 and 35 kPa and does not show an increase with depth as would be expected considering compaction effects (Fig. 25). In the first 10 mbsf, the strength follows a "reversed" consolidation trend (i.e., the S_u/P_o' decreases sharply from more than 8 to less than 0.2). The interval between approximately 45 and 115 mbsf has overall low and constant S_u/P_o' ratios, which usually fall well below 0.1. In contrast, the shallow section between 0 and 45 mbsf has S_u/P_o' ratios that are about 0.2

or as high as 4. Zones of elevated undrained shear strength are present in the following intervals: the first 10 mbsf, approximately 40 to 45 mbsf, at about 75 mbsf, and between 105 and 110 mbsf. Variations in *P*-wave velocity from the MST, GRAPE density, and mineralogy coincide with several of these strength excursions. Three of the strength anomalies (0–10, 40–45, and 105–110 mbsf) correlate positively with changes in density, velocity, and mineralogy. The percentage of aragonite (see "Inorganic Geochemistry" section, this chapter) seems to have a strong effect on shear strength, density, and velocity. Although sedimentation rates calculated from biostratigraphy (see "Biostratigraphy" section, this chapter) indicate a sharp decrease downcore from approximately 55 to 80 mbsf, no coeval change in shear strength was observed.

Thermal Conductivity

Thermal conductivities were measured on cores from Holes 1003A and 1003B. At Hole 1003A, 38 measurements were performed from 0 to 160 mbsf. At Hole 1003B, 41 measurements were made from 0 to 100 mbsf. Results are shown in Table 16 on CD-ROM and Figure 26. The conductivities for the upper (<10 mbsf) cores are between 0.98 and 1.1 W/(m·K). There is little variation in conductivity between 10 and 100 mbsf, with values of approximately 1.2 W/(m·K). Data from the deeper (>100 mbsf) cores are scattered between 1.1 and 1.7 W/(m·K). This distribution pattern is quite similar to the bulk density and water content. The average and the standard deviations of all the conductivity measurements at this site are 1.17 and 0.12 W/(m·K), respectively.

DOWNHOLE LOGGING

Logging Operations

After drilling operations ended at Hole 1003D, the borehole was prepared for logging (see "Operations" section, this chapter). The lower limit of the bottom-hole assembly (BHA) was placed at 105 mbsf and maintained at this position except during the end of the last logging run to avoid destabilization of the upper part of the hole. We deployed five logging tool strings, in the following order: (1) induction-sonic-temperature (NET/SDT/DIT/TLT), (2) Formation MicroScanner (FMS), (3) integrated porosity-lithology tool (IPLT), (4) geochemical logging tool (GLT), and (5) well seismic tool (WST) (see "Downhole Logging" section, "Explanatory Notes" chapter, this volume). All five tool strings reached the total depth drilled (Fig. 27). Because of time constraints and hole quality, the GLT was run only between 450 and 1050 mbsf.

The WST recorded stacks of five to seven air gun shots at 20 stations spaced about 50 m apart. The resulting interval velocities and time-depth curve are discussed in the "Seismic Stratigraphy" section (this chapter).

Data Quality

Hole conditions provided high-quality logging data between 350 and 1050 mbsf in Hole 1003D. For most of the interval above 350 mbsf, the hole is enlarged beyond the maximum caliper aperture of both the hostile-environment Litho-Density Sonde (HLDS) in the IPLT string (~16.5 in or 42 cm) and the FMS (~15 in or 38 cm). The

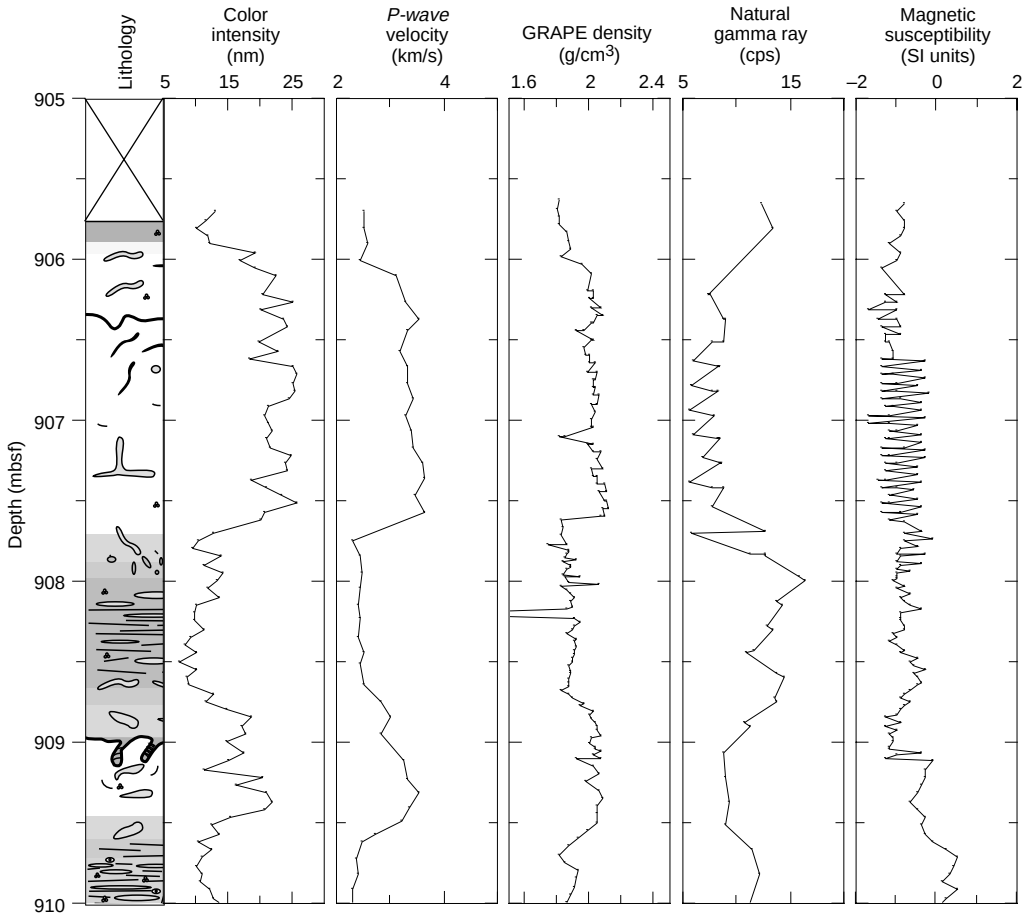

Figure 24. High-resolution profile of lithology, color intensity, velocity, GRAPE density, natural gamma ray, and magnetic susceptibility of Core 166-1003C-48R. See text for discussion.

enlarged borehole in this interval degraded the quality of the logs, in particular the density, porosity, gamma ray, and FMS. The resistivity and sonic logs appear to have been less affected by the enlarged borehole.

Comparison of the logging data with index properties measurements indicates that abnormally low values of density and porosity were logged for most of the interval above 250 mbsf (Fig. 28). Measurements of core velocity appear to be too low compared with the sonic log in the less indurated intervals, whereas in the indurated intervals core velocities tend to be higher than the logging values. This discrepancy probably results from the limited vertical resolution of the sonic tool compared with core measurements in combination with the fact that in soft sediments the laboratory measurements do not reproduce in situ conditions (see "Physical Properties" section, this chapter).

FMS images analyzed on board are of good quality, displaying fine-scale bedding over most of the logged section. At Site 1006, caliper groove marks made on the borehole wall by the HLDS tool in the IPLT string were imaged by the FMS. To prevent this problem at Site 1003, we deployed the FMS string before the IPLT string.

Preliminary Observations

Geophysical and geochemical data acquired during the logging of Hole 1003D in the interval from 105 to 1050 mbsf provide detailed information on the sedimentary properties and structure of the strata that cannot be obtained from the recovered material. As sediment recovery below 105 mbsf was variable, averaging about 45%, these logs can provide extremely valuable information about Site 1003 that can be correlated with data gleaned from the incomplete core record. Log-to-core correlation permits significant interpretation about variation in the sedimentation patterns adjacent to Great Bahama Bank from the earliest middle Miocene (approximately 15.9 Ma) to the present. The changes recorded in the logs can be traced eastward to the Great Bahama Bank along the seismic sequence boundaries, providing a tie of the sedimentation patterns at Site 1003 to other drill sites across the platform margin and on the platform top.

Figures 28, 29, and 30 contain compilations of the logged data plotted against depth in the section and related to core recovery, biostratigraphic age, lithologic units, and physical property laboratory data measured in discrete samples and whole-core sections. The compatibility of the discrete points with the data obtained from the total logged interval supports the integrity of the data sets. In particular,

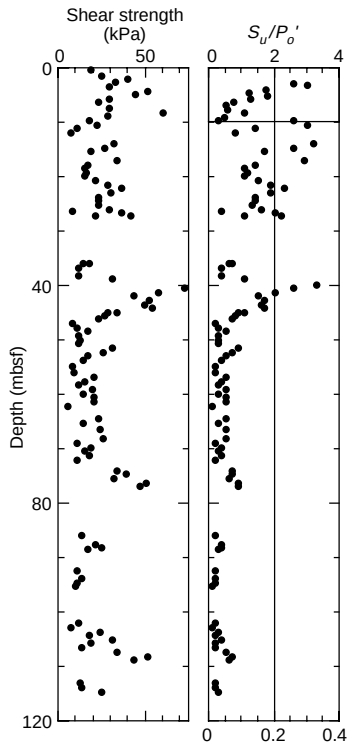

Figure 25. Shear strength and S_u/P_o' calculated from shear strength and overburden stress for cores from Hole 1003A.

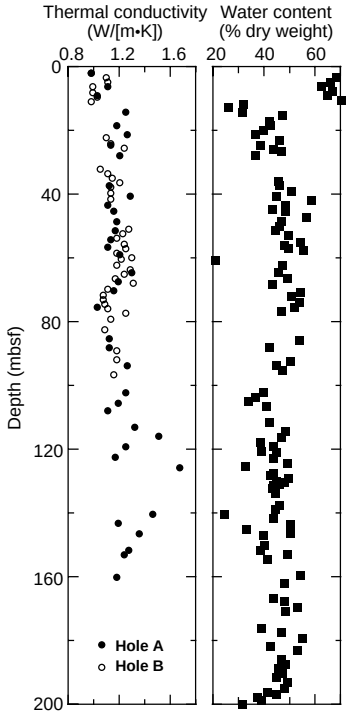

Figure 26. Thermal conductivity and water content for Holes 1003A and 1003B.

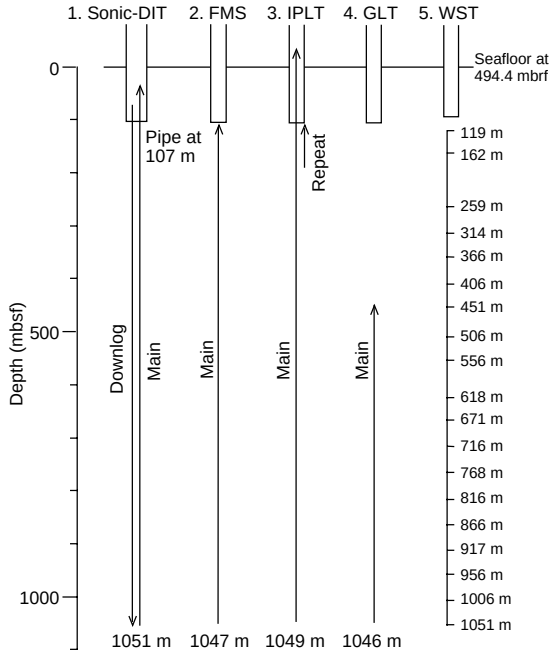

Figure 27. Summary of the logging runs in Hole 1003D. The logging speeds were sonic-DIT at 300 m/hr, FMS at 550 m/hr, IPLT at 350 m/hr, and GLT at 200 m/hr. See "Explanatory Notes" chapter (this volume) for description of the tool strings.

the extreme fluctuations in the values for discrete samples from the lower portion of the section are constrained by wide variability in the logged curves for the same interval.

In general, there is a downhole trend of increasing density, resistivity, and sonic velocity and of decreasing porosity that probably results from sediment compaction (Fig. 28). There is a pronounced change in this trend at 738 mbsf, where the gradient is offset to lower densities, resistivities, and velocities and to higher porosities. This anomalous pattern may be the result of changing sediment composition and diagenetic overprint, and corresponds to the change from sediments with abundant turbidites above (Subunit VA, see "Lithostratigraphy" section, this chapter) to sediments with virtually no turbidites below (Subunit VB). Below 738 mbsf, this major lithologic change is apparent in the natural gamma-ray and geochemical (Ca, Al, and Si) logs (Figs. 29, 30). The increased frequency and magnitude of the uranium signal is particularly notable (Fig. 29). The salinity indicator ratio in the geochemical logs (SIR = Cl/H, Fig. 30) shows a sharp increase below 738 mbsf, implying a more saline formation fluid. These data are consistent with the high chlorinity measured in pore waters from these depths (see "Inorganic Geochemistry" section, this chapter) and demonstrate that the formation above 738 mbsf constitutes a permeability barrier to migrating pore fluids.

Abrupt changes in the downhole trends of physical and chemical properties of the sedimentary succession also occur at 160, 238, 313, 520–537, 645, 738, 897, 915, and 1020 mbsf. The interval between 915 and 1020 mbsf contains a large number of spikes in most of the logs, displaying a markedly different log character than the zones above and below (Fig. 28). This interval is approximately equivalent to seismic Sequence *n* (see "Seismic Stratigraphy" section, this chapter).

The aforementioned changes in downhole trends match closely the depths denoting the boundaries of the lithologic units (e.g., Subunit VB/VIA boundary, Fig. 28) and correlate well with the estimated depths of the sequence stratigraphic boundaries (see "Seismic Stratigraphy" section, this chapter). Although there was incomplete core recovery, the logs will enable refinement of the exact location of both lithologic and sequence boundaries. For instance, the level corresponding to the major biostratigraphic hiatus observed between Cores 166-1003C-47R and 50R (between 897 and 924 mbsf; see "Biostratigraphy" section, this chapter) is well imaged in the FMS data. Within this interval we observe at least three intervals of high-resistivity beds that have a character similar to turbidites observed elsewhere in the cores.

Chemical Changes in the Sedimentary Succession

The GLT tool was deployed in Hole 1003D between 450 and 1050 mbsf (Fig. 30). This interval was chosen because not only were the hole conditions optimal in this interval, but the percent carbonate content (see "Organic Geochemistry" section, this chapter) reveals significant variations in sediment chemistry that could be detected through the logs. In addition, this interval crosses several lithologic units, including a major change in the sedimentary physical properties at 738 mbsf (the transition from Subunit VA to Subunit VB) that had been interpreted as being an effective seal to the vertical migration of gas and fluids. Relative changes in the intensity of the signals of these elements can be compared by taking ratios of the different yields. The processed geochemical data was prepared post cruise and is displayed at the end of this chapter.

Major changes in the concentrations of Ca, Fe, and Al coincide with the transition from Subunit VA to Subunit VB (Figs. 30, 31). Below this boundary, in Subunit VB, the concentration of U inversely correlates with Ca and positively correlates with Al, indicating that U is associated mainly with a clay-rich fraction either in the clay or organic matter (Fig. 31B). Above and below Subunit VB, the cross-correlation analysis suggests that changes in the concentration of U are largely independent of changes in Ca and Al, with perhaps a slight tendency to positive correlation (Fig. 31A). Close examination of the logs indicates that below Subunit VB major U spikes occur together with increased Ca yield, whereas a similar inverse correlation between U and Ca continues to occur at a smaller spatial scale (Figs. 30, 31).

Core-Log Integration and Small-Scale Bedding Patterns

High-quality FMS images obtained at this site will enable a detailed characterization of electric log facies of individual features at the scale of beds and laminae after detailed shore-based work. Together with core descriptions and photographs, the logging data will provide an important complement to characterize the lithology, sedimentary structures, bedding patterns, and physical properties, which cannot be achieved by cores alone because of incomplete recovery. An exact depth match between features observed in the logs and cores is required to understand the log response in the different lithologies. This can be achieved through detailed comparisons of physical properties such as gamma-ray and GRAPE density, which are measured on both core and through wireline tools. Here we illustrate with a few examples the types of features observed in the images and cores and how they relate to one another.

Core 166-1003C-48R contains an example of cyclic bedding observed through much of the Miocene section. Dark, clay-bearing beds with compacted burrows alternate with light-colored, indurated limestone beds containing numerous, usually cemented, uncompacted burrows (Fig. 32; see also "Lithostratigraphy" section, this chapter). Correlation of the gamma-ray logs and MST-NGR data clearly demonstrates that the low-conductivity intervals in the images correspond to the darker colored beds in the cores. This resistivity response is consistent with the porosity contrast in these beds, as well as with increased clay content in the darker beds as revealed by the gamma-ray and chemical logs. High-resolution FMS images, particularly when viewed on a graphic workstation, even display faint features, such as the inferred hardgrounds noted in Core 166-1003-C-48R (Fig. 32).

The expression of turbidite and other coarse-grained deposits recovered at this site can be observed in Figure 33, a comparison of FMS and natural gamma logs with Core 166-1003C-30R. The log response in these thin-bedded deposits in Figure 33 is complex, but it is apparent that intervals interpreted as graded turbidites are resistive at the base and conductive at the top (darkening upward in the FMS image). These turbidites form the base of lithologic Subunit VA, and the Subunit VA/VB boundary at 738 mbsf is obvious in all logs. In the FMS logs, this boundary separates thin (a few tens of centimeters or less) alternations of highly resistive and conductive beds above from longer wavelength and more gentle resistivity contrasts within the cyclic unit below. The gamma-ray log and the core gamma-ray data constrain the core-FMS correlation and suggest that the boundary between Subunits VA and VB probably was recovered near the base of Core 30R. On the basis of interpolated biostratigraphic ages, the contact observed in the FMS images at 738 mbsf would occur at approximately 12.5 Ma and corresponds to sequence Boundary L (see "Seismic Stratigraphy" section, this chapter).

The value of core-log integration in understanding the nature and patterns within the sedimentary succession is further exemplified through images obtained in intervals of poor core recovery. Figure 34 displays a succession that shows an apparently cyclic alternation of resistive and conductive beds representative of compacted/noncompacted intervals. Changes in resistivity show that this cyclic pattern is typically marked by gradual change at bed contacts. In places the cycles appear more asymmetric, with a relatively sharp top contact (e.g., near the top and base of Fig. 34). Whether these intervals represent hardgrounds (e.g., Fig. 32) is difficult to determine from the images alone, but they clearly mark abrupt changes in sedimentation patterns and/or diagenetic alteration.

Intervals recognized in the cores as turbidites and sediment gravity-flow deposits can be distinguished in the images by particularly well-preserved laminations and overall high resistivity. This signature is usually accompanied by peaks in sonic velocity, density, and

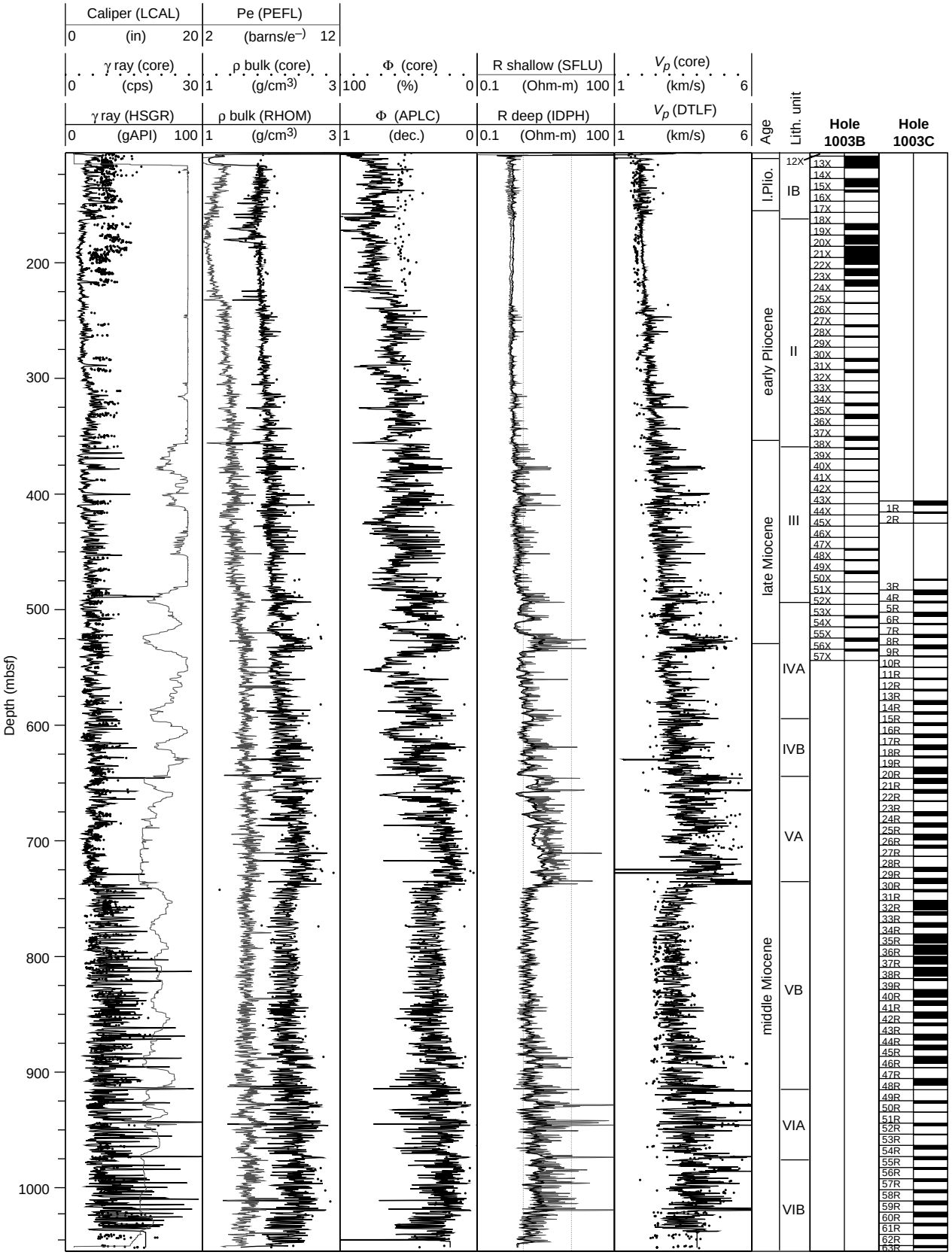

Figure 28. Summary of key geophysical logs acquired with the IPLT and induction-sonic logging strings. From left to right, columns are gamma ray and caliper, bulk density (ρ bulk) and photoelectric index (Pe), porosity (ϕ), shallow and deep resistivity (R), and sonic velocity (V_p). The points represent core measurements from the MST (natural gamma ray) and index properties (bulk density, porosity, and velocity from the DSV instrument; see "Physical Properties" section, this chapter), age, lithologic units, and core recovery in Holes 1003B and 1003C.

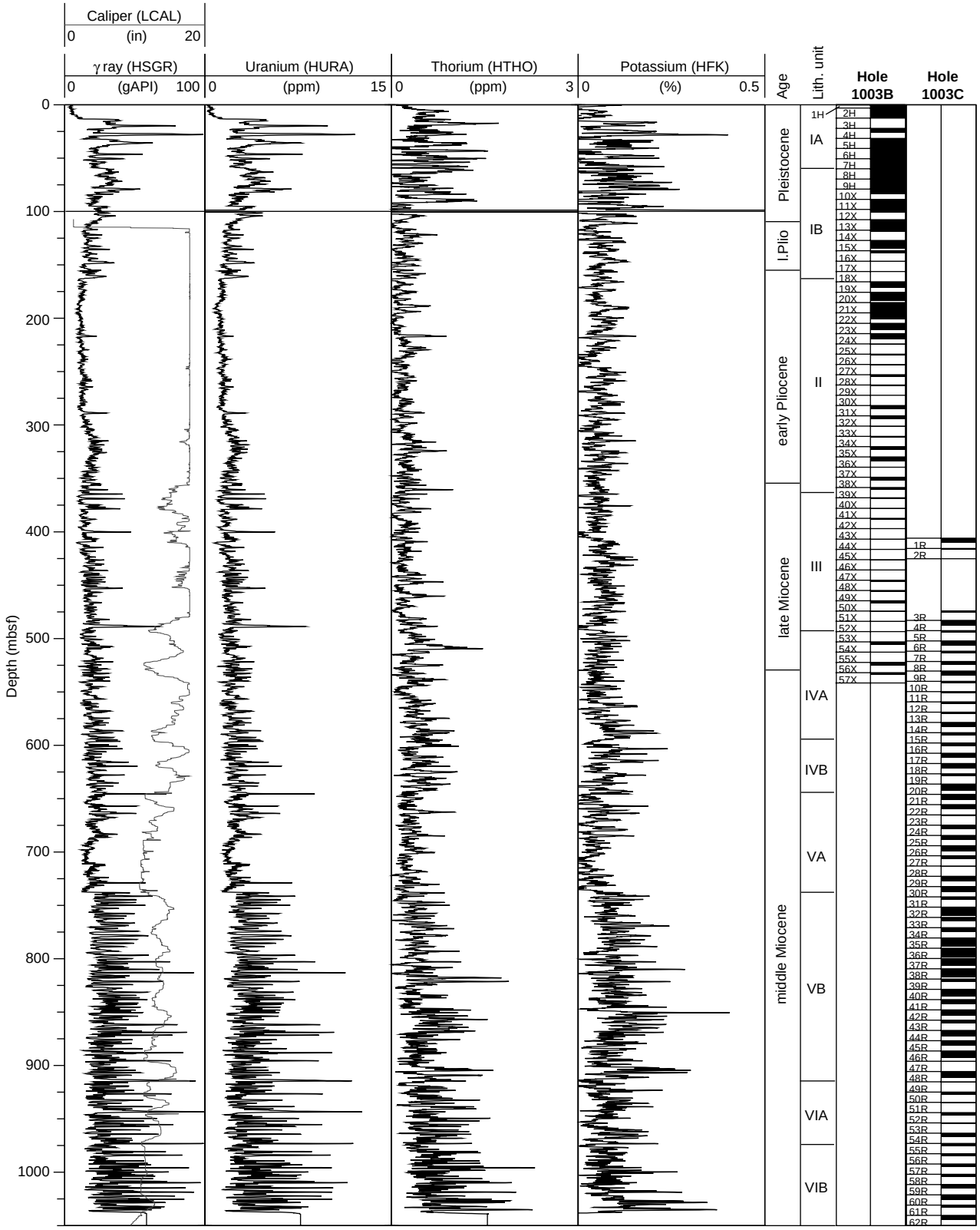

Figure 29. Spectral gamma-ray results from the HNGS tool. The curves between 0 and 105 mbsf were corrected for the attenuation of the gamma-ray spectra caused by measurement in the drill pipe following empirical correction constants obtained by comparing logging runs in Holes 1005A and 1005C (correction factor = 4.0 within the BHA, 1.8 within 5½-in drill pipe, and 1.7 within 5-in drill pipe).

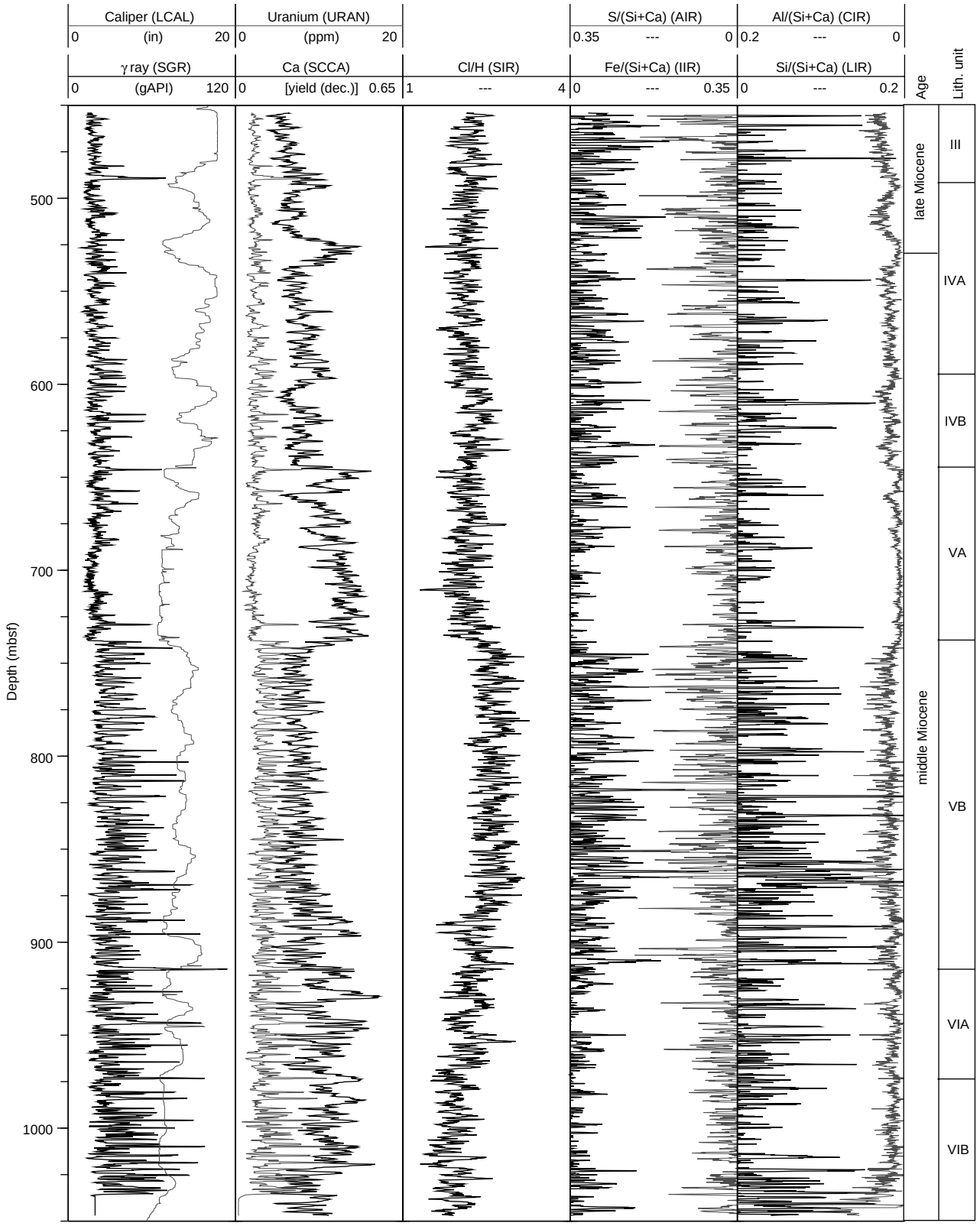

Figure 30. Summary of geochemical logging data. From left to right, columns represent gamma ray (SGR) and caliper (LCAL), uranium (URAN) and calcium yields (SCCA), salinity-indicator ratio (SIR), anhydrite-indicator ratio (AIR) and iron-indicator ratio (IIR), and clay-indicator ratio (CIR) and lithology-indicator ratio (LIR).

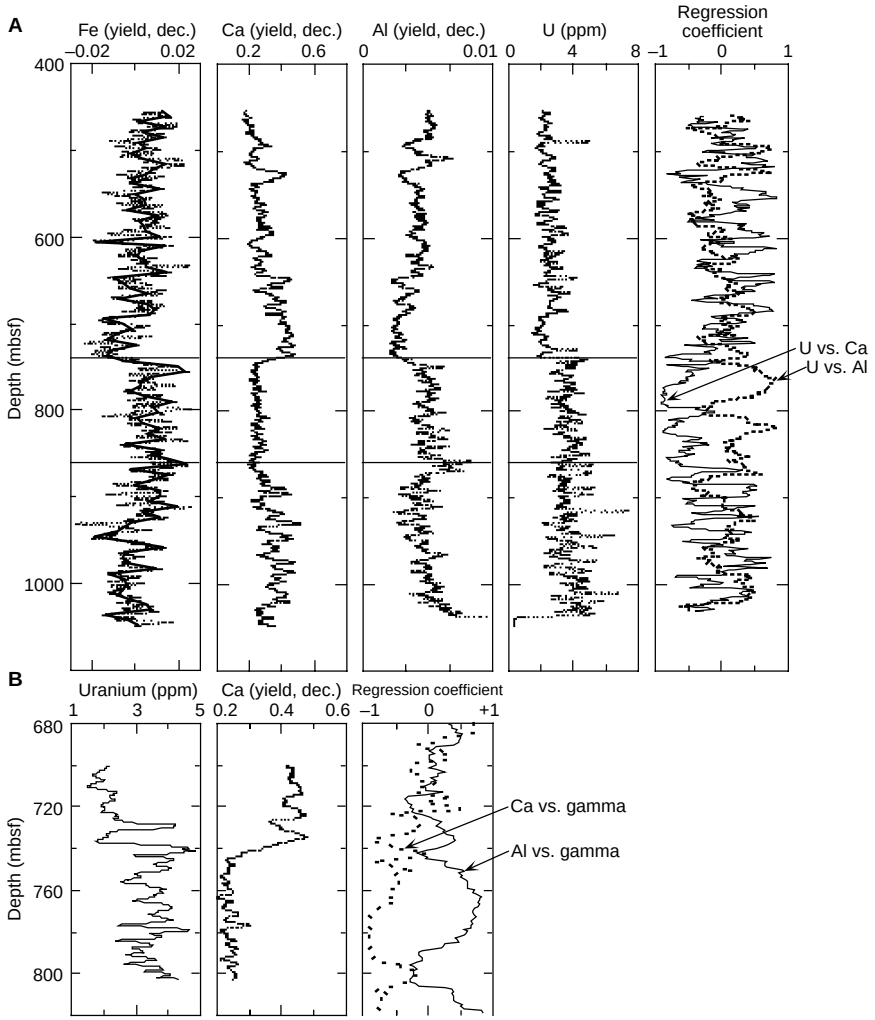

Figure 31. **A.** Sedimentary cycles within the Miocene revealed by geochemical logging data. Points represent raw yields and lines represent 10-point averages. The far-right column represents the cross-correlation coefficient between the different smoothed curves. Note the marked inverse correlation between Ca and U and the positive correlation between U and Al representing limestone beds alternating with clay-bearing, organic rich beds. **B.** Detail of chemical cycles near the boundary between lithologic Subunits VA and VB. A correlation coefficient of R = 1 indicates perfect correlation, R = 0 indicates no correlation, and R = –1 indicates perfect inverse correlation. (yield, dec.) = yield, decimal fraction.

porosity (Fig. 28). In Figure 35, several examples of what appear to be turbidites display thinly laminated beds as well as darkening-upward (fining-upward?) and lightening-upward (coarsening-upward?) beds. The gamma-ray activity in these intervals is higher in the conductive clay beds, and even relatively thin beds cause a slight deflection of the gamma curve.

IN SITU TEMPERATURE MEASUREMENTS

Introduction

Three sets of Adara tools were deployed a total of seven times at Site 1003. Four of these deployments yielded acceptable temperature records. Instrumentation problems caused loss of data for Cores 166-1003A-8H and 1003B-5H. In Core 1003A-5H, the probe penetrated well before it was thermally equilibrated with the bottom water at the mudline, and therefore the data were not useful for obtaining the in situ bottom sediment temperature. Two downhole water sampler, temperature, and pressure probes (WSTP) were deployed a total of five times at Site 1003. The first WSTP yielded somewhat erratic temperature records on the first two deployments, whereas the second deployment for the last three measurements produced high quality data. Table 17 shows the equilibrium temperatures determined for the individual deployments. The error estimates provided in the table are based on a number of fits to the penetration decay curves using the different time ranges. Further work may improve these estimates. The temperature at the seafloor (15.3°C) has been determined from the mudline stops and a nearby expendable bathythermograph (XBT) drop from the ship.

Geothermal Profile

At Site 1003, the geothermal profile is concave upward from the seafloor to about 100 mbsf and then becomes concave downward downhole (Fig. 36). If the geothermal field is in steady state and the heat is transported by conduction, the temperature-depth profile should be linear. The nonlinear profile at this site indicates occurrences of some transient thermal phenomena (e.g., temporary fluctuation of the bottom water temperature) and/or convective heat transfer by pore fluid migration. The pore fluid chemistry studies at this site seem to support the latter mechanism.

Two measurements deviate from this profile (Fig. 36). The temperatures are similar to what would be expected for the temperatures of drill water at these depths (see the “Downhole Measurements” section, this chapter) and therefore, we believe that these measurements were made in the bottom infill of the hole. Examination of the penetration temperature records indicates some anomaly of the deployments. Normally, a successful penetration of the probe into the bottom hole formation observes an instantaneous rise of temperature as a result of the frictional heating of the penetration, which is followed by a gradual, exponential decrease in association with the dissipation of the heat (Fig. 37). At Core 19X, however, little frictional heating occurred at the penetration (Fig. 38). In addition, the probe probably moved during the penetration, indicating that the bottom hole sedi-

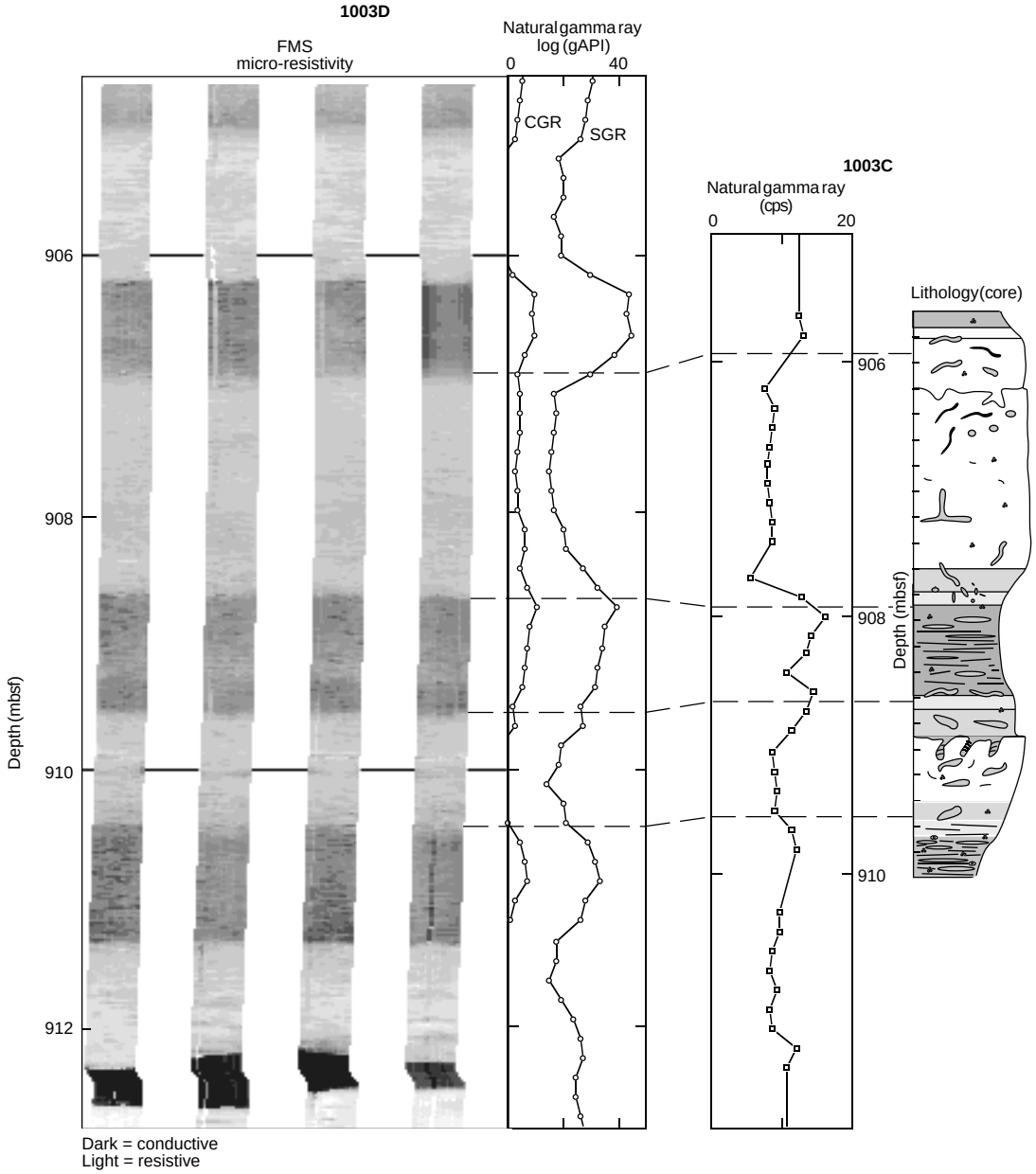

Figure 32. Comparison of a schematic drawing of a sedimentary cycle as seen in a portion of Core 166-1003C-48R with the corresponding FMS image. Conductive (dark) intervals in the image represent dark, clay-bearing intervals with compacted burrows in the core. Resistive (light) intervals in the image represent more cemented limestone with open burrows. Note the relatively sharp contacts between beds in the images that suggest fairly abrupt changes in cementation characteristics. Irregular surfaces toward the top of the light limestone intervals are firmgrounds (see "Lithostratigraphy" section, this chapter).

ments were not very firm. The cores taken at these depths also showed poor recovery rates.

The temperature record from Core 22X (Fig. 39) also is somewhat anomalous, though the equilibrium temperature obtained is considerably higher than the drill water. The thermal decay after the penetration seems too fast in the first minute. This may indicate that the bottom hole sediments were excessively disturbed by the penetration and allowed infiltration of drill water.

Heat Flow

There are two possible solutions for calculating the heat flow at Site 1003. The first is to determine the geothermal gradient using the top seven points of the profile. The second solution uses the top five points and the lowest point only. Either set of points can be reasonably fitted with the linear least square regression (Fig. 36). The first solution gives a geothermal gradient of 34.0°C/km. The second gives a geothermal gradient of 25.1°C/km. The average of the thermal conductivities measured from 0 through 160 mbsf at Site 1003 is 1.17 W/(m·K). Using the average conductivity and the first solution for the geothermal gradient yields a heat flow of 39.8 mW/m^2 compared to 29.4 mW/m^2 from the second solution. The first solution is probably correct because of the relatively questionable quality of the deepest WSTP measurement. Also, the first solution is more consistent with the heat flow values reported from sedimentary basins and slopes of other Mesozoic continental margins in the mid-Atlantic (about 40 mW/m^2; Nagihara et al., 1996; Paull, Matsumoto, Wallace, et al., 1996).

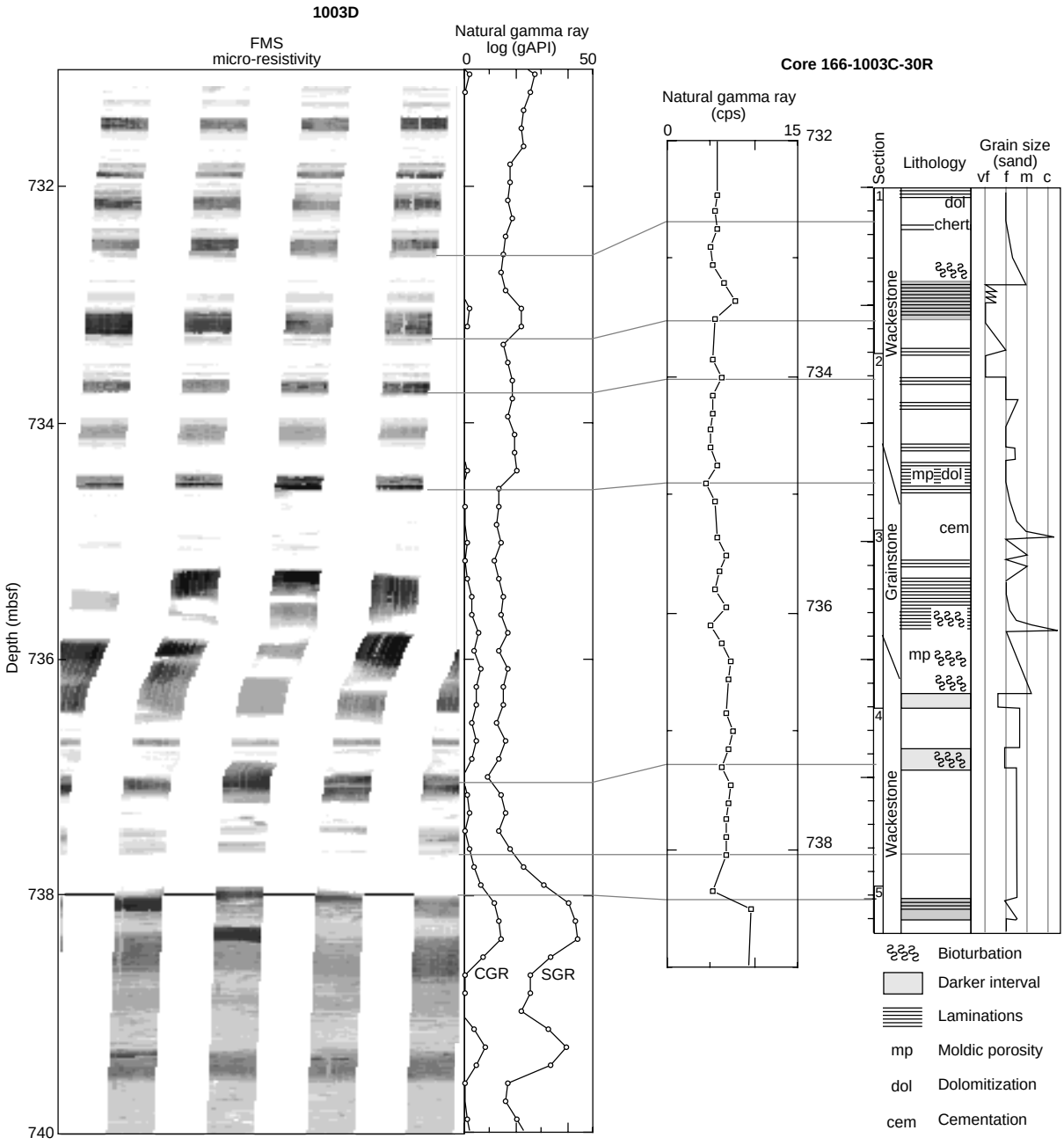

Figure 33. FMS-lithology comparison in an interval of turbidites, suggesting the existence of a hiatus within the middle Miocene at 738 mbsf. The turbidites are highly resistive (white), probably as a result of compaction and/or cementation. Patterns of fining-upward grain size within turbidite beds are represented in the images by a stepwise upward decrease in resistivity (darkening upward). The opposite occurs for coarsening-upward beds.

SEISMIC STRATIGRAPHY

Introduction

Seismic stratigraphic studies of the Neogene section along the Bahamas Transect is mainly based on two seismic data sets and the core borings Unda and Clino on the modern Great Bahama Bank (GBB). A crossbank seismic line (Western Geophysical seismic line) connects the shallow-water environment of GBB with a grid of high-resolution multichannel seismic (MCS) lines in the adjacent Straits of Florida (see Fig. 1). These high-resolution MCS lines were collected aboard *Lone Star* (Rice University) in 1994 (see "Underway Geophysics" chapter, this volume). Predrilling age assignments in these lines were made based on several data sets. Schlager, et al. (1988) correlated biostratigraphic ages from the well Great Isaac-1 on northwestern GBB to a seismic grid located on the banktop north of the Western Line. These ages were originally brought into the seismic grid by jump correlation (Eberli and Ginsburg, 1989). More recently, a set of regional industrial seismic lines became available, which allowed for tracing ages along seismic reflection horizons into the Bahamas Transect area. These ages, in conjunction with the existing ages from older regional lines (Sheridan et al., 1981; Ladd and Sheridan, 1987), provide the regional framework for the seismic stratigraphic interpretation. The two core borings Unda and Clino drilled

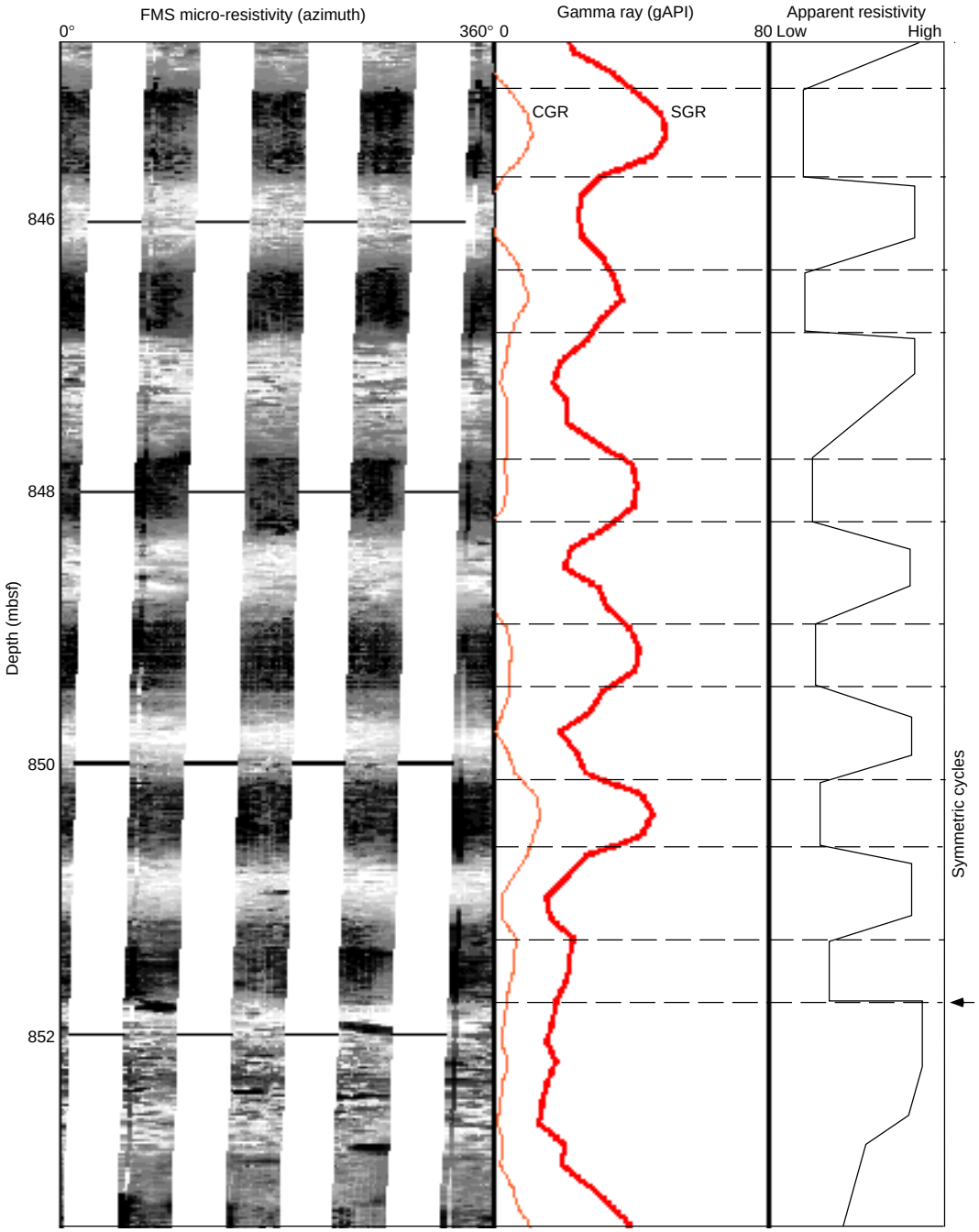

Figure 34. FMS images illustrating the nature of downhole variations in bedding patterns and schematic trends in microresistivi ty. The alternating beds of high and low resistivity show mostly gradational bed boundaries. Both conductive (dark) and resistive (light) beds have burrows, but conductive intervals display faint laminations and flattened burrows, whereas resistive beds tend to display high-resistivity mottling patterns that probably represent cemented burrows (see "Lithostratigraphy" section, this chapter). Note the slight asymmetry of the resistivity pattern toward the top and bottom of the image and the sharp top boundary within the lowermost bed (arrow). The image spans the interval penetrated by Cores 166-1003C-41R and 42R.

in 1990 during the Bahamas Drilling Project on the western margin of GBB penetrated eight sequences of late Miocene to Holocene age (Eberli et al., in press). An integrated chronostratigraphy yielded more precise ages for these sequence boundaries and information about the facies in the prograding sequences (Eberli et al., this volume).

During Leg 166, biostratigraphic age-depth plots were constructed for each site (see "Biostratigraphy" section, "Explanatory Notes" chapter, this volume). Preliminary ages are assigned to the seismic sequence boundaries using the age-depth plots. These ages are tentative, because the tie points were subjectively chosen. Shore-based biostratigraphic research will refine the age models to improve the age assignments of the sequence boundaries. Thus our ages are a first approximation and should be taken with caution.

Seismic sequence boundaries (SSB) were determined on the Western Line, where geometrical relationships, such as erosional unconformities and onlap patterns, help to separate the individual sequences. These SSBs were carried from the Western Line into the

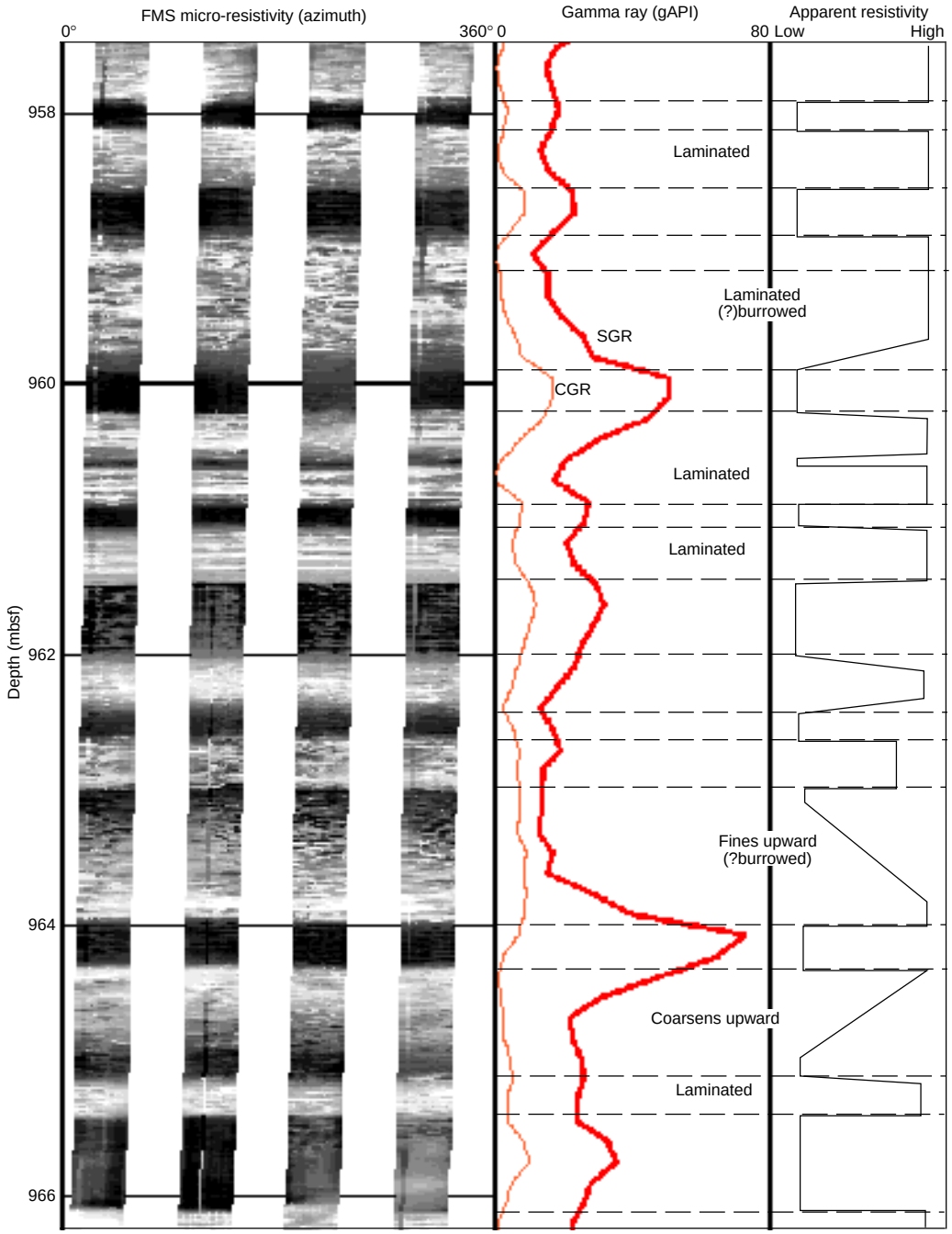

Figure 35. Examples of asymmetric resistivity patterns interpreted as sediment gravity flows. Note the relatively good preservation of parallel laminations with highly compacted burrows. Some beds display no apparent resistivity trends, with a relatively sharp transition to low-resistivity beds above and below. The image spans the interval of low recovery represented by Cores 166-1003C-53R and 54R.

high-resolution MCS lines in the Straits of Florida. For an optimal correlation, we retraced the basinal portion of the Western Line during the acquisition of the high-resolution MCS line (Line 106a). Tracing the reflection horizons is straightforward for the Pleistocene and the early and middle Miocene sequences. Uncertainties exist for the late Miocene and early Pliocene sequence boundaries because the multiple reflections and diffractions generated by the steep GBB margin could not be completely removed in both data sets and, consequently, some of the downlapping and erosional geometries of this time period are partially masked. We identified 17 sequences in the Neogene section, which we labeled *a*–*q*, with their basal SSBs A–Q (see Frontispiece; Figs. 40, 41). At the Leg 166 sites, most of the sequence boundaries are conformable. Minor truncation is observed in the more proximal sites, and two sequence boundaries (D and E) still display major erosional unconformities in the slope section (see Frontispiece and Fig. 40; see "Background and Objectives" section, this chapter). Downlapping geometries within the sequences are common and also help to separate the prograding packages of the individual sequences.

Neogene Platform Evolution

The internal architecture of the individual sequences is partially controlled by the platform/basin morphology, which evolved from a

Table 17. In situ bottom-hole sediment temperatures measured at Site 1003.

Core	Depth (mbsf)	Temperature (°C)	Error (°C)	Mudline (°C)	Tool	Notes
166-1003A-						
4H	35.5	16.25	0.18	15.51	Adara18	
6H	54.5	16.68	0.06	15.73	Adara11	
7H	64.0	16.94	0.04	15.41	Adara18	
166-1003B-						
8H	69.5	17.12	0.05	14.98	Adara11	
166-1003A-						
9H	83.0	16.45	0.70	14.28	Adara18	Anomalous, poor recovery
166-1003B-						
11X	88.5	17.73	0.03	14.91	WSTP204	
166-1003A-						
13X	101.6	18.53	0.01	15.01	WSTP204	Anomalous, poor recovery
16X	139.9	19.63	0.18	14.99	WSTP201	
19X	159.2	18.08	0.01	15.39	WSTP201	Anomalous, poor recovery
22X	188.1	20.06	0.01	16.50	WSTP201	Anomalous

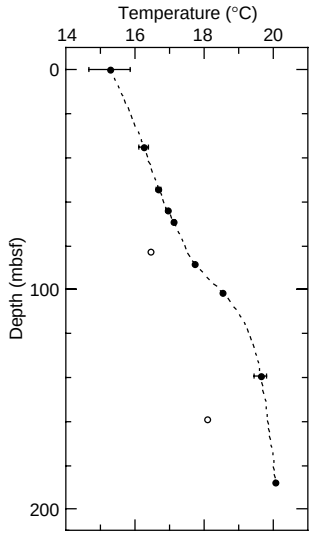

Figure 36. Temperature vs. depth plot for Site 1003. Solid circles represent the reliable temperature measurements and open circles represent the unreliable measurements.

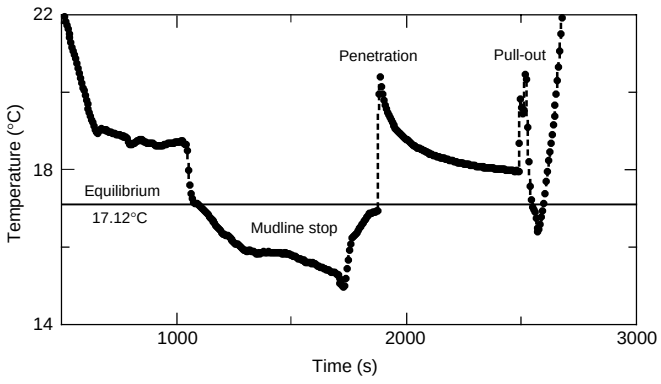

Figure 37. Penetration temperature record from the Adara tool deployment in Core 1003B-8H. The equilibrium temperature calculated from the penetration decay is shown by the horizontal solid line.

low-angle into a steep-sided platform. During the early Miocene, the platform edge was approximately 25 km farther eastward (Fig. 40). The vertically aggrading rimmed platform of this time had a low-angle ramp-like slope to the west. The depositional sequences (*o, p, q*) thus consist of an aggrading portion on the platform and gently dipping and basinward thinning clinoforms. During the middle Miocene (Sequences *k, l, m, n*) the slope angle further decreased, enabling the platform to prograde. A major basinward shift of the margin occurred in the late Miocene that moved the platform edge some 12 km farther westward. Unda penetrated this platform edge, which consisted of a reefal unit in the latest Miocene (Sequence *g*). The reef is bounded by hardgrounds. At Site 1003, the basal hardground forms a hiatus with a maximum of 3 m.y. (8.7–5.7 m.y.) duration. Flooding during the early Pliocene (Sequence *f*) and late Pliocene (Sequence *e*) caused a backstep of the margin and led to renewed platform aggradation. The late Pliocene Sequence *d* again is a prograding unit; its clinoforms are initially thin, but as the sequence moves more basinward it thickens as more current deposits are deposited in the basin axis (Fig. 40). With this progradation event and the prograding pulses of the Pleistocene Sequences *a–c*, the GBB evolved into a steep-sided platform. Each prograding pulse results in a steepening of the frontal clinoforms, so that the current platform margin has a near vertical cliff in the upper 100 m on which the Holocene sediments onlap (Wilber et al., 1990).

In the basinal areas, coeval deposition of a sediment drift occurred from the middle Miocene onward (Frontispiece). These drift deposits form a wide mound-like feature of approximately 800 m in thickness. Toward the east, the drift deposits interfinger with the thin distal tongues of the prograding clinoforms. As a result, Sequences *k–c* thicken again from the toe-of-slope toward the basin. In the late Pliocene and Pleistocene the depocenter of the drift shifted eastward and, as a result, thick packages of drift deposits onlap the slope deposits. Site 1003, however, is positioned in the modern middle-upper slope to penetrate the proximal to distal slope deposits of these Neogene sequences where no influence of the current deposits are recognized in the seismic section (Fig. 41).

Time-Depth Conversion

The prerequisite for a reliable tie between the core and the seismic data is an accurate time-depth conversion. Such a conversion is needed to compare seismic sequence boundaries with lithologic sequence boundaries and to relate lithology to seismic facies. Pre-cruise velocity estimates were derived for the shallow sub-bottom depths from seismic stacking velocities of the site survey data set. At greater depths, where stacking velocities were less reliable, velocities were inferred from expected lithologies and their known properties as measured in the cores Unda and Clino (see Eberli et al., this volume).

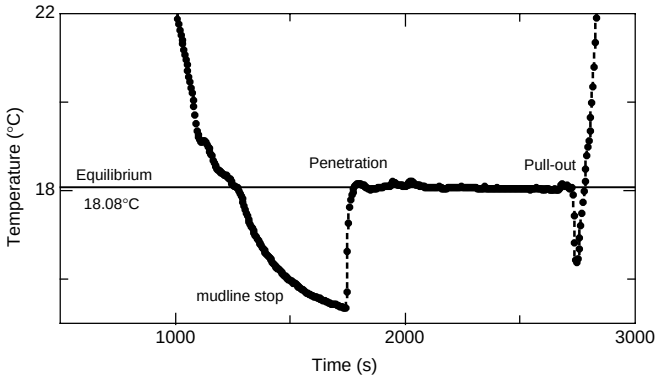

Figure 38. Penetration temperature record from the WSTP deployment in Core 1003A-19X. The equilibrium temperature calculated from the penetration decay is shown by the horizontal solid line. There is little indication of frictional heating at the penetration. The two small pulses at about 2000 s may indicate that the probe moved in the mud and generated some frictional heat.

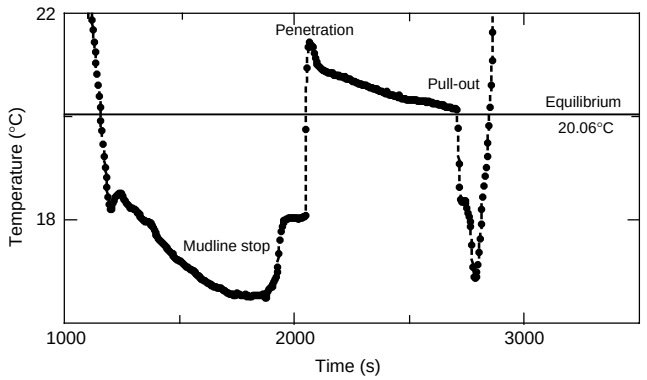

Figure 39. Penetration temperature record from the WSTP deployment in Core 1003A-22X. The equilibrium temperature calculated from the penetration decay is shown by the horizontal solid line. The first minute of the penetration decay seems too steep for conductive dissipation of the frictional heat.

As part of logging operations, a check shot survey was performed using the single channel well seismic tool (WST), which could be lowered to a depth of 1051 mbsf into Hole 1003D (Table 18). The resulting depth traveltime curve with interval velocities between the 19 stations is shown in Figure 42. A preliminary time-depth conversion was also performed using the high-resolution data set of discrete shipboard velocity measurements (n = 1600). This database is used for the time-depth conversion between 1051 and 1300 mbsf where no vertical seismic profile (VSP) data are available (Fig. 42). Differences in seismic formation velocities and shipboard measurements on the core samples were taken into account. Such differences could be caused by selective recovery (hard vs. soft), pressure differences (surface vs. burial), and frequency dispersion (ultrasonic vs. seismic frequencies). The resulting version of a best-fit downhole velocity curve and the resulting time-depth diagram are shown in Figure 42 and compared to the velocities obtained from the VSP. The excellent agreement of this calculated curve with the velocity curve from the VSP gives a high level of confidence for an accurate conversion in the lower part of Site 1003.

Velocity as Indicator of Seismic Facies

The comparison between the shipboard velocity measurements and the sonic log with the seismic data explains the seismic facies on Line 106a and the position of most seismic sequence boundaries. At Site 1003, two major seismic facies can be distinguished (Fig. 41). Sediments above 150 mbsf and between 300 and 750 mbsf are characterized by moderately coherent reflections forming abundant cut-and-fill structures. The high variability in these slope carbonates is reflected in the large range of velocities, particularly in the lower interval. The seismic facies of the zone between 160 and 280 mbsf (between SSBs E and F) are characterized by seismic transparency. The absence of major seismic reflections can be related to the very uniform and low velocities in this interval (Fig. 41). The top of this unit, SSB E, is characterized by irregular, erosive topography and by a velocity increase upcore across the boundary. Both factors accentuate the absence of seismic energy being reflected from the transparent interval. The seismic facies below SSB L is disturbed by the sea-bottom multiple and is difficult to assess. Laterally, where the multiple does not mask the reflection character, the seismic pattern becomes more coherent. A second interval of low seismic reflectivity is found between 740 and 900 mbsf (Sequence *m*), where velocities are much slower and less variable than in the sequences above and below.

In summary, the seismic facies can be explained by the velocity distribution in the various intervals, which in turn can be correlated to variations in lithology. Not surprisingly, therefore, the seismic sequence boundaries match well with the depositional unit boundaries (Fig. 43). Three of these lithologic unit boundaries coincide with hiatuses, and all the others are lithostratigraphically well dated, indicating that the SSBs correlate to the breaks in the pulses of progradation seen in the core.

The Holocene-Pleistocene Sequences

Three Pleistocene seismic sequences were drilled at Site 1003 (*a*–*c*). Their sequence boundaries are indicated on the seismic section by onlap geometries. The youngest sequence (*a*) forms the modern platform edge consisting of a steep margin and an onlapping Holocene wedge with clinoforms thinning basinward. At Site 1003, the seismic reflection marking the base of the sequence is at 10 ms below seafloor (msbsf [TWT]), which translates into 8 m of sediment thickness (Table 19). The sediments within the sequence consist of, in the upper part, unlithified mudstone and wackestone typical for periplatform sediments. The seismic sequence boundary probably coincides with a coarse layer with sand-pebble-sized fossil debris and lithoclasts at 12 mbsf (see “Lithostratigraphy” section, this chapter). This boundary is characterized by an abrupt downward increase in velocity and density (Fig. 23) that results in a distinct impedance contrast across this sequence boundary. This first downcore occurrence of a break in sedimentation, combined with the nannofossil stratigraphy that dates this sequence boundary as 0.09 m.y., indicates that it is likely to be the Pleistocene/Holocene boundary. In the underlying two Pleistocene Sequences *b* and *c*, several horizons of coarse-grained floatstones are intercalated in the periplatform background sediment. Sequence Boundary B is at 30 msbsf (TWT) or 25 mbsf, respectively. This boundary might correlate to the floatstone layer between 27.5 and 28.5 mbsf that is topped by bored lithoclasts that could be the remnant of a thin, hard layer. Sequence *b* is characterized by consistently higher densities and natural gamma values as the sequences above and below (Fig. 23). Sequence *c* is the thickest of the Pleistocene sequences; it extends down to 110 msbsf (TWT) or 100 mbsf, respectively. This depth coincides with the Pliocene/Pleistocene boundary. Lithologically the boundary is expressed by a major packstone layer in Section 166-1003B-12X-2 with convolute and laminar bedding that contains black lithoclasts, foraminifers, bioclasts, and white mud pebbles (see “Lithostratigraphy” section, this chapter). The component assemblage indicates that the debris was shed during platform exposure during sea-level lowstands. Similar layers are also found within the sequences and are interpreted as the record of high-frequency sea level changes within the lower-order seismic sequences.

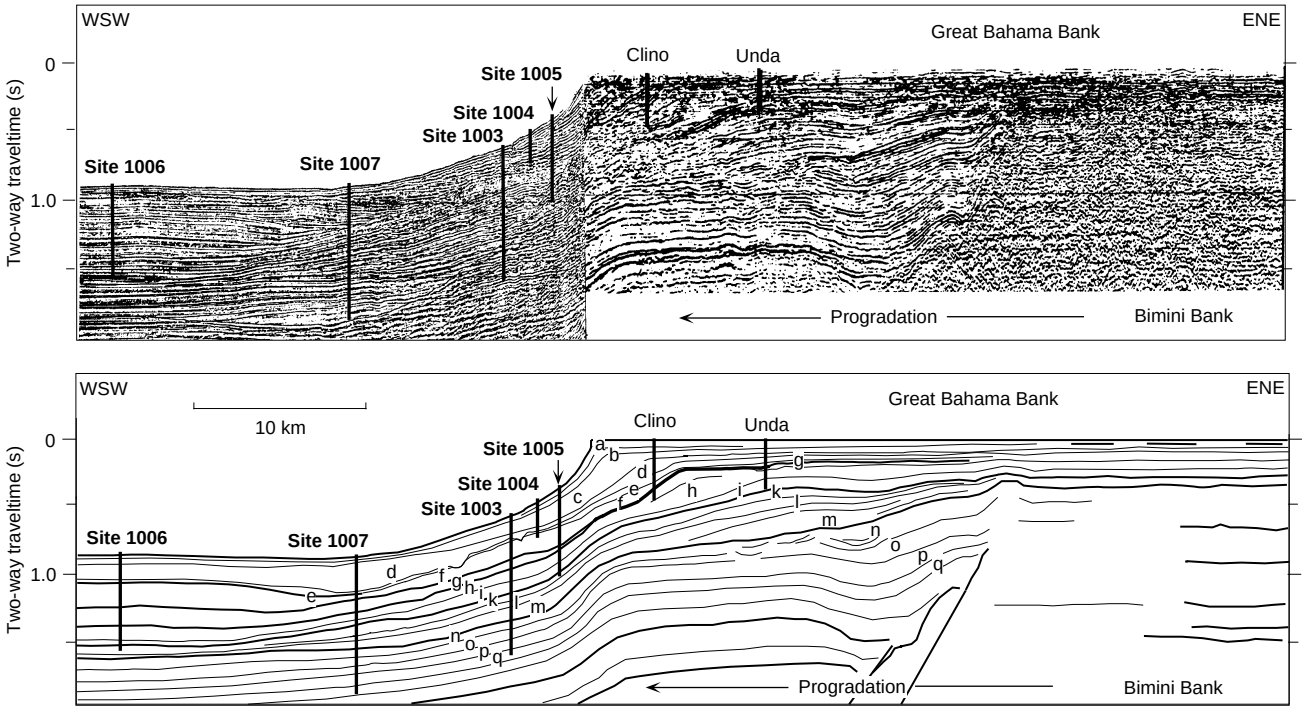

Figure 40. Line drawing of seismic lines across the margin of Great Bahama Bank (Western Line and Line 106a) displaying the upper Cenozoic sequences.

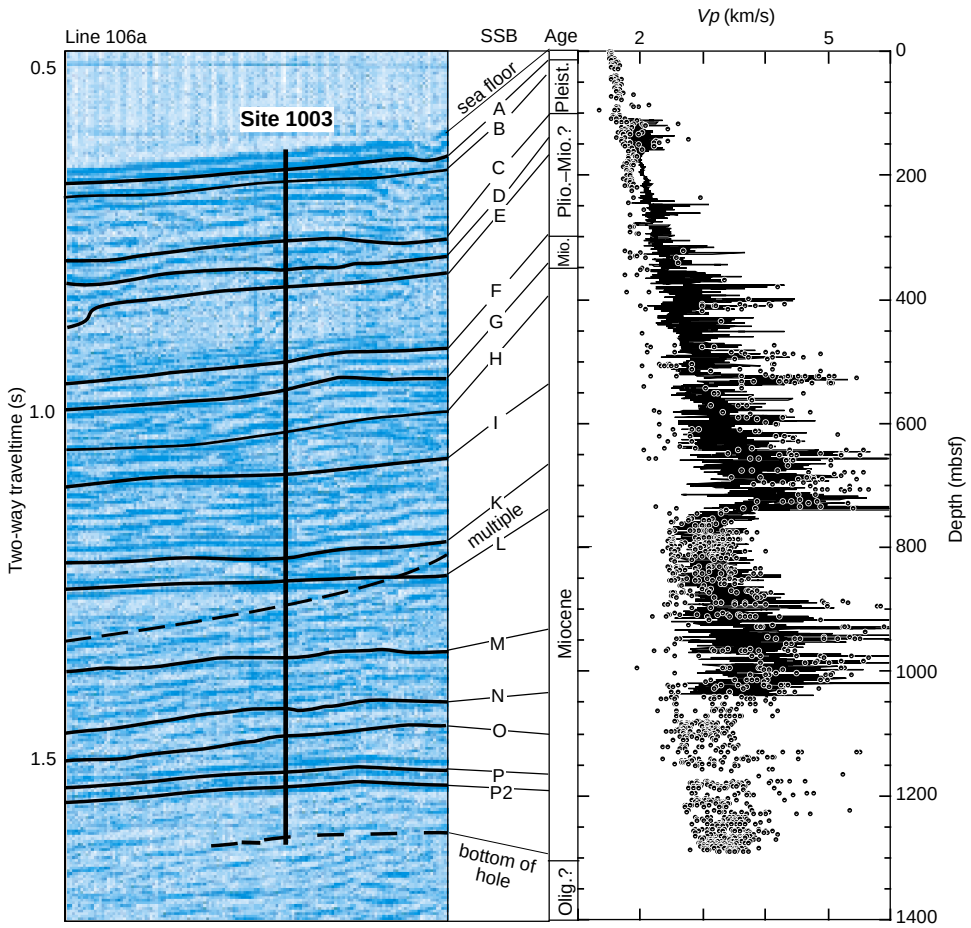

Figure 41. Correlation of seismic Section 106a with traced seismic sequence boundaries (in two-way traveltime) to the ages and physical properties (V_p) at Site 1003.

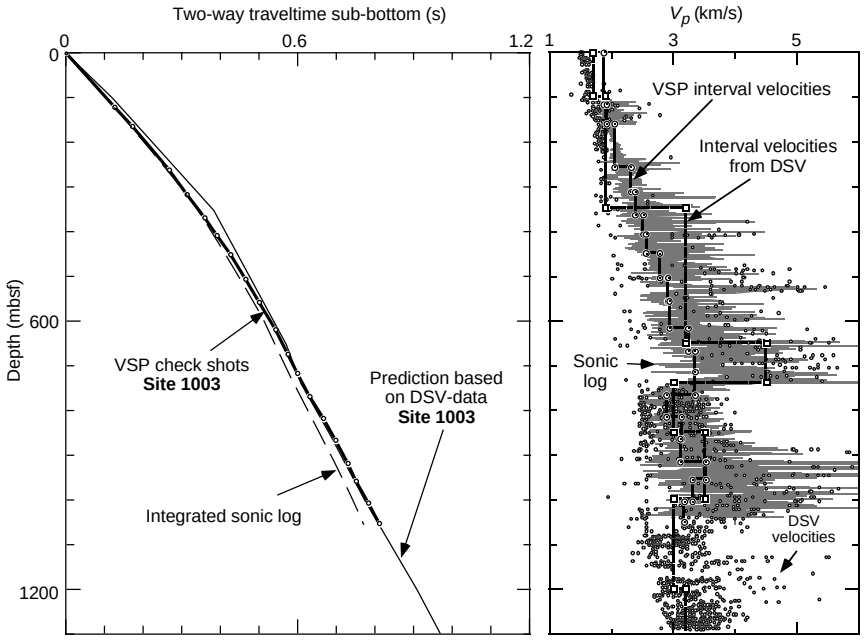

Figure 42. Time-depth conversion according to three different data sources: pre-logging prediction based on shipboard DSV-velocity measurements (thin line); integrated sonic log (far trace); and corrected traveltimes from VSP check shots (solid thick line with circles indicating VSP stations). Resulting interval velocities are plotted on right side.

Table 18. Check-shot stations of VSP survey in Hole 1003D.

Check-shot station	Depth (mbsf)	TWT below seafloor (msbsf)	TWT below sea level (msbsl)
Seafloor	0	0	643.9
166-1003D-			
1	118.5	125.8	769.7
2	161.5	170.4	814.3
3	258.5	264.5	908.4
4	313.5	312.1	956.0
5	365.5	355.9	999.8
6	405.5	387.6	1031.5
7	450.5	422.7	1066.6
8	505.5	462.2	1106.1
9	555.5	496.5	1140.4
10	617.5	538.5	1182.4
11	670.5	571.2	1215.1
12	715.5	598.1	1242.0
13	767.5	629.1	1273.0
14	815.5	662.4	1306.3
15	865.5	694.2	1338.1
16	916.5	726.9	1370.8
17	955.5	748.9	1392.8
18	1005.5	779.1	1423.0
19	1050.5	807.4	1451.3

The Pliocene Sequences

In the shallow core borings Unda and Clino, seismic Sequences *d*, *e*, and *f* were determined to be of Pliocene age (see Eberli et al., this volume). Sequence *d* is confined to the latest Pliocene (1.9–1.7 m.y.). On the slope, SSB D occasionally cuts completely through the underlying Sequence *e*. At Site 1003, SSB D is approximately 30 ms (TWT) above SSB E (Table 19), which is placed at the reflection at 180 msbsf (TWT) or 175 mbsf. This horizon is just below the biostratigraphic boundary between the early and late Pliocene at 159.33 mbsf (see "Biostratigraphy" section, this chapter) and the lithologic boundary between Units I and II at 165.9 mbsf. Considering the seismic resolution and the core recovery, SSB E can possibly be correlated with both and is tentatively dated as 3.8 m.y., which is the time of the onset of extensive Northern Hemisphere glaciation. Just above this boundary peloids start to become part of the component assemblage, indicating a major change of the sediment production on the platform. The sequence boundary is also marked by a change in natural gamma values (Fig. 28): Sequence *e* shows variable gamma ray values with high spikes, whereas Sequence *f* is characterized by low and uniform gamma values.

The early Pliocene Sequence *f* is mostly a transgressive sequence during which the platform margin backstepped for several kilometers. Offbank transport nevertheless was extensive and resulted in a thick package of monotonous wackestones to mudstones (Unit II). The base of Sequence *f* at Site 1003 is at the top of a high-amplitude reflection at 315 msbsf (TWT) or 315 mbsf. No sharp lithologic change occurs across this boundary, but below 320 mbsf the sediments change color from light gray to brownish gray heavily bioturbated wackestones. On the upper slope in bore hole Clino, SSB F is an iron-manganese stained hardground marking a major hiatus that lasted probably from approximately 7.3–4.3 m.y., and straddles the Miocene/Pliocene boundary. On the platform (Hole Unda), the hardground overlays a formerly exposed reef of Messinian age. Sequence *f* is clearly visible on all seismic sections, since it forms a zone with an almost transparent seismic facies. This facies is the result of the homogenous lithology that causes very uniform velocity pattern (Fig. 41). Velocity range increases significantly in Sequence *g* that extends from 315 to 340 msbsf (TWT) or 315 to 350 mbsf, respectively, resulting in higher seismic reflectivity. This interval is not datable due to the poor preservation of the fossils and lack of age-diagnostic species. It is either latest Miocene or earliest Pliocene in age (see "Biostratigraphy" section, this chapter).

The Miocene Sequences

Sequence *g* is either of late Miocene or earliest Pliocene in age. A major hiatus of at least 2.5 m.y. (8. 7–6.2 m.y.) occurs in the cores at approximately 355 mbsf. This hiatus coincides with SSB G at 340 msbsf (TWT) or 350 mbsf. The SSB and the hiatus fall into a mudstone interval with no platform-derived sediment, indicating exposure of platform throughout most of this time. SSB H is at 400 mbsf and roughly correlates with the base of the upper part of lithologic Unit III, which comprises several coarser grained redeposited beds in a wackestone background sedimentation. SSB H is characterized by sharp gamma-peaks as seen on the logs (Fig. 28). Sequence *i* comprises the lower part of Unit III, which is an interval with cyclic alternations of light well-cemented and darker less-cemented wacke-

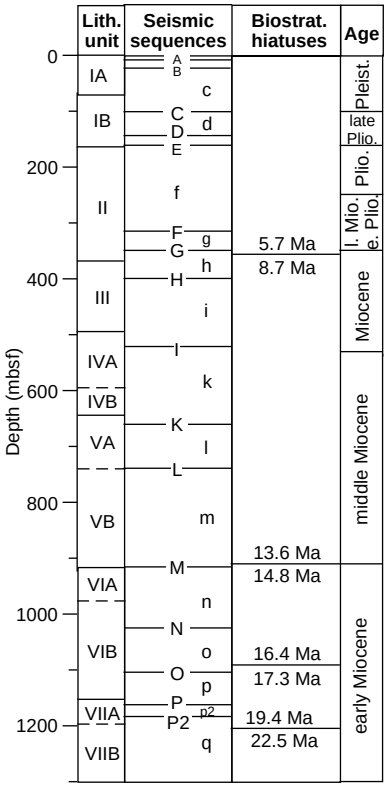

Figure 43. Correlation between lithostratigraphic units, seismic sequences, and biostratigraphic hiatuses and ages.

stones to mudstones. Sequence Boundary I is at 520 mbsf (475 msbsf, TWT) and correlates well with an interval of coarse-grained bioclastic redeposits between 530 and 520 mbsf, which is marked in the sonic log by a prominent positive deviation with V_p of up to 5 km/s. Biostratigraphically determined sedimentation rates indicate low rates of 5 cm/k.y. at the base of the sequence and high sedimentation rates of 15 cm/k.y. in the upper part of the sequence. The increase of sedimentation rate is a result of a higher input of platform-derived material during a time when the platform was flooded.

Four depositional sequences are found within the middle Miocene strata. The first, Sequence *k*, comprises nearly the entire lithologic Unit IV, which contains a packstone-dominated upper part with several calcareous turbidites and a lower part with cyclic alternation of mudstones and wackestones. SSB K is placed at 670 mbsf and dated as 12.2 m.y. This horizon is correlated to a horizon with chertified layers that separate a 30-m-thick interval with turbidites from bioclastic-rich turbidites in lithologic Unit V. The top of this sequence is marked by two high-velocity intervals between 540 and 500 mbsf, which result in the strong and coherent reflection that characterizes SSB I (Fig. 41). The underlying Sequence *l* is characterized by consistently high velocities that contrast to the highly variable velocities in Sequence *k* above and particularly to the low velocities in Sequence *m* below. Sequence *l* extends from SSB K down to 740 mbsf or 610 msbsf (TWT). This depth coincides with the base of lithologic Subunit VA, a subunit with abundant redeposited beds. Biostratigraphically SSB L is dated as 12.7 m.y. Sequences *m* and *n* are of Langhian age. The younger Sequence *m* is the thickest of the middle Miocene sequences at Site 1003. Its upper boundary at 740 mbsf (SSB L) forms a major change not only in lithology, but also in physical and geochemical properties. The velocity pattern displays a dramatic decrease across SSB L (Fig. 42), which is accompanied by sharp changes in density, porosity, and resistivity (Fig. 28). Similar to Sequence *f*, this pattern yields a low seismic reflectivity. In addition, the natural gamma-ray pattern within Sequence *m* shows a high-frequency cyclicity with sharp, high peaks and low background levels, compared to a more uniform pattern with few lower peaks in the sequences above. Its basal SSB M is placed on a reflection at 725 msbsf (TWT) or 915 mbsf, which makes this sequence over 300 m thick. The lithologic facies within the sequence are characterized in the lower part by bioturbated mudstones and packstones and in the upper part by the occurrence of turbidite beds. The basal SSB correlates to the base of lithologic Unit V that starts above a hardground at 915.8 mbsf. This hardground marks a biostratigraphic hiatus that lasted at least from 13.6–15.1 m.y. Sequence *n* is also of Langhian age. Its SSB is placed at 790 msbsf (TWT) or 1025 mbsf, which yields an approximate age of 15.9 m.y. (Table 19). This SSB does not correlate with either a specific biostratigraphic boundary or with a distinct lithologic change. It occurs in an interval that is dominated by dark, heavily bioturbated foraminifer wackestones, which indicate reduced platform-derived sedimentation (see "Lithostratigraphy" section, this chapter) and has a much higher velocity range than Sequence *m* above, resulting in a clearly seismically traceable SSB.

Four early Miocene sequences (*o, p, p2, q*) were penetrated at Site 1003. The basal SSB of Sequence *q*, however, was not reached by the total drilling depth (TD) of 1300 mbsf. Sequence *o* (790–840 msbsf [TWT] or 1025–1105 mbsf) is of Burdigalian age and is lithologically characterized by an alternation of light gray, better cemented intervals and darker bioturbated wackestones. These alternations are interpreted to be produced by high-frequency sea-level changes in which platform sediment is exported into a more shaly background sediment during sea-level highstands. Considering the resolution of the seismic data, the basal SSB O probably correlates with biostratigraphic hiatus at 1089 mbsf, which is at least 1 m.y. in duration (16.4–18.2 m.y.). SSB P is placed at 880 msbsf (TWT) or 1165 mbsf. At this depth, about 10 m of extremely dense fine-grained packstones was encountered in an interval of silt-sized turbidites in greenish wackestones within lithologic Subunit VIIA. The age of this boundary is approximately 19.2 m.y. SSB P2 occurs at a depth of 900 msbsf or 1190 mbsf. On seismic Line 106a, both SSBs P and P2 are imaged by two high-amplitude reflections (white troughs, Fig. 41) despite disturbance by multiple reflections. These strong reflection events are likely a result of a sharp increase in velocities from Sequence *p* to *p2* and underlying Sequence *q*, as seen in shipboard velocity measurements below 1130 mbsf (Fig. 41). The base of Sequence *p2* at 1190 mbsf correlates with a hiatus (19.4–22.5 m.y.) that occurs at 1204 mbsf. The remainder of the core is part of Sequence *q*.

In conclusion, the sedimentary succession at Site 1003 is characterized by variations in the amount of pelagic vs. platform-derived sediments. Punctuations of sediment starvation and erosion are reflected in the seismic sequence architecture. Changes in sediment composition and rates coincide with SSBs, which are interpreted as being controlled by sea-level fluctuations. This indicates that the sequence architecture is also controlled by these changes.

SUMMARY AND CONCLUSIONS

An expanded Neogene section was drilled at Site 1003 on the western slope of GBB. We continuously cored 1300 m and logged 1052 m in a dedicated logging hole. The thick package of sediments provides a chronology for upper middle slope (483 m water depth) deposition from the earliest Miocene to the Holocene. Sufficient recovery (overall more than 40%) and the abundance of biostratigraphic markers, allowed us to accomplish two of the primary sea-level objectives and the fluid-flow objective. It is possible to define the approximate ages of the Neogene sequence boundaries, to test their consistency with ages determined in the boreholes Unda and Clino, and to retrieve the sedimentary record of the middle to lower slope portions of the prograding sequences. Interstitial water chemistry yielded depth profiles with abrupt changes across some stratigraphic

Previous Chapter Table of Contents Next Chapter

Table 19. Time-depth conversion and tentative age assignments of seismic sequence boundaries.

Seismic sequence boundary	TWT below seafloor (msbsf)	Depth (mbsf)	Nannofossil zone	Foraminifer zone	Age	Age* (Ma)
A	10	8	NN21	N23	Holocene/Pleistocene	0.09
B	30	25	NN20	N22	Pleistocene	0.25
C	110	100	NN19	N22	earliest Pleistocene	1.2–1.6
D	150	145	NN16	N21	late Pliocene	3.1
E	180	175	NN14–15	N19/20	early/late Pliocene	3.8
F	315	315	?		Messinian?	5.6
G	340	350	?	N19–16	top Tortonian	8.7–6.2
H	380	400	?	N16	Tortonian	9
I	475	520	NN9	N16	Tortonian	10.6
K	570	670	NN7	N12	Seravallian	12.2
L	610	740	NN7	N12	Seravallian	12.7
M	725	915	NN5	Hiatus	Langhian	13.6–15.1
N	790	1025	NN5	N8	Langhian	15.9
		1089	hiatus	Hiatus		16.4–18.2
O	840	1105	NN4/3	N6	Burdigalian	18.4
P	880	1165	NN3/2	N5	Burdigalian	19.2
P2	900	1190	Hiatus	Hiatus		19.4–22.5
Q	Below TD					

Note: * = ages are preliminary and based on shipboard biostratigraphy (see “Biostratigraphy” section, “Explanatory Notes” chapter, this volume).

boundaries. These data, in conjunction with the temperature profiles, suggest active fluid movement in certain regions of the section.

Depositional Environment and Platform Architecture

During the Neogene, the GBB developed from a platform with a low-angle slope into a steep-sided platform (Reijmer et al., 1992) and prograded more than 25 km into the Straits of Florida, toward Site 1003 (Eberli and Ginsburg, 1989). This evolution of platform morphology is reflected in the sedimentary succession with an increase of platform-derived material from the Miocene to the Pleistocene and in the change from low-diversity, sparse, transported shallow-water taxa in the Pliocene to common, transported shallow-water benthic foraminifers in the Pleistocene. The prograding clinoforms are punctuated by intervals with increased pelagic deposits indicating that sediment production and export from the bank was variable through time. Miocene units are characterized by alternations of darker, lower, carbonate layers and whiter, carbonate-rich layers. Miocene units also have variable amounts of intercalated packstones and floatstones with abundant neritic components that are interpreted as turbidites and other mass gravity flow deposits. In these Miocene sections, a small amount of fine-grained siliciclastics are admixed in the pelagic intervals. The frequency and average thickness of the coarser intercalations increase from the earliest Miocene to the late Miocene, documenting the platform progradation. This trend continues in the Pliocene and culminates in the Pleistocene strata with the deposition of thick periplatform units with frequent intercalations of mass gravity flow deposits. These strata consist of a series of mixed pelagic and bank-derived carbonates, with a carbonate content of 92%–97%.

Sedimentary Record of Sea-Level Changes

The variations in the amount of platform-derived sediments vs. pelagic sedimentation are interpreted to be related to sea-level changes. Platform-derived sedimentation is indicative for sea-level highstands, whereas the more pelagic intervals are reflecting times of platform exposure or backstepping. These lithologic variations correlate with the seismic sequence architecture that was previously established from the seismic data. Foraminifer and nannofossil biostratigraphy yielded precise ages of the lithologic units and the sequence boundaries (see “Seismic Stratigraphy” section, this chapter).

The sediments contained in Unit I (0–162.07 mbsf) are of Pleistocene to latest Pliocene in age, a climate period characterized by intensive Northern Hemisphere glaciation. The unit consists of unlithified to partially lithified mudstones, wackestones, packstones, and floatstones. The onset of the modern platform production is documented by a high sedimentation rate during the last 0.9–1.0 Ma (10 cm/k.y.). The lower Pleistocene–upper Pliocene interval shows a much slower sedimentation rate of about 2.5 cm/k.y. This low rate during the early Pleistocene is consistent with lower rates measured on other shallow Bahamian platforms (McNeill et al., 1988). The early Pleistocene on many Bahamian platforms was a period of relative lowstand and subaerial exposure (Beach and Ginsburg, 1980; Williams, 1985; McNeill et al., 1988). The middle to late Pleistocene increase in sedimentation rate is related to intermittent, high-amplitude sea-level flooding events. Three seismic sequences are distinguished within the Quaternary. Their SSBs coincide with coarse and hardened layers of packstones and floatstones within the periplatform ooze. Blackened lithoclasts from the platform top in these layers indicate erosion during platform exposure and sea-level lowstands. The youngest SSB (A) is dated as 0.09 Ma and is probably the Holocene/Pleistocene boundary. SSB B is placed at 25 mbsf and is dated as 0.25 Ma. The oldest Pleistocene, SSB C, is dated as 1.2–1.6 Ma and probably represents the Pleistocene/Pliocene boundary.

In the late Pliocene, sedimentation rate drops to 2.5 cm/k.y. at Site 1003. A low rate of sedimentation during the Pliocene was also reported at the sites of Leg 101 and was attributed to periods of sea-level lowering and a decrease of bank-top-derived sediments (Mellilo, 1988; Watkins and Verbeek, 1988). This reduced sedimentation rate is also reflected in the thicknesses of the two upper Pliocene Sequences *d* and *e*, which at Site 1003 are only 45 m and 30 m thick, respectively. SSB D is dated as 3.1 Ma and SSB E as 3.8 Ma. The onset of this reduced sedimentation and the age of SSB E coincide with the timing of the onset of extensive Northern Hemisphere glaciation.

The lower Pliocene–upper Miocene sediments consist of a homogeneous section of partially lithified, intensely bioturbated wackestones with variations in the composition and abundance of skeletal fragments (lithologic Unit II [166–359.92 mbsf]). The base of this unit is a nannofossil chalk. The lack of peloids in the off-bank transported sediment in this time interval documents a change in the sediment production on the platform from peloidal to skeletal material. This change is also observed in core borings from the top of the GBB (Beach and Ginsburg, 1980). In regard to sea level this unit is interpreted to record an initial flooding in the Zanclian followed by a prolonged interval of high sea levels with extensive sediment production and off-bank transport on the bank. Intermittent high-frequency, sea-level falls are indicated by periodic admixtures of silt-sized blackened bioclasts and lithoclasts in the periplatform sediments. Two seismic sequences are identified within this unit. Sequence *e* is 140 m thick and for the most part is early Pliocene in age. Its basal se-

quence boundary could not be dated as a result of the absence of age-diagnostic fossils. It is either early Pliocene or late Miocene in age (see "Biostratigraphy" section, this chapter). Consequently, it is not clear if the underlying Sequence *f* is of Miocene or Pliocene age. The horizon that marks its basal SSB F is a hiatus that lasted at least 2.5 Ma, from 8.7 to 6.2 m.y, and indicates erosion and platform exposure throughout most of this time. Therefore, Sequence *f* could be of Messinian age.

The sediments of Unit III (368.2–493 mbsf) were deposited during Tortonian times. In this unit a pattern of facies successions is observed that is repeated in the underlying Units IV–VII. The top part of this and the following units are dominated by packstones to grainstones that are interpreted as turbidites and other mass gravity flow deposits in a background sediment of bioturbated wackestones. The bottom part of the units are composed of cyclic alternations of light-gray, lithified packstone to wackestone beds with an average thickness of 30–40 cm and darker, greenish to brownish gray, with less lithified intervals of 15- to 25-cm thickness. The facies succession of the entire unit is seen as the expression of a prograding pulse in which coarser-grained platform-derived sediments are deposited on a lower bathyal slope. The cyclic alternations are interpreted as the record of high-frequency sea-level changes in which the lighter, better cemented intervals reflect higher neritic input with high aragonite content during sea-level highstands and the darker compacted zones reflect a decreased input of aragonite during sea-level lowstands. Unit III roughly coincides with seismic Sequences *h* and *i.* SSB H (9 Ma) correlates with the top of a series of turbidites that are not well recovered, but are clearly visible on the FMS images. In contrast, SSB I (10.6 Ma) underlies a 15-m-thick interval with turbidites, indicating that these were shed during both sea-level highstands and lowstands.

Four seismic sequences are distinguished in the middle Miocene section. The sequence boundaries of the first two Sequences *k* and *l* are of Seravallian age, and the basal SSBs are dated as 12.2 Ma and 12.7 Ma, respectively. Based on the time-depth conversion using the WST, their boundaries are placed in and below intervals with coarser-grained packstones that are interpreted as turbidites. Some of the turbidites carry blackened clasts in their component assemblage that are indicative of erosion during platform exposure. At least parts of the turbidite interval, therefore, were probably deposited during relative sea-level lowstands. The bulk of these sequences, however, shows a distinct cyclicity of light-gray, well-cemented, moderately bioturbated intervals and strongly bioturbated, dark gray to green layers. The thicknesses of the cycles range between 50 and 200 cm. The darker intervals also contain a small amount of clay and silt-sized quartz, plagioclase, and clay. The cycles are interpreted to record high-frequency sea-level changes in the Miocene when platform-derived carbonates produced carbonate-rich beds in more clayey slope sediments.

The Langhian Sequence *m* is the thickest of the middle Miocene and is composed nearly exclusively of the cyclic alternation described above; only in the upper part did we observe some intercalations of packstones and floatstones. A hardground at 915.2 mbsf separates Sequence *m* from the underlying Sequence *n* and lithologic Unit V from the underlying Unit VI. The hardground marks a biostratigraphic hiatus of approximately 1.2 Ma (13.6–14.8 Ma). Obviously, input from the platform top was reduced for a prolonged period of time. Below the hardground, Sequence *n* has intercalations of packstones and floatstones in the upper part with a background sedimentation of bioturbated, greenish-grayish wackestones and packstones. SSB N is placed within lithologic Subunit VIB and dated as 15.9 Ma.

In the lower Miocene, the packstone-dominated intervals within the cyclic sedimentation are thin, and the packstones are thin-bedded. The siliciclastic admixture is now approximately 5%–7%. Thus, the turbidite-bearing intervals in the Miocene show an overall thickening and coarsening upward trend in their packstone dominated subunits, indicating a pulsed, but progressive progradation of GBB throughout the early and middle Miocene. Three early Miocene SSBs are carried from inside the GBB to the slope of Site 1003. SSB O (1105 mbsf) is tentatively dated as 18.4 Ma. The next older SSB, P, is placed at (1165 mbsf) and dated as 19.2 Ma. Lithologically, it is expressed by a well-cemented package within a thin turbidite sequence. Turbidites below the SSB belong to the top of Sequence *q* whose bottom was not reached at TD.

In summary, sedimentation from the lowermost Miocene to the Holocene seems to be controlled by changing sea level. Thick and expanded intervals during the early and middle Miocene coincide with the generally high sea level of this time. The late Miocene, a time of global cooling and sea-level fall, is recorded in a reduced interval and a subsequent hiatus. The Pliocene sea-level rise resulted in renewed flooding of GBB and sedimentation on the slope. As far as the seismic sequence stratigraphy is concerned, the principal result of Site 1003 is that the SSBs, which were defined in the subsurface of GBB, can be carried to the slope where they correlate with stratal surfaces. In addition, the bounding facies indicate that these sequence boundaries were formed during sea-level falls. Furthermore, a nannofossil-planktonic foraminiferal stratigraphy was established at Site 1003, which allows us to tentatively date the SSBs. A comparison with the proposed global sea-level curve of Haq et al., (1987) shows a very good agreement of the age of the SSBs at Site 1003 with the major sea-level fluctuations throughout the Neogene.

Indications for Fluid Flow

The most persuasive evidence for fluid flow is provided by the absence of changes in both conservative and nonconservative pore-water constituents in the upper portion (flushed zone) of Site 1003 (0–40 mbsf). Although temperature profiles obtained using Adara indicate a nonsteady state condition, they do not conclusively support or negate fluid flow in this interval at this site. Below the flushed zone, the concentration of Cl^- rises steadily with increasing depth to the bottom of the hole and concentrations of nonconservative elements (Ca^{2+}, Mg^{2+}, Sr^{2+}, SO_4^{2-}, alkalinity, and NH_4^+) vary in response to different diagenetic reactions occurring locally in the sediments. These reactions include the oxidation of organic material and the recrystallization of aragonite and the precipitation of dolomite and calcite. The deepest interstitial water sample (1083 mbsf) taken from Hole 1003C shows concentrations of Cl^- and other minor elements nearly twice that of normal seawater. These high concentrations cause the lower portion of the geochemical profile to be dominated by diffusion of Cl^-, Ca^{2+}, and K^+ from an underlying brine and by local reactions within the sediments. The source of this high Cl^- is at present not known, but it could result from upward migration of a high-salinity brine from an evaporitic deposit deeper in the Straits of Florida or beneath the Great Bahama Bank itself.

REFERENCES

Baker, P.A., 1986. Pore-water chemistry of carbonate-rich sediments, Lord Howe Rise, Southwest Pacific Ocean. *In* Kennett, J.P., von der Borch, C.C., et al., *Init. Repts. DSDP,* 90: Washington (U.S. Govt. Printing Office), 1249–1256.

Baker, P.A., and Bloomer, S.H., 1988. The origin of celestite in deep-sea carbonate sediments. *Geochim. Cosmochim. Acta,* 52:335–339.

Baker, P.A., Gieskes, J.M., and Elderfield, H., 1982. Diagenesis of carbonates in deep-sea sediments: evidence from Sr^{2+}/Ca^{2+} ratios and interstitial dissolved Sr^{2+} data. *J. Sediment. Petrol.,* 52:71–82.

Beach, D.K., and Ginsburg, R.N., 1980. Facies succession, Plio-Pleistocene carbonates, Northwestern Great Bahama Bank. *AAPG Bull.,* 64:1634–1642.

Claypool, G.E., and Kaplan, I.R., 1974. The origin and distribution of methane in marine sediments. *In* Kaplan, I.R. (Ed.), *Natural Gases in Marine Sediments:* New York (Plenum), 99–139.

Davies, P.J., McKenzie, J.A., Palmer-Julson, A., et al., 1991. *Proc. ODP, Init. Repts.*, 133 (Pts. 1, 2): College Station, TX (Ocean Drilling Program).

De Carlo, E.H., 1992. Geochemistry of pore water and sediments recovered from the Exmouth Plateau. *In* von Rad, U., Haq, B.U., et al., *Proc. ODP, Sci. Results*, 122: College Station, TX (Ocean Drilling Program), 295–308.

Droxler, A.W., and Schlager, W., 1985. Glacial versus interglacial sedimentation rates and turbidite frequency in the Bahamas. *Geology*, 13:799–802.

Eberli, G.P., and Ginsburg, R.N., 1989. Cenozoic progradation of NW Great Bahama Bank: a record of lateral platform growth and sea fluctuations. *In* Crevello, P.D., et al. (Eds.), *Controls on Carbonate Platform and Basin Evolution.* Spec. Publ.—Soc. Econ. Paleontol. Mineral., 44:339–355.

Eberli, G.P., Kenter, J.A.M, McNeill, D.F., Anselmetti, F.S., Melim, L.A., and Ginsburg, R.N., in press. Facies, diagenesis and timing of prograding seismic sequences on western Great Bahama Bank. *Soc. Econ. Paleontol. Mineral. Concepts Sedimentol. Paleontol.*

Emeis, K.-C., and Kvenvolden, K.A., 1986. Shipboard organic geochemistry on *JOIDES Resolution. ODP Tech. Note*, 7.

Gieskes, J.M., 1983. The chemistry of interstitial waters of deep-sea sediments: interpretation of deep-sea drilling data. *In* Riley, J.P., and Chester, R. (Eds.), *Chemical Oceanography* (Vol. 8): London (Academic), 221–269.

Haak, A.B., and Schlager, W., 1989. Compositional variations in calciturbidites due to sea-level fluctuations, Late Quaternary, Bahamas. *Geol. Rundsch.*, 78:477–486.

Handford, C.R., and Loucks, R.G., 1993. Carbonate depositional sequences and systems tracts: responses of carbonate platforms to relative sea-level changes. *In* Loucks, R.G., and Sarg, J.F. (Eds.), *Carbonate Sequence Stratigraphy.* AAPG Mem., 57:3–41.

Haq, B.U., Hardenbol, J., and Vail, P.R., 1987. Chronology of fluctuating sea levels since the Triassic. *Science*, 235:1156–1167.

Katz, M.E., and Miller, K.G., 1993. Latest Oligocene to earliest Pliocene benthic foraminiferal biofacies of the northeastern Gulf of Mexico. *Micropaleontology*, 39:367–403.

Kendall, C.G.St.C., and Schlager, W., 1981. Carbonates and relative changes in sea level. *In* Cita, M.B., and Ryan, W.B.F. (Eds.), *Carbonate Platforms of the Passive-type Continental Margins, Present and Past.* Mar. Geol., 44:181–212.

Kenter, J.A.M., Ginsburg, R.N., and Treolstra, S.R., in press. The western Great BAhama Bank: sea-level-driven sedimentation patterns on the slope and margin. *In* Ginsburg, R.N. (Ed.), *SEPM Contributions in Sedimentology.*

Ladd, J.W., and Sheridan, R.E., 1987. Seismic stratigraphy of the Bahamas. *AAPG Bull.*, 71:719–736.

Lidz, B.H., and McNeill, D.F., 1995. Reworked Paleogene to early Neogene planktonic foraminifers: implications of an intriguing distribution at a late Neogene prograding margin, Bahamas. *Mar. Micropaleontol.*, 25:221–268.

Maher, B.A., 1988. Magnetic properties of some synthetic sub-micron magnetites. *Geophys. J. R. Astron. Soc.*, 94:83–96.

McNeill, D.F., Ginsburg, R.N., Chang, S.-B.R., and Kirschvink, J.L., 1988. Magnetostratigraphic dating of shallow-water carbonates from San Salvador, Bahamas. *Geology*, 16:8–12.

Melillo, A.J., 1988. Neogene planktonic foraminifer biostratigraphy, ODP Leg 101, Bahamas. *In* Austin, J.A., Jr., Schlager, W., et al., *Proc. ODP, Sci. Results*, 101: College Station, TX (Ocean Drilling Program), 3–45.

Mullins, H.T., 1983. Comment on "Eustatic control of turbidites and winnowed turbidites." *Geology*, 11:57–58.

Nagihara, S., Sclater, J.G., Phillips, J.D., Behrens, E.W., Lewis, T., Lawver, L.A., Nakamura, Y., Garcia-Abdeslem, J., and Maxwell, A.E., 1996. Heat flow in the western abyssal plain of the Gulf of Mexico: implications for thermal evolution of the old oceanic lithosphere. *J. Geophys. Res.*, 101:2895–2913.

Paull, C.K., Matsumoto, R., Wallace, P.J., et al., 1996. *Proc. ODP, Init. Repts.*, 164: College Station, TX (Ocean Drilling Program).

Reijmer, J.J.G., Schlager, W., Bosscher, H., Beets, C.J., and McNeill, D.F., 1992. Pliocene/Pleistocene platform facies transition recorded in calciturbidites (Exuma Sound, Bahamas). *Sediment. Geol.*, 78:171–179.

Reymer, J.J.G., Schlager, W., and Droxler, A.W., 1988. Site 632: Pliocene–Pleistocene sedimentation in a Bahamian basin. *In* Austin, J.A., Schlager, W., Palmer, A.A., et al., *Proc. ODP, Sci. Results*, 101: College Station, TX (Ocean Drilling Program), 213–220.

Sarg, J.F., 1988. Carbonate sequence stratigraphy. *In* Wilgus, C.K., Hastings, B.S., Kendall, C.G.St.C., Posamentier, H., Ross, C.A., and Van Wagoner, J. (Eds.), *Sea-Level Changes: An Integrated Approach*. Spec. Publ.—Soc. Econ. Paleontol. Mineral., 42:155–181.

Schlager, W., 1991. Depositional bias and environmental change—important factors in sequence stratigraphy. *Sediment. Geol.*, 70:109–130.

Schlager, W., Bourgeois, F., Mackenzie, G., and Smit, J., 1988. Boreholes at Great Isaac and Site 626 and the history of the Florida Straits. *In* Austin, J.A., Jr., Schlager, W., et al., *Proc. ODP, Sci. Results*, 101: College Station, TX (Ocean Drilling Program), 425–437.

Schlager, W., and James, N.P., 1978. Low-magnesian calcite limestones forming at the deep-sea floor, Tongue of the Ocean, Bahamas. *Sedimentology*, 25:675–702.

Sheridan, R.E., Crosby, J.T., Bryan, G.M., and Stoffa, P.L., 1981. Stratigraphy and structure of southern Blake Plateau, Northern Florida Straits, and Northern Bahama Platform from multichannel seismic reflection data. *AAPG Bull.*, 65:2571–2593.

Shipboard Scientific Party, 1988. Leg 101—an overview. *In* Austin, J.A., Jr., Schlager, W., et al., *Proc. ODP, Sci. Results*, 101: College Station, TX (Ocean Drilling Program), 455–472.

————, 1991. Explanatory notes. *In* Davies, P.J., McKenzie, J.A., Palmer-Julson, A., et al., *Proc. ODP, Init. Repts.*, 133 (Pt. 1): College Station, TX (Ocean Drilling Program), 31–58.

Swart, P.K., and Burns, S.J., 1990. Pore-water chemistry and carbonate diagenesis in sediments from Leg 115: Indian Ocean. *In* Duncan, R.A., Backman, J., Peterson, L.C., et al., *Proc. ODP, Sci. Results*, 115: College Station, TX (Ocean Drilling Program), 629–645.

Swart, P.K., and Guzikowski, M., 1988. Interstitial-water chemistry and diagenesis of periplatform sediments from the Bahamas, ODP Leg 101. *In* Austin, J.A., Jr., Schlager, W., Palmer, A.A., et al., *Proc. ODP, Sci. Results*, 101: College Station, TX (Ocean Drilling Program), 363–380.

Tjalsma, R.C., and Lohmann, G.P., 1983. Paleocene-Eocene bathyal and abyssal benthic foraminifera from the Atlantic Ocean. *Micropaleontol. Spec. Publ.*, 4.

Vail, P.R., Audemard, F., Bowman, S.A., Eisner, P.N., and Perez-Cruz, G., 1991. The stratigraphic signatures of tectonics, eustasy, and sedimentology—an overview. *In* Einsele, G., Ricken, W., and Seilacher, A. (Eds.), *Cycles and Events in Stratigraphy:* Berlin (Springer), 617–659.

van Morkhoven, F.P.C.M., Berggren, W.A., and Edwards, A.S., 1986. Cenozoic cosmopolitan deep-water benthic foraminifera. *Bull. Cent. Rech. Explor.-Prod. Elf-Aquitaine*, Mem. 11.

Watkins, D.K., and Verbeek, J.W., 1988. Calcareous nannofossil biostratigraphy from Leg 101, northern Bahamas. *In* Austin, J.A., Jr., Schlager, W., et al., *Proc. ODP, Sci. Results*, 101: College Station, TX (Ocean Drilling Program), 63–85.

Wilber, R.J., Milliman, J.D., and Halley, R.B., 1990. Accumulation of bank-top sediment on the western slope of Great Bahama Bank: rapid progradation of a carbonate megabank. *Geology*, 18:970–974.

Williams, S.C., 1985. Stratigraphy, facies evolution, and diagenesis of late Cenozoic limestones and dolomites, Little Bahama Bank, Bahamas [Ph.D. dissert.]. Univ. of Miami, Coral Gables.

Ms 166IR-106

NOTE: Core description forms ("barrel sheets") and core photographs can be found in Section 3, beginning on page 377. Forms containing smear slides can be found in Section 4, beginning on page 831. Thin sections can be found in Section 5, beginning on page 849. See the Table of Contents for material contained on CD-ROM.

SHORE-BASED LOG PROCESSING

Hole 1003D

Bottom felt: 494.5 mbrf
Total penetration: 677 mbsf
Total core recovered: none

Logging Runs

Logging string 1: DIT/SDT/GPIT/NGT
Logging string 2: FMS/GPIT/NGT
Logging string 3: APS/HLDS/HNGS
Logging string 4: ACT/GST/NGT
Logging string 5: WST

Wireline heave compensator was used to counter ship heave.

Bottom-Hole Assembly

The following bottom-hole assembly depths are as they appear on the logs after differential depth shift (see "Depth shift" section) and depth shift to the seafloor. As such, there might be a discrepancy with the original depths given by the drillers on board. Possible reasons for depth discrepancies are ship heave, use of wireline heave compensator, and drill string and/or wireline stretch.

DIT/SDT/GPIT/NGT: Bottom-hole assembly at ~106.5 mbsf.
FMS/GPIT/NGT: Bottom-hole assembly at ~106.5 mbsf.
APS/HLDS/HNGS: Bottom-hole assembly at ~106 mbsf.
ACT/GST/NGT: Did not reach bottom-hole assembly.

Processing

Depth shift: Original logs have been interactively depth shifted with reference to HNGS from APS/HLDS/HNGS run and to the seafloor (−493.5 m). This amount differs 1.0 m from the "bottom felt" depth given by the drillers and is based on correlation between logs and lithologic markers seen on core.

Gamma-ray environmental corrections: Corrections for borehole size and type of drilling fluid were performed on the NGT data from the FMS/GPIT/NGT and DIT/SDT/GPIT/NGT tool strings. HNGS data from the APS/HLDS/HNGS tool string were corrected in real-time during the recording.

Acoustic data processing: The array sonic tool was operated in standard depth-derived, borehole compensated, long spacing (8–10 and 10–12 ft) mode. The sonic logs were of very good quality and did not require any reprocessing.

Geochemical processing: For detailed explanation of the processing please refer to the "Explanatory Notes," this volume, or to the geochem.doc file on the enclosed CD-ROM. The elemental yields recorded by the GST tool represent the relative contribution of only some of the rock-forming elements (iron, calcium, chlorine, silicon, sulfur, hydrogen, gadolinium, and titanium—the last two computed during geochemical processing) to the total spectrum. Because other rock-forming elements are present in the formation (such as aluminum, potassium, etc.), caution is recommended in using the yields to infer lithologic changes. Instead, ratios are more appropriate to determine changes in the macroscopic properties of the formation. A list of the oxide/carbonate factors used in geochemical processing includes the following:

SiO_2 = 2.139
$CaCO_3$ = 2.497
K_2O = 1.205
Al_2O_3 = 1.889.

Quality Control

Data recorded through bottom-hole assembly such as the gamma ray data above 106 mbsf should be used only qualitatively because of the attenuation on the incoming signal. Invalid gamma ray data were recorded at 100 mbsf during the APS/HLDS/HNGS run and at 99–107 mbsf during the DIT/SDT/GPIT/NGT run.

Hole diameter was recorded by the caliper on the HLDS tool (LCAL) and the caliper on the FMS string (C_1 and C_2).

FACT = quality control curve in geochemical processing. Accuracy of the estimates is inversely proportional to the magnitude of the curve.

Details of standard shore-based processing procedures are found in the "Explanatory Notes" chapter, this volume. For further information about these logs, please contact:

Cristina Broglia
Phone: 914–365–8343
Fax: 914–365–3182
E-mail: chris@ldeo.columbia.edu

Zhiping Tu
Phone: 914–365–8336
Fax: 914–365–3182
E-mail: ztu@ldeo.columbia.edu

Hole 1003D: Natural Gamma Ray-Resistivity-Sonic Logging Data

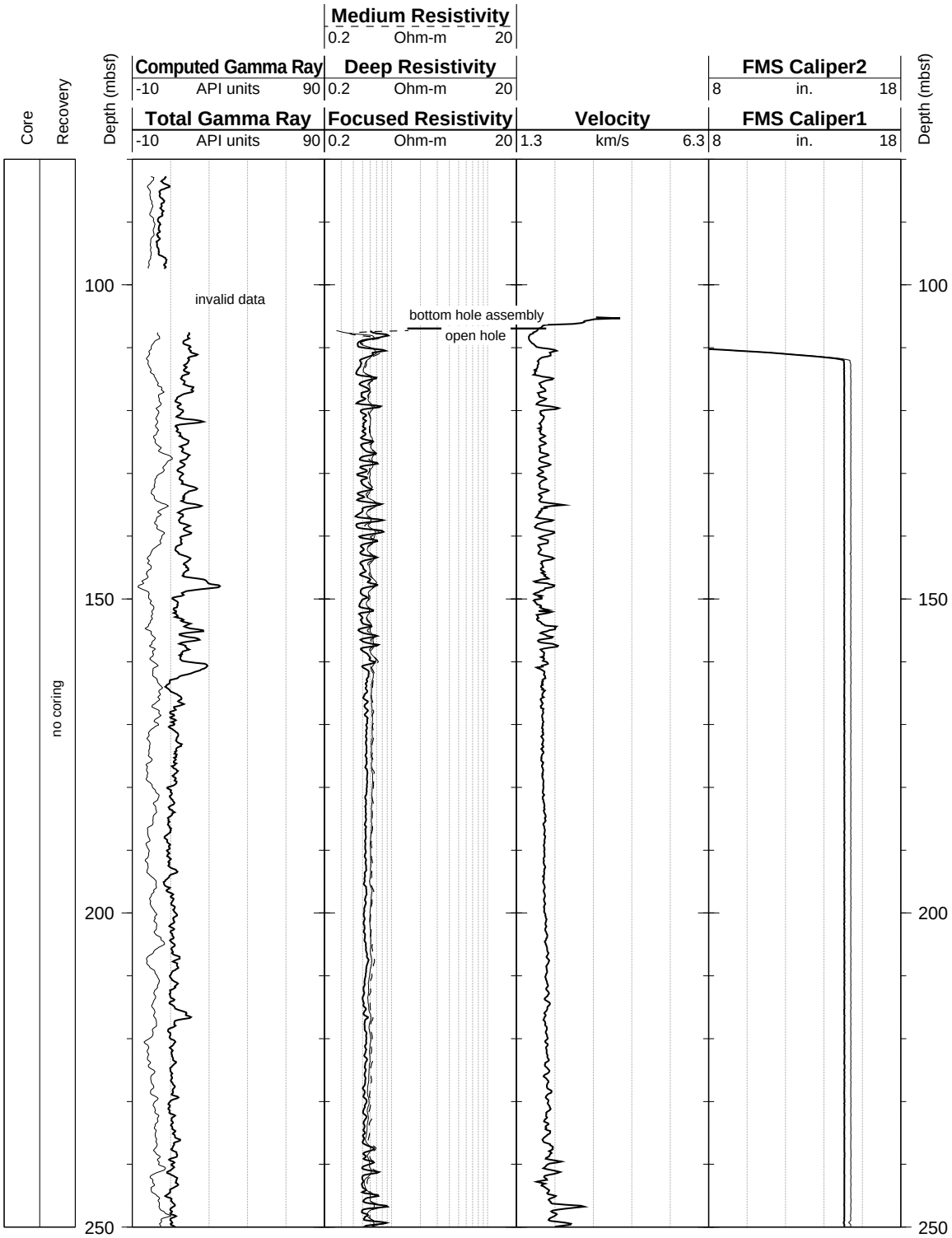

Hole 1003D: Natural Gamma Ray-Resistivity-Sonic Logging Data (cont.)

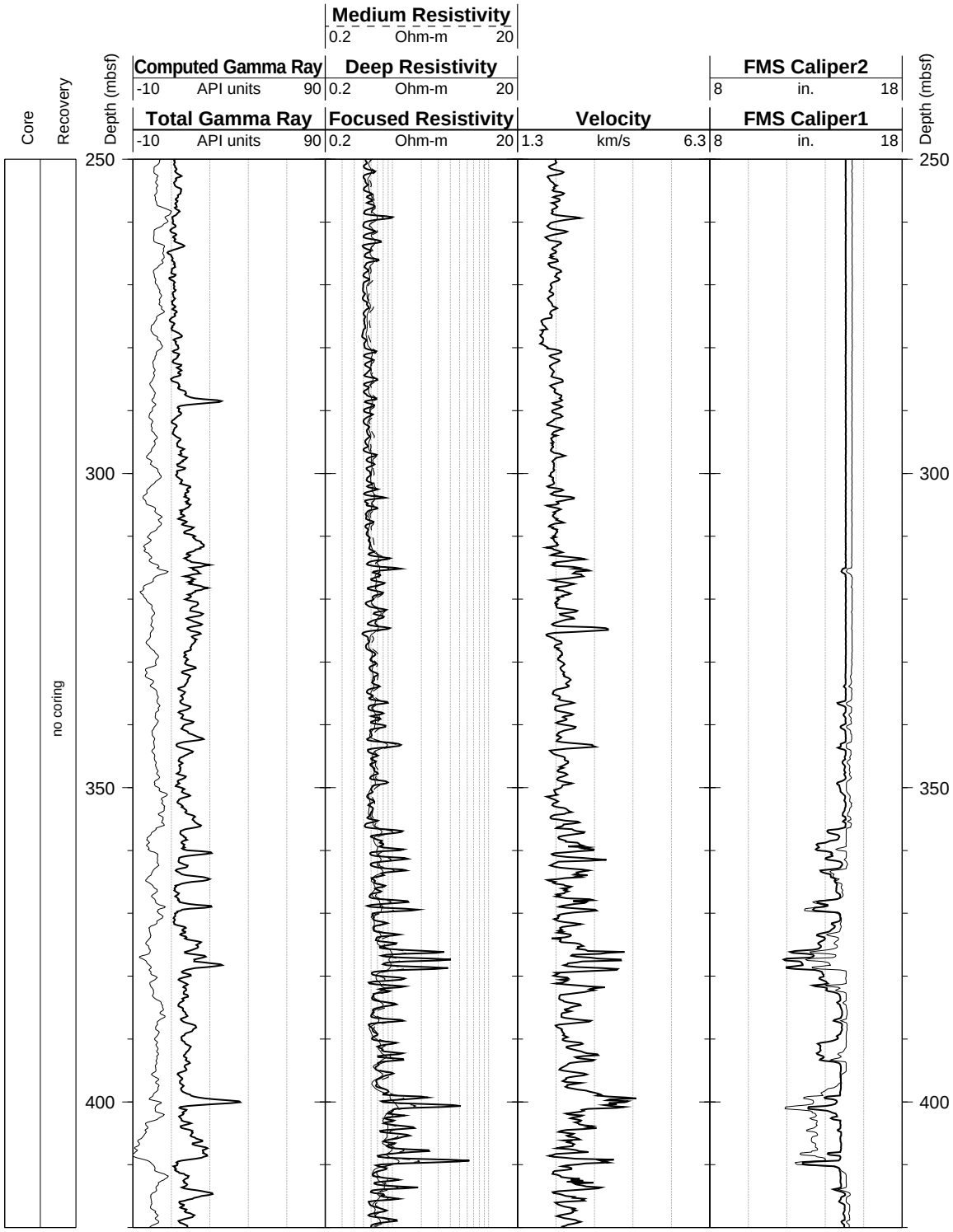

Hole 1003D: Natural Gamma Ray-Resistivity-Sonic Logging Data (cont.)

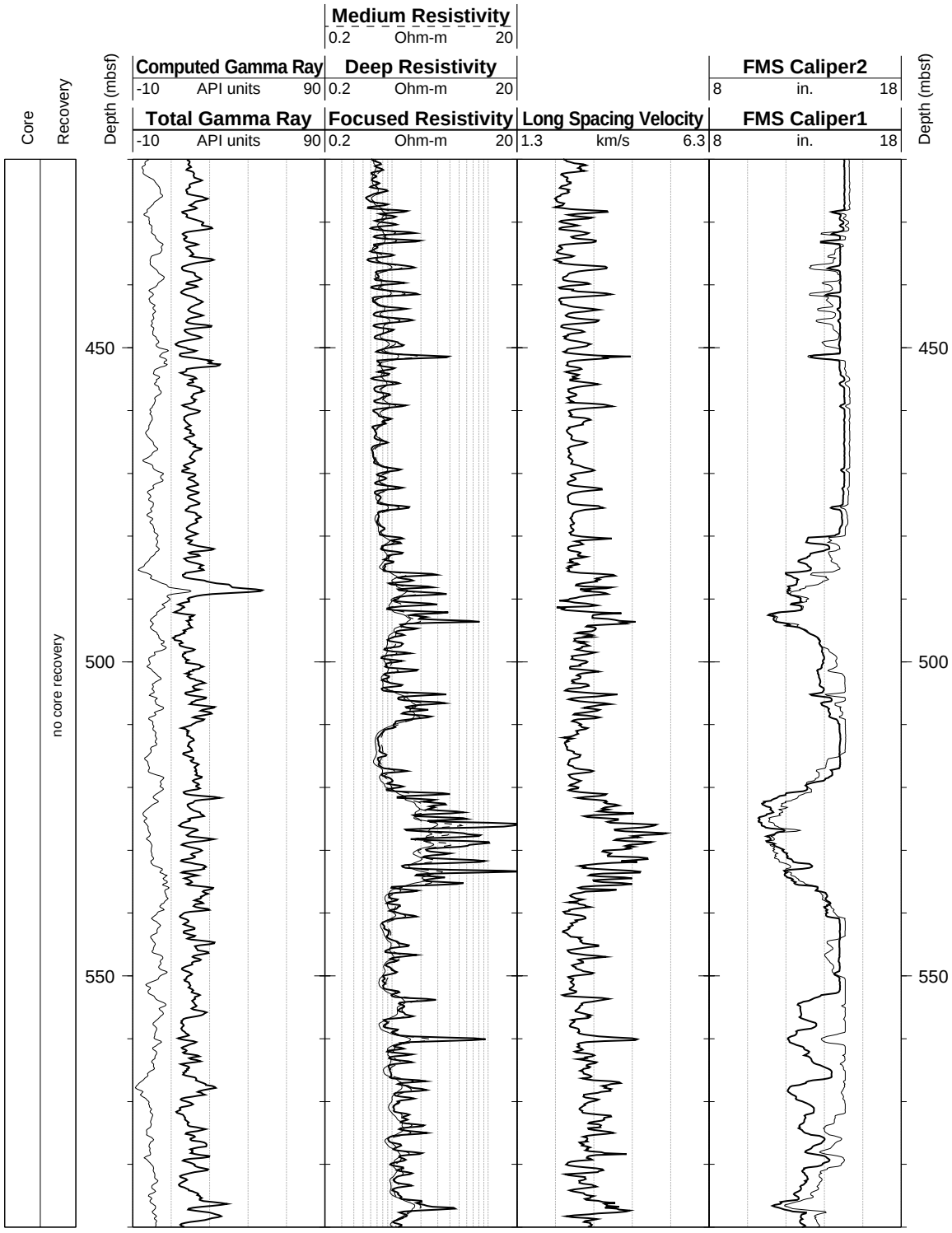

Hole 1003D: Natural Gamma Ray-Resistivity-Sonic Logging Data (cont.)

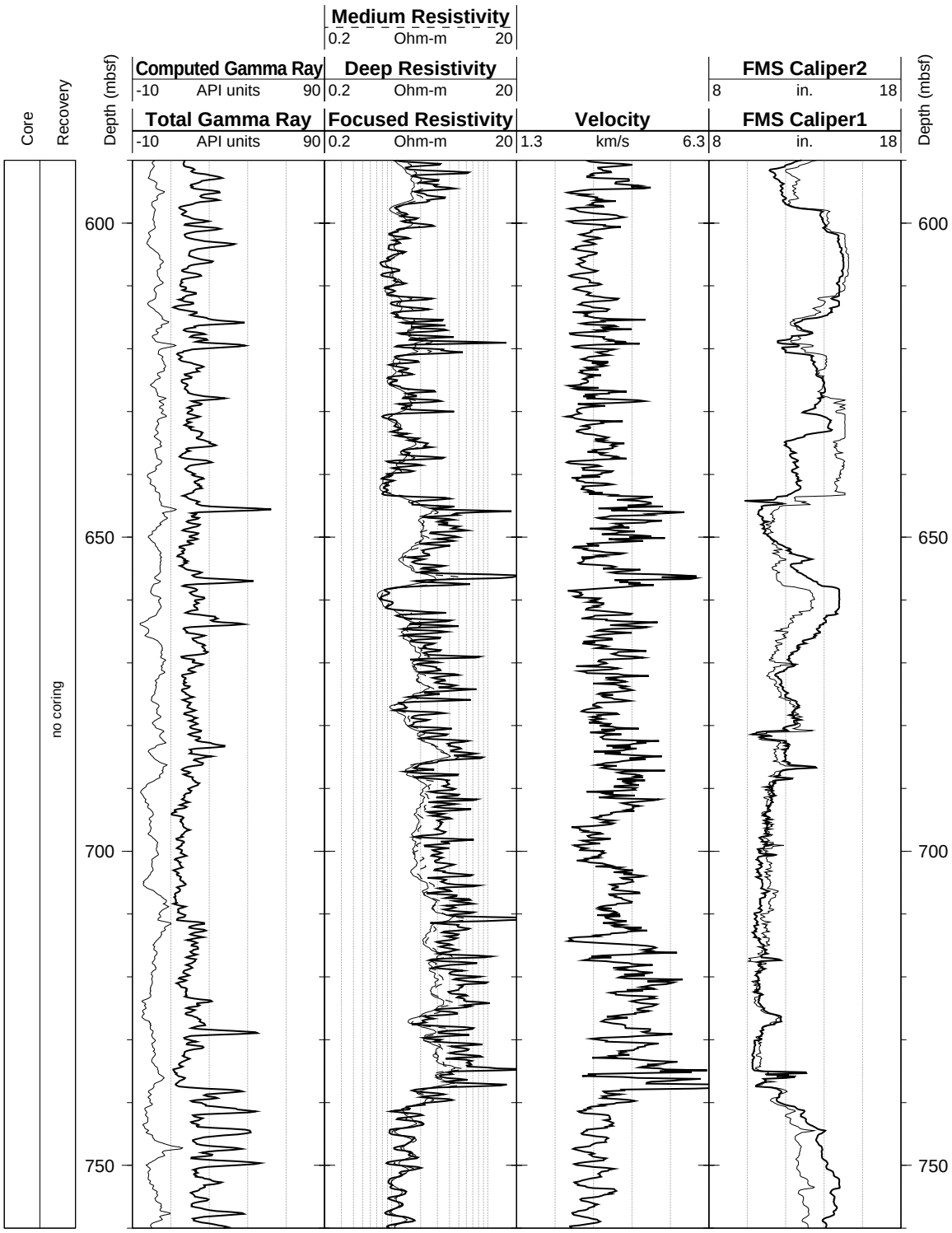

Hole 1003D: Natural Gamma Ray-Resistivity-Sonic Logging Data (cont.)

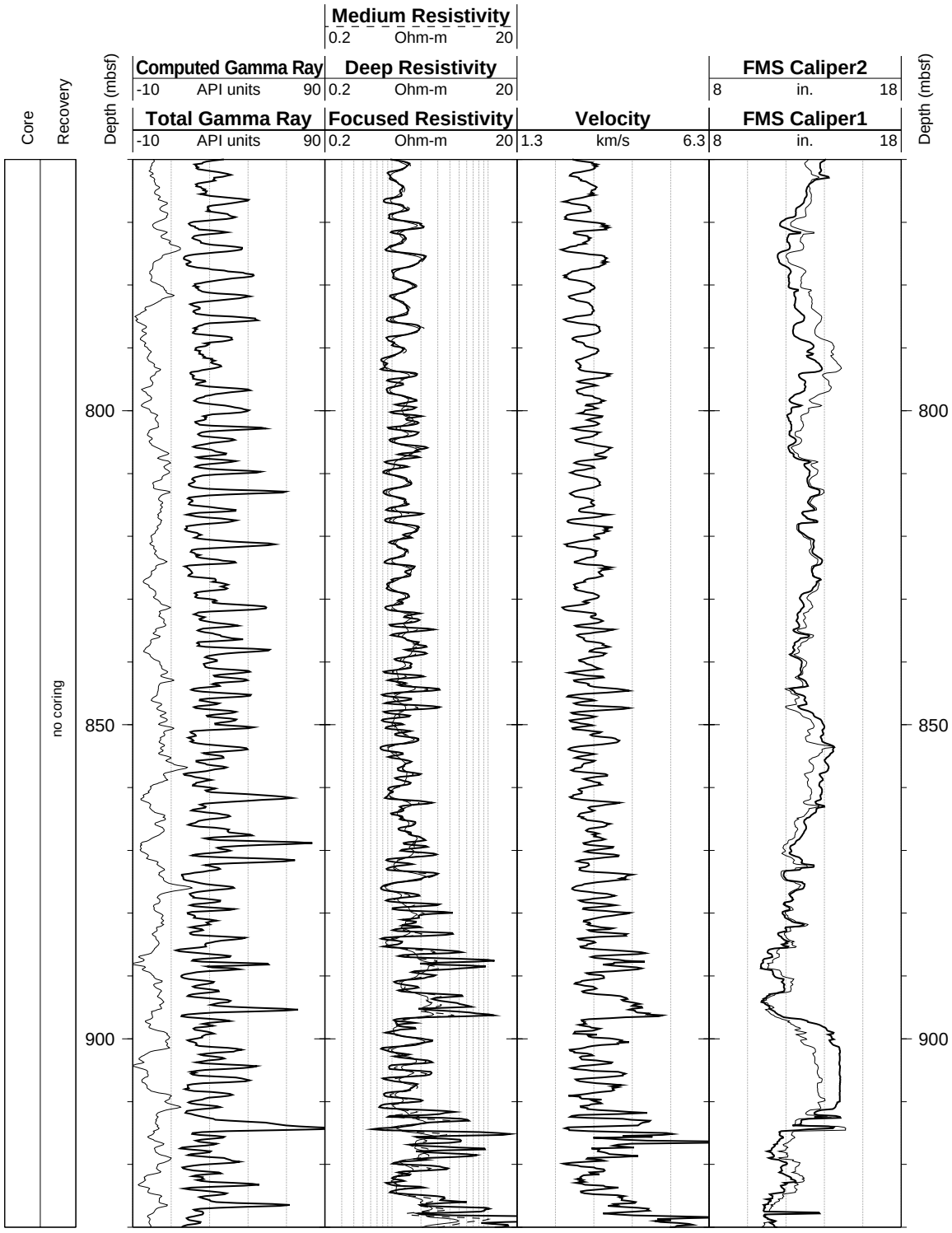

Hole 1003D: Natural Gamma Ray-Resistivity-Sonic Logging Data (cont.)

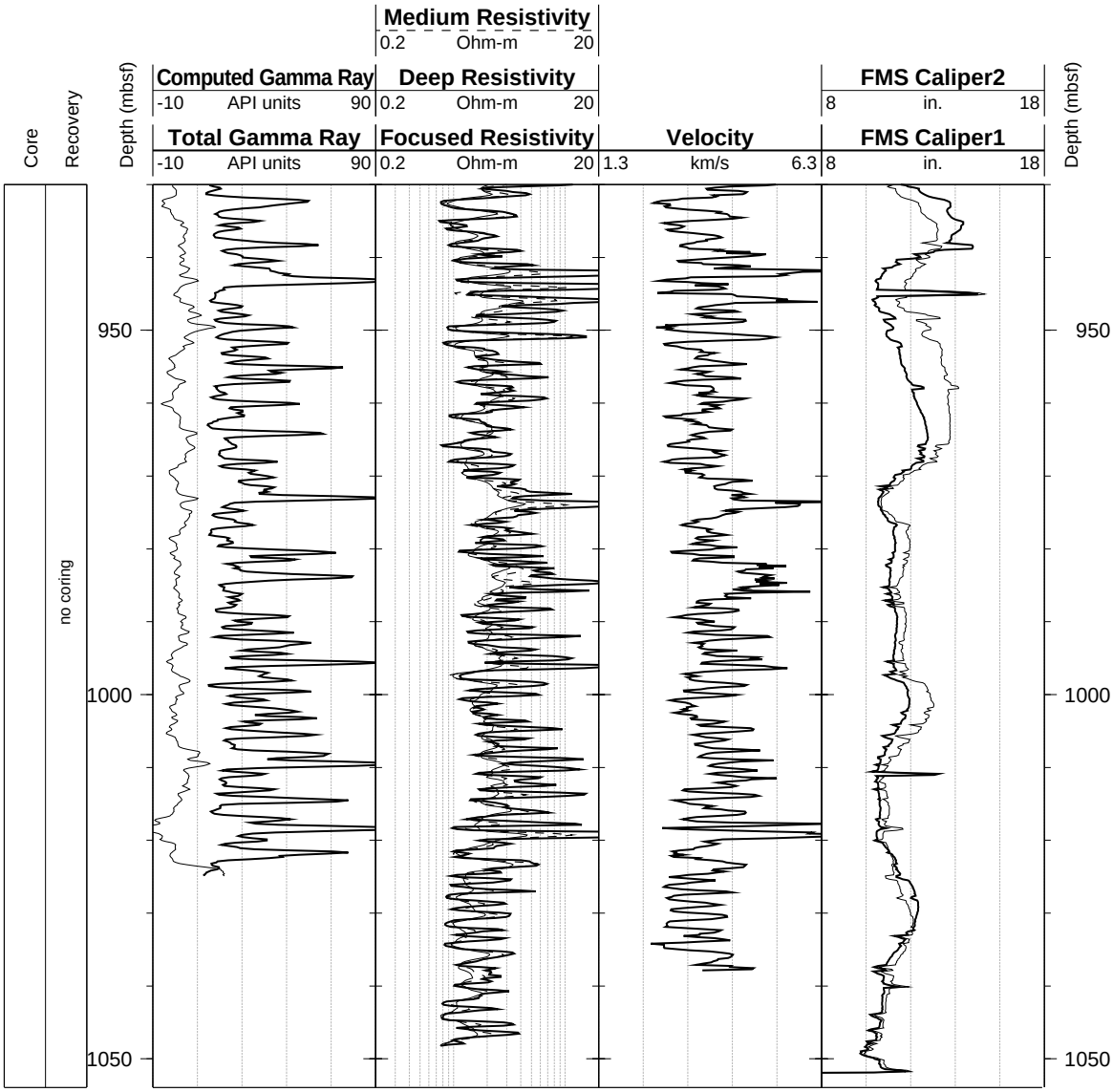

Hole 1003D: Natural Gamma Ray Logging Data

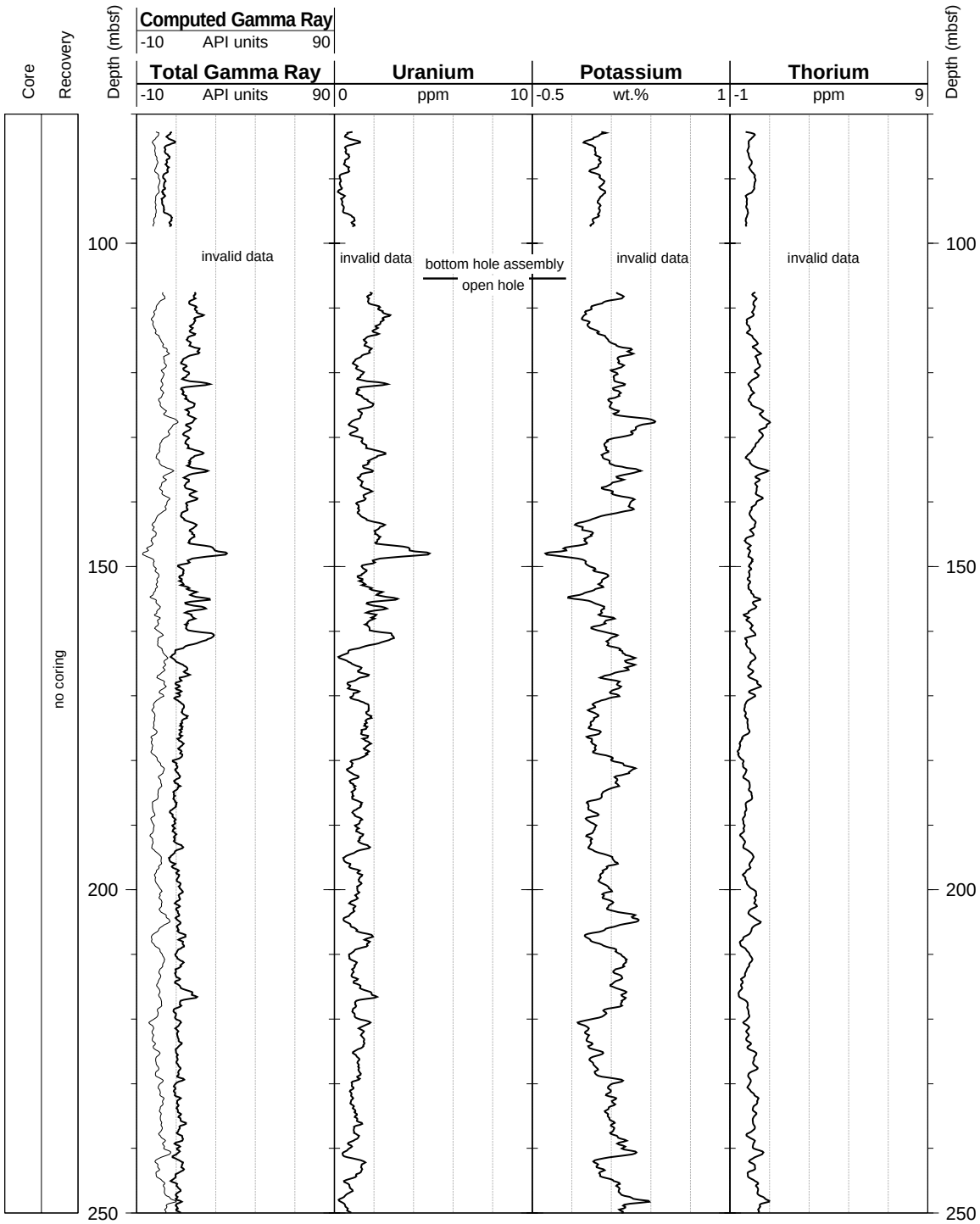

Hole 1003D: Natural Gamma Ray Logging Data (cont.)

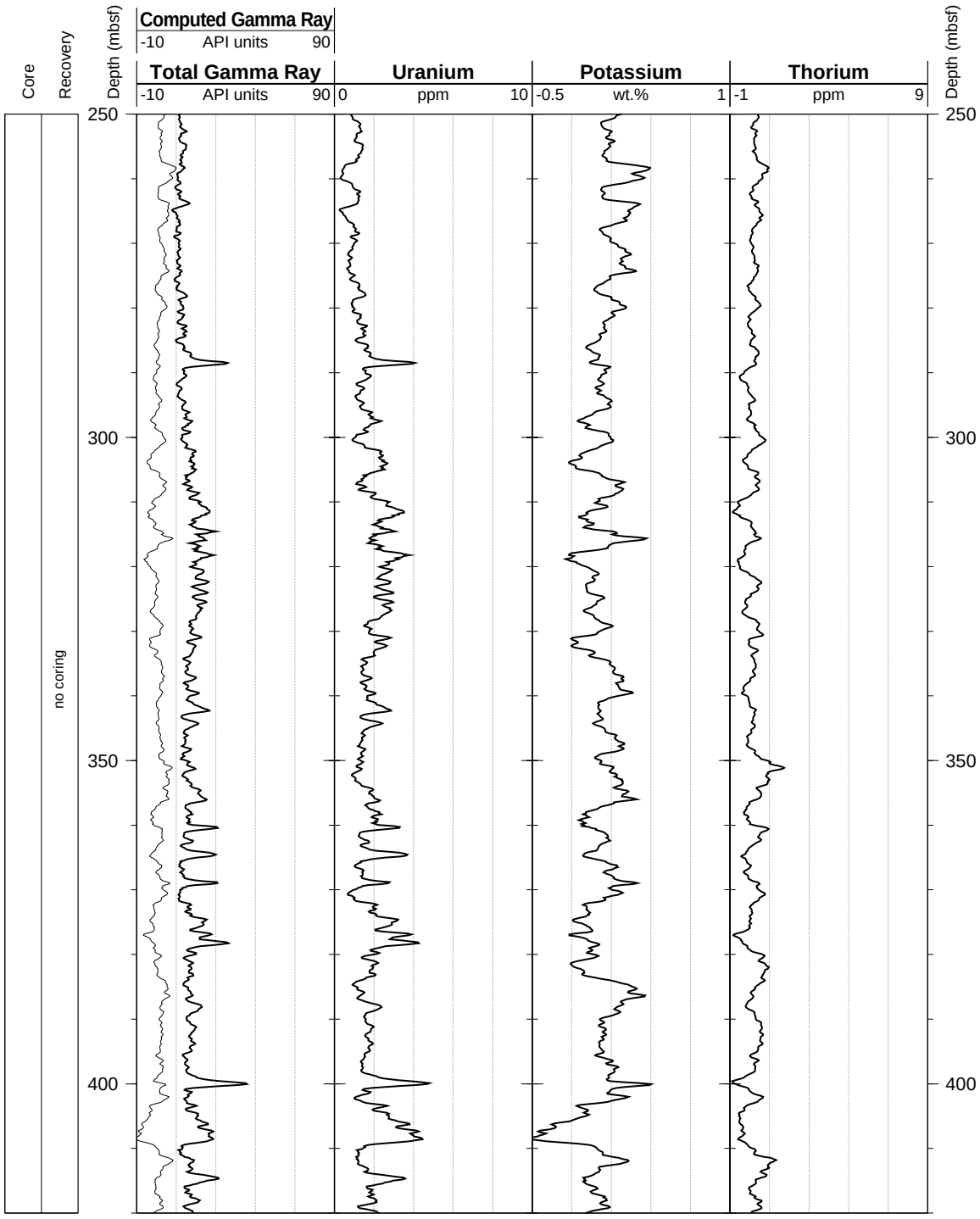

Hole 1003D: Natural Gamma Ray Logging Data (cont.)

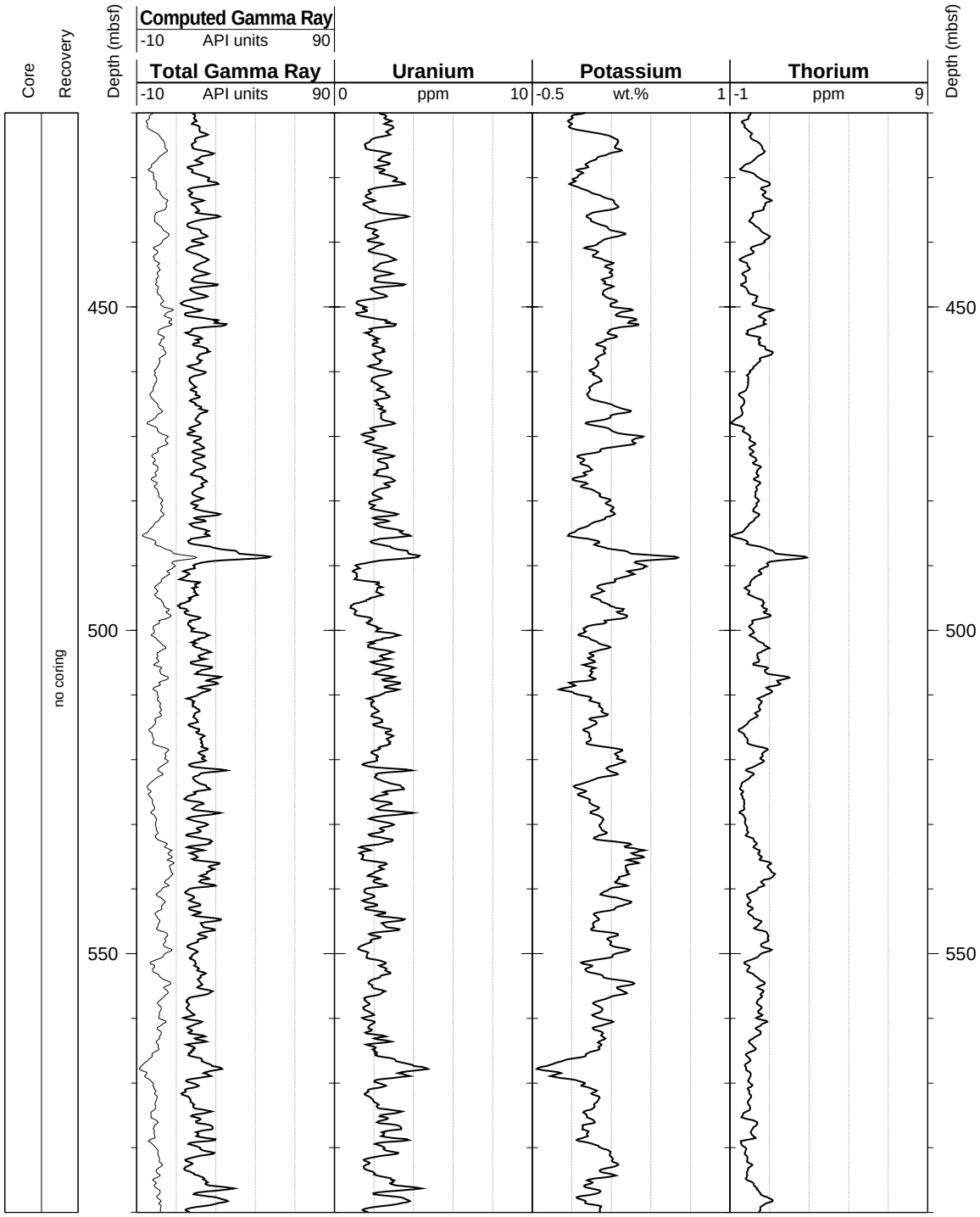

Hole 1003D: Natural Gamma Ray Logging Data (cont.)

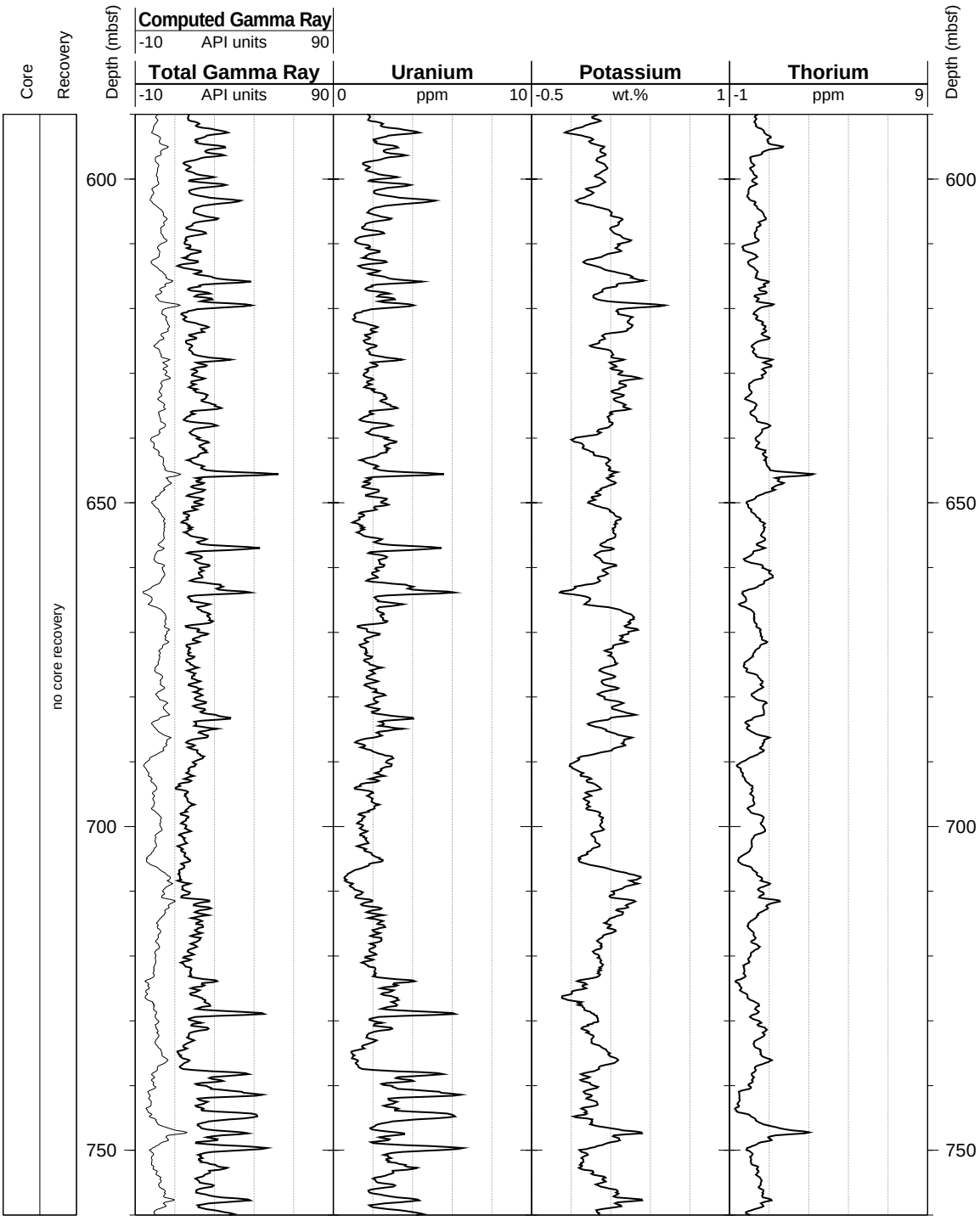

Hole 1003D: Natural Gamma Ray Logging Data (cont.)

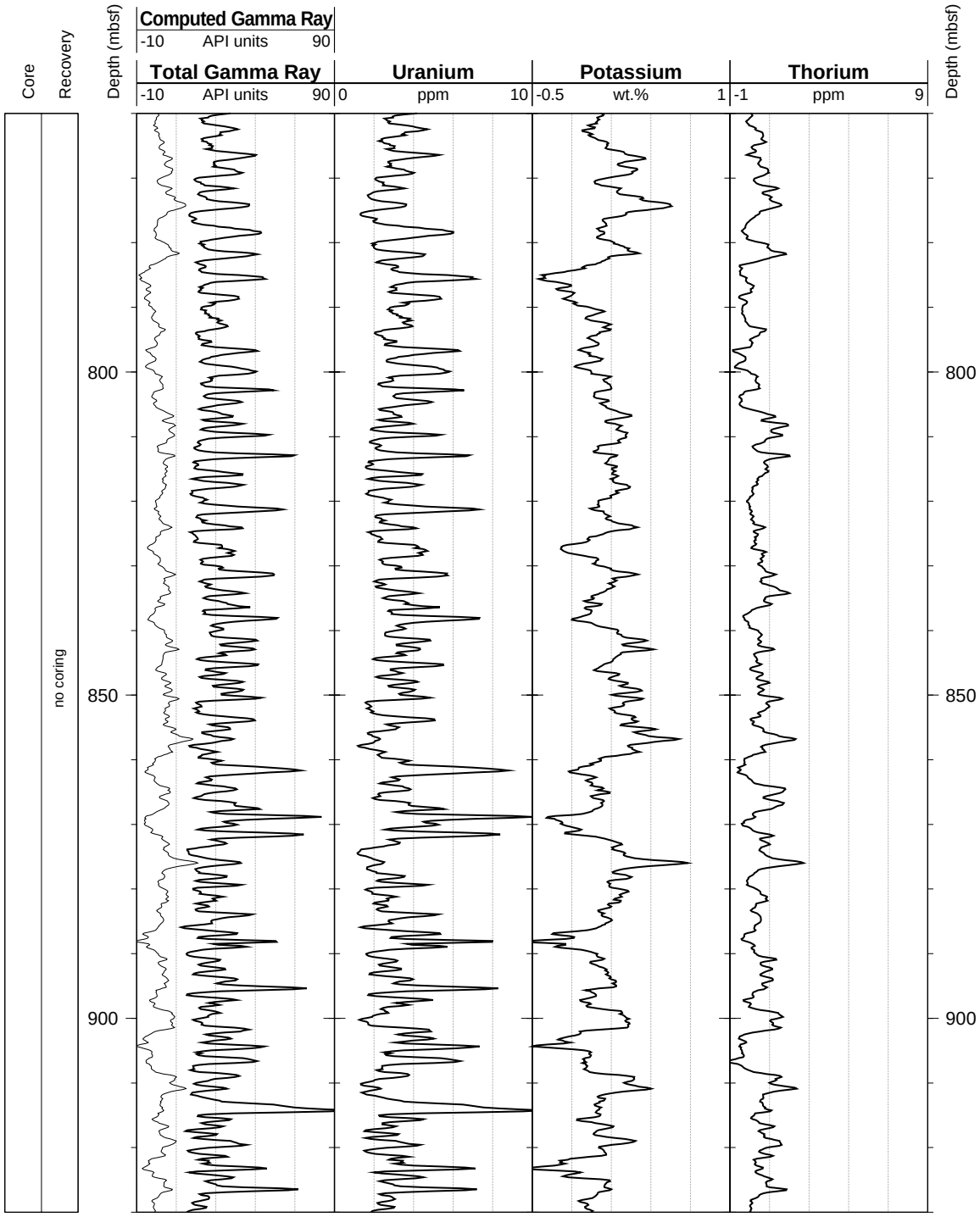

Hole 1003D: Natural Gamma Ray Logging Data (cont.)

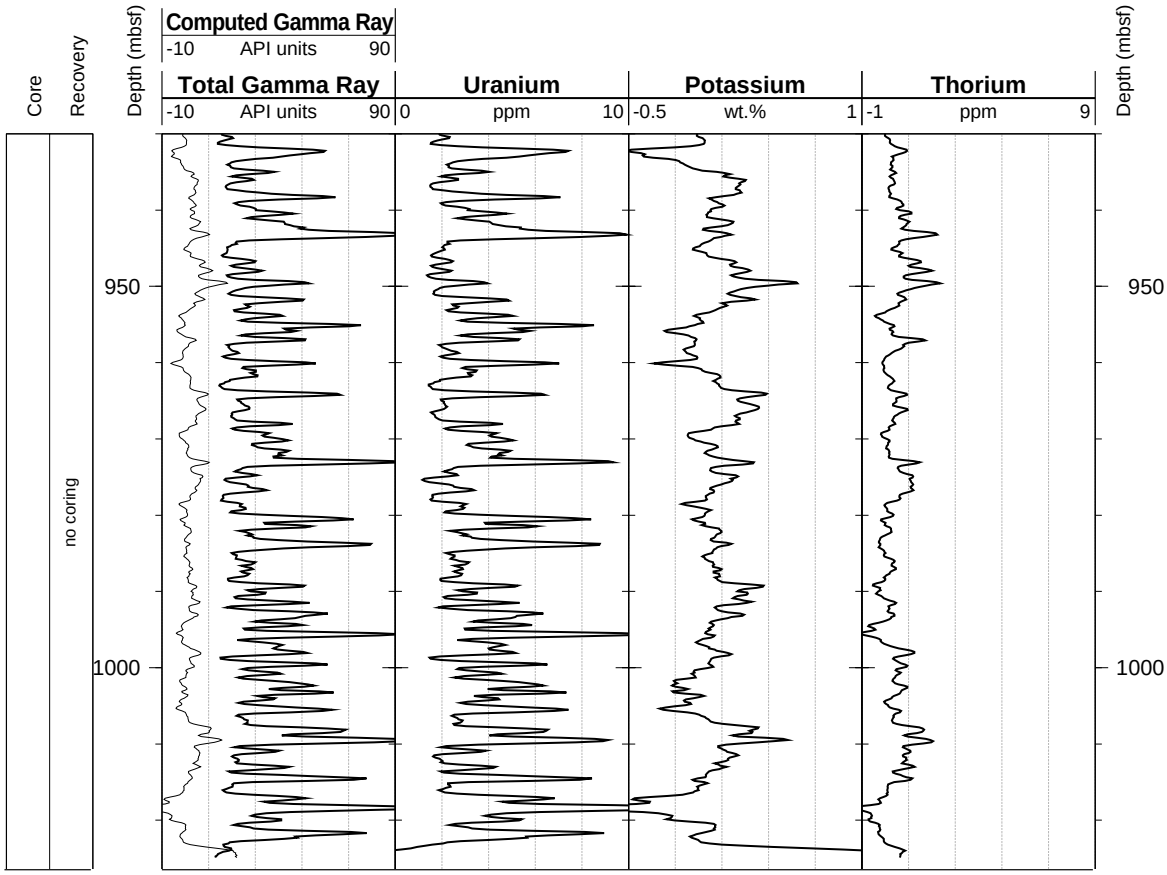

Hole 1003D: Natural Gamma Ray-Density-Porosity Logging Data

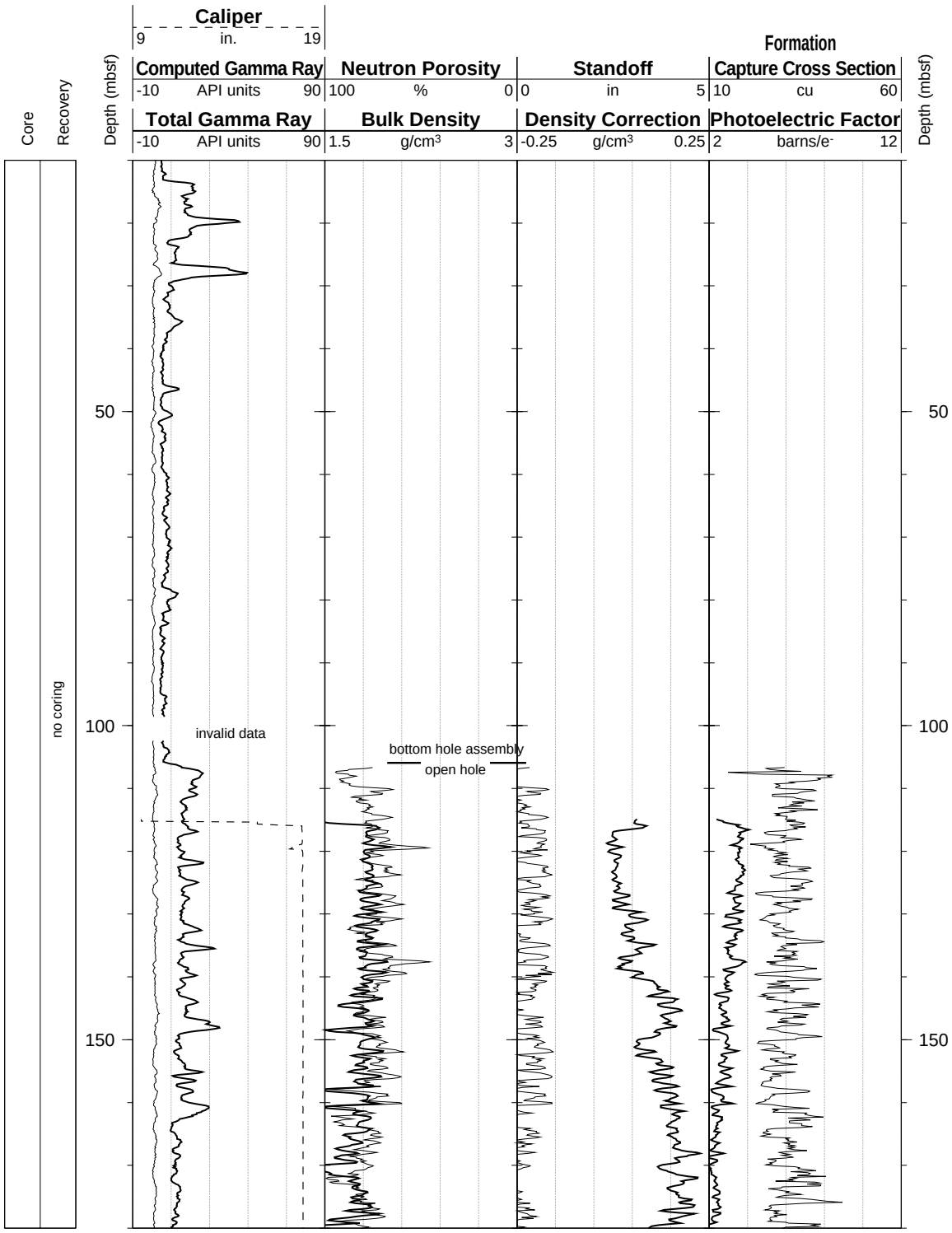

Hole 1003D: Natural Gamma Ray-Density-Porosity Logging Data (cont.)

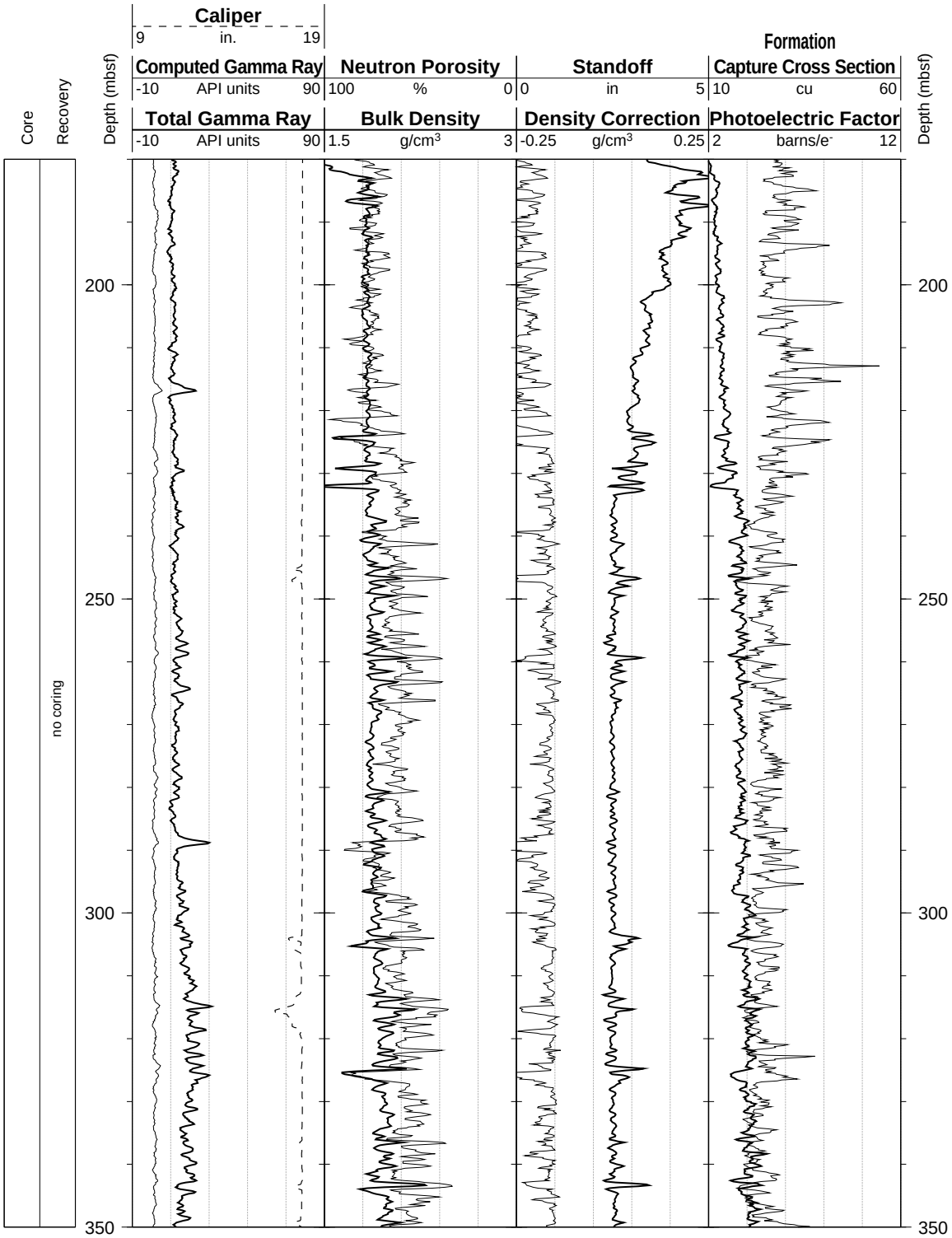

Hole 1003D: Natural Gamma Ray-Density-Porosity Logging Data (cont.)

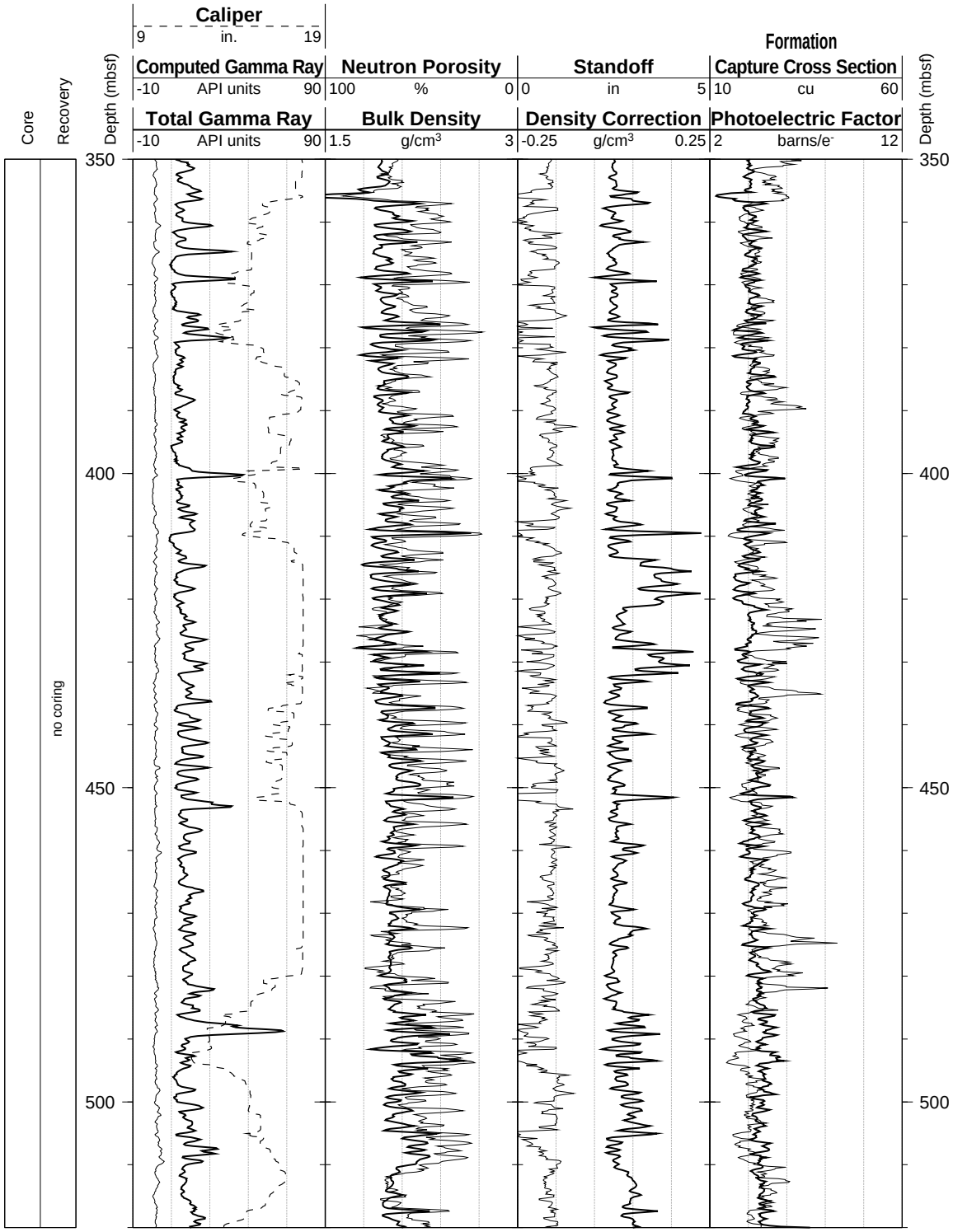

Hole 1003D: Natural Gamma Ray-Density-Porosity Logging Data (cont.)

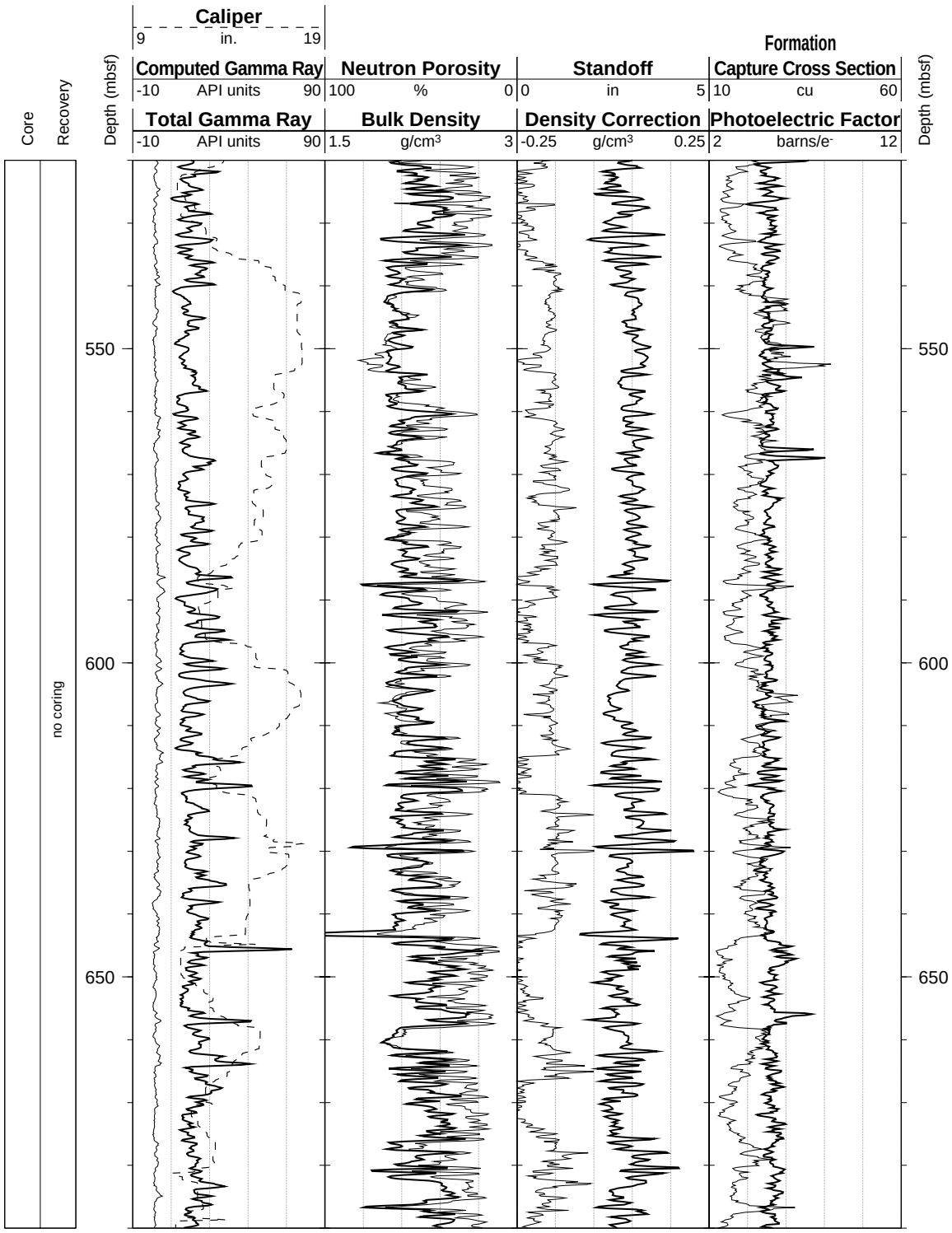

Hole 1003D: Natural Gamma Ray-Density-Porosity Logging Data (cont.)

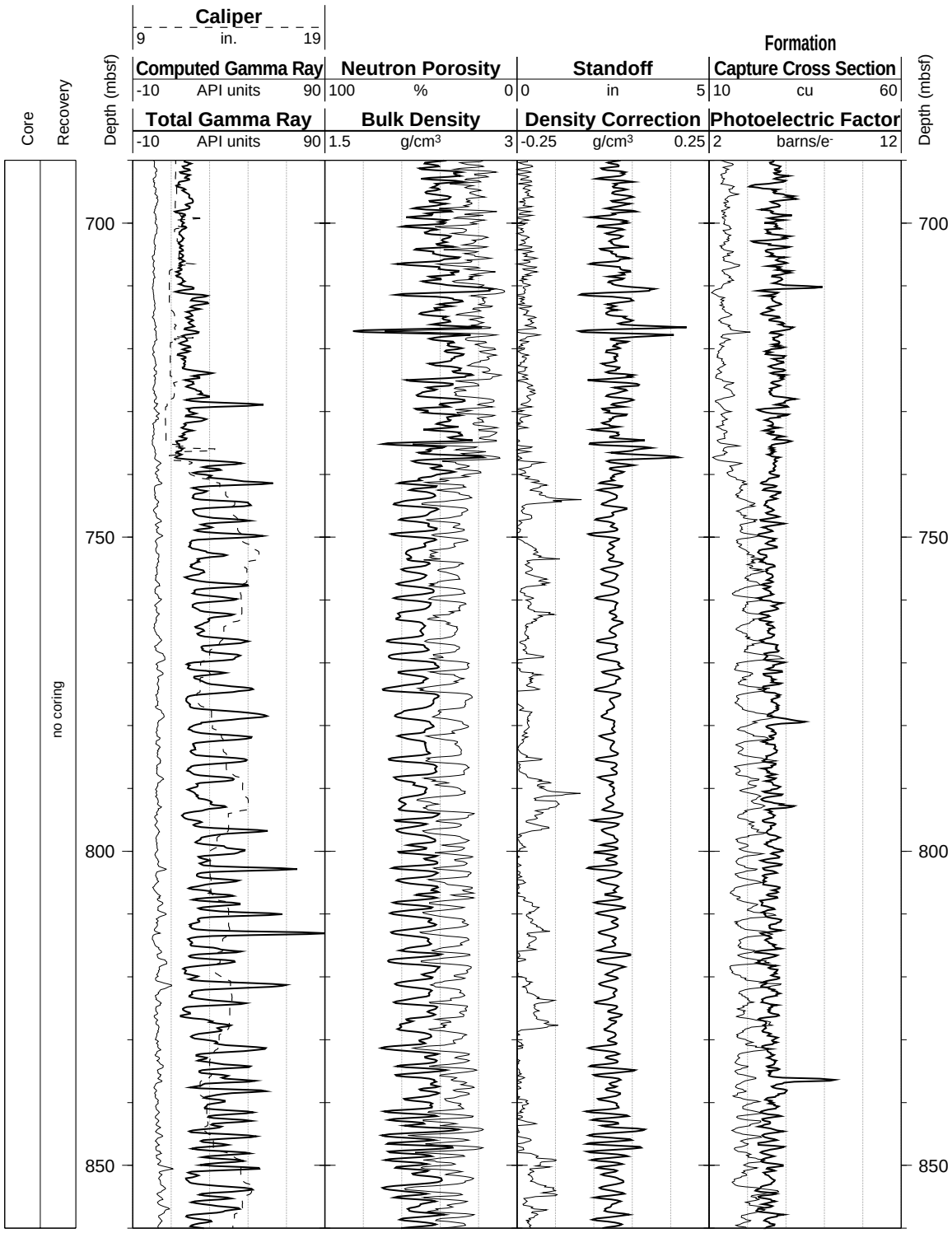

Hole 1003D: Natural Gamma Ray-Density-Porosity Logging Data (cont.)

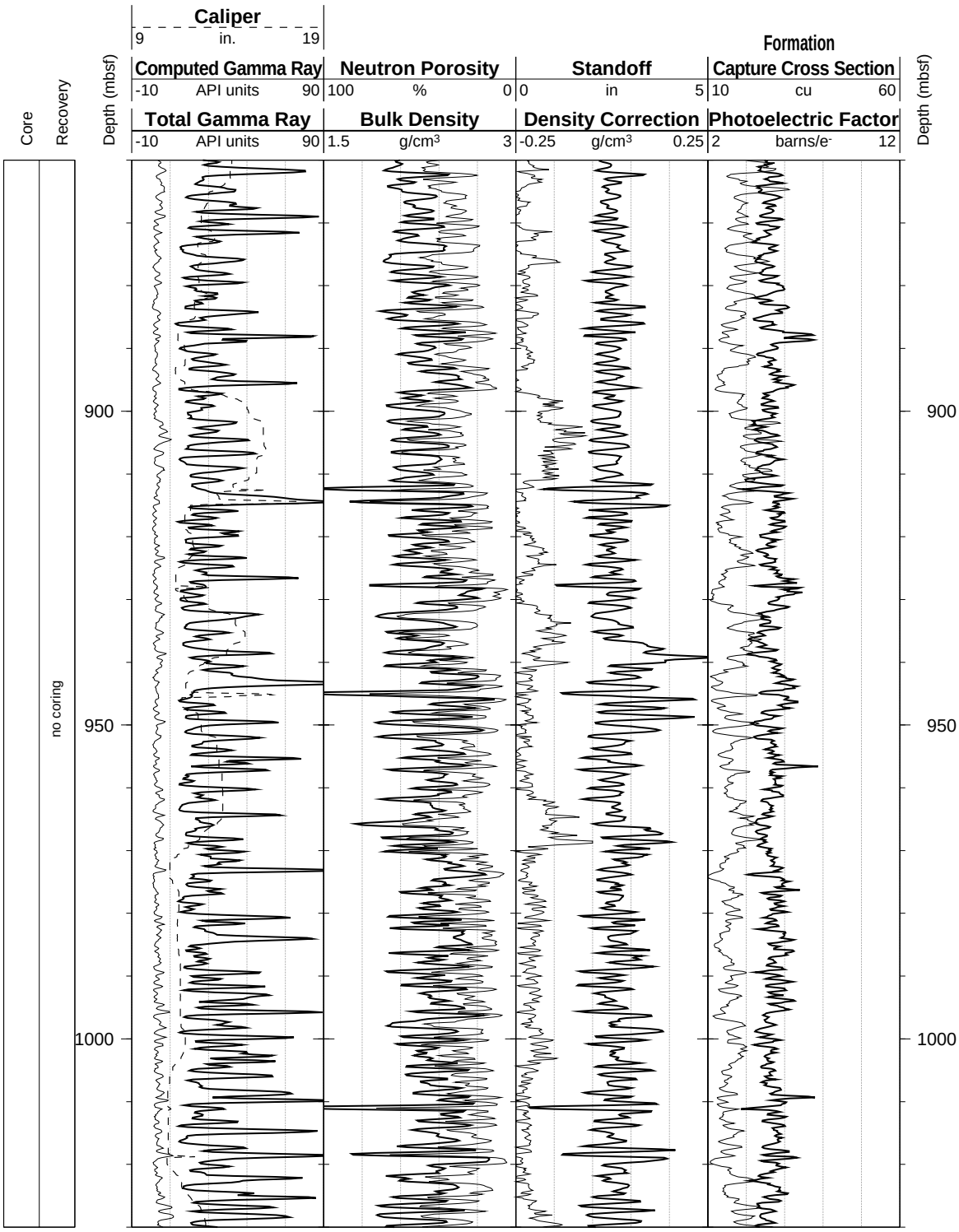

Hole 1003D: Natural Gamma Ray-Density-Porosity Logging Data (cont.)

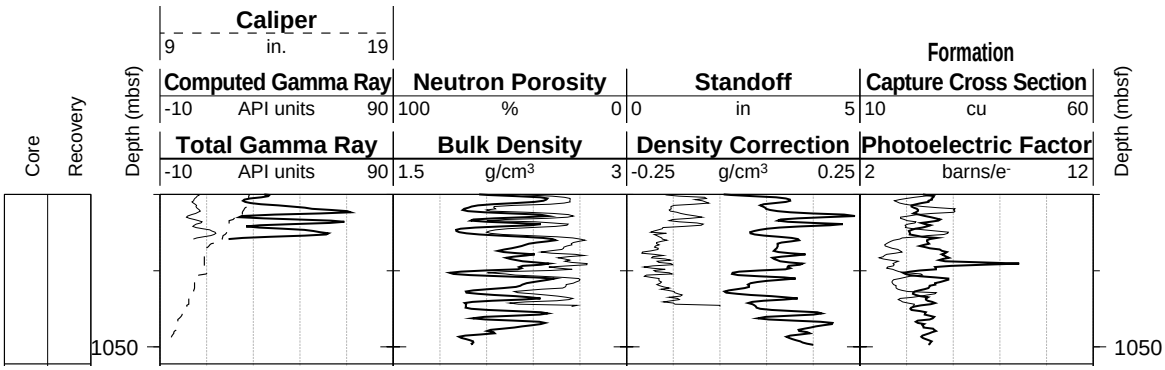

Hole 1003D: Natural Gamma Ray Logging Data

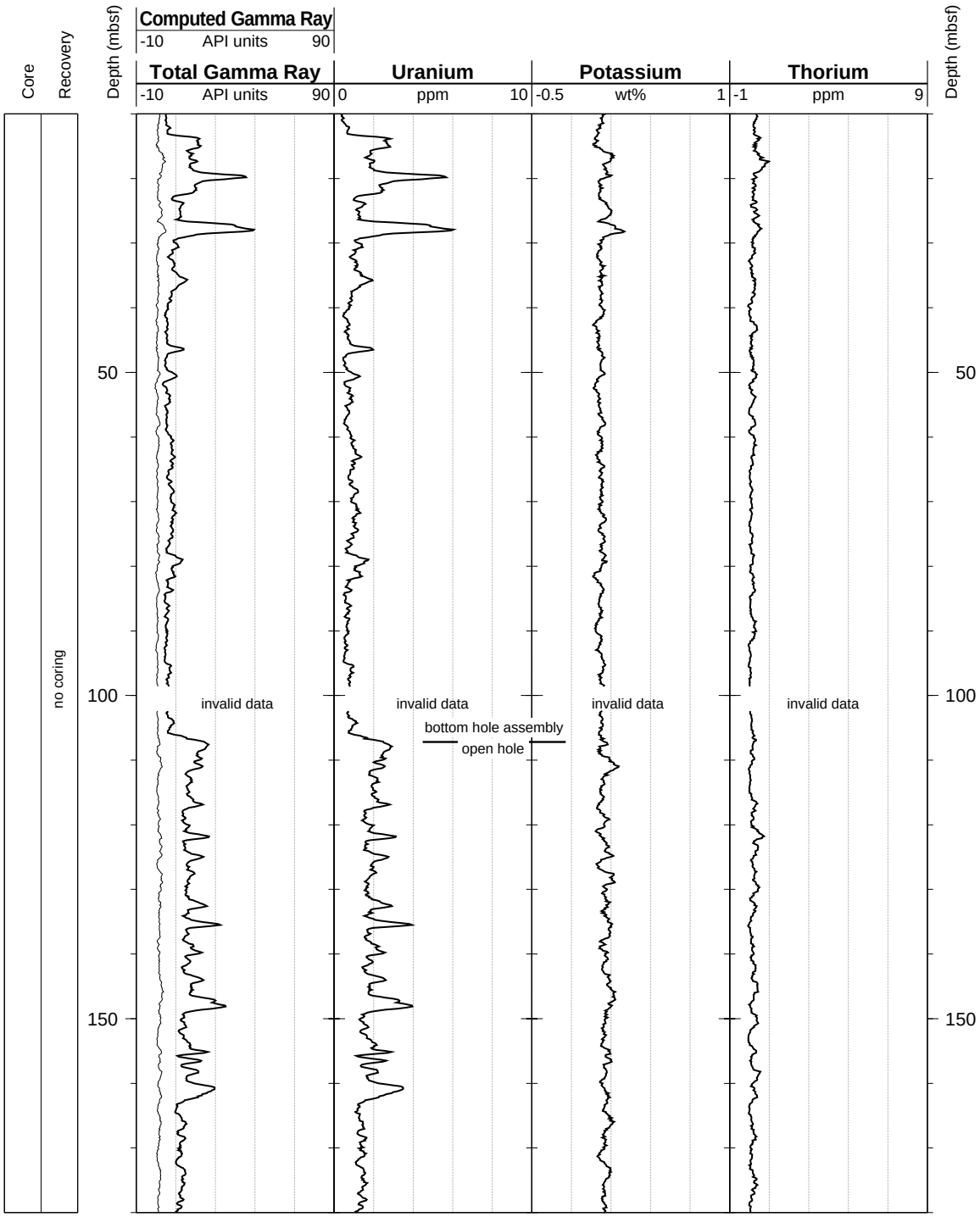

Hole 1003D: Natural Gamma Ray Logging Data (cont.)

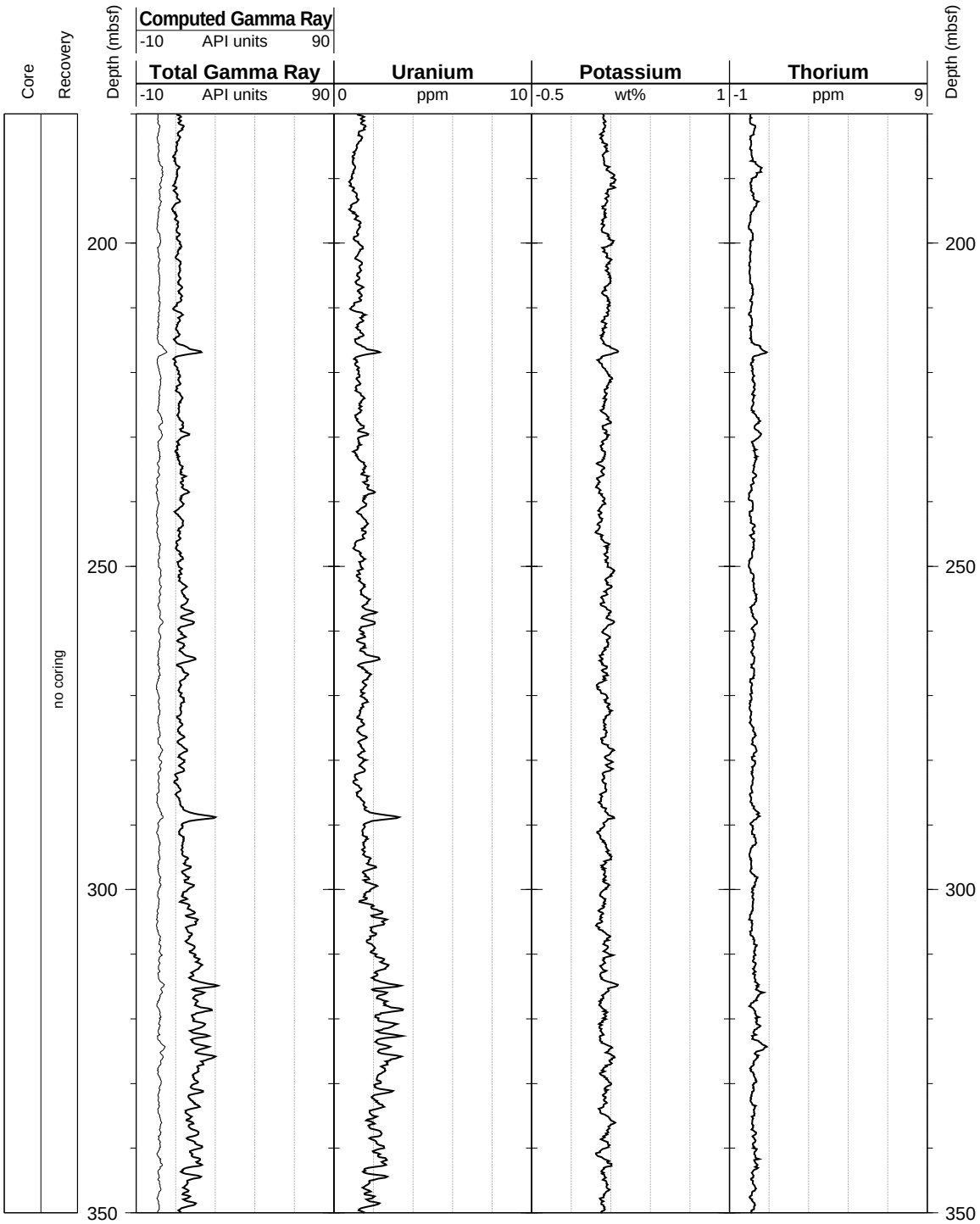

Hole 1003D: Natural Gamma Ray Logging Data (cont.)

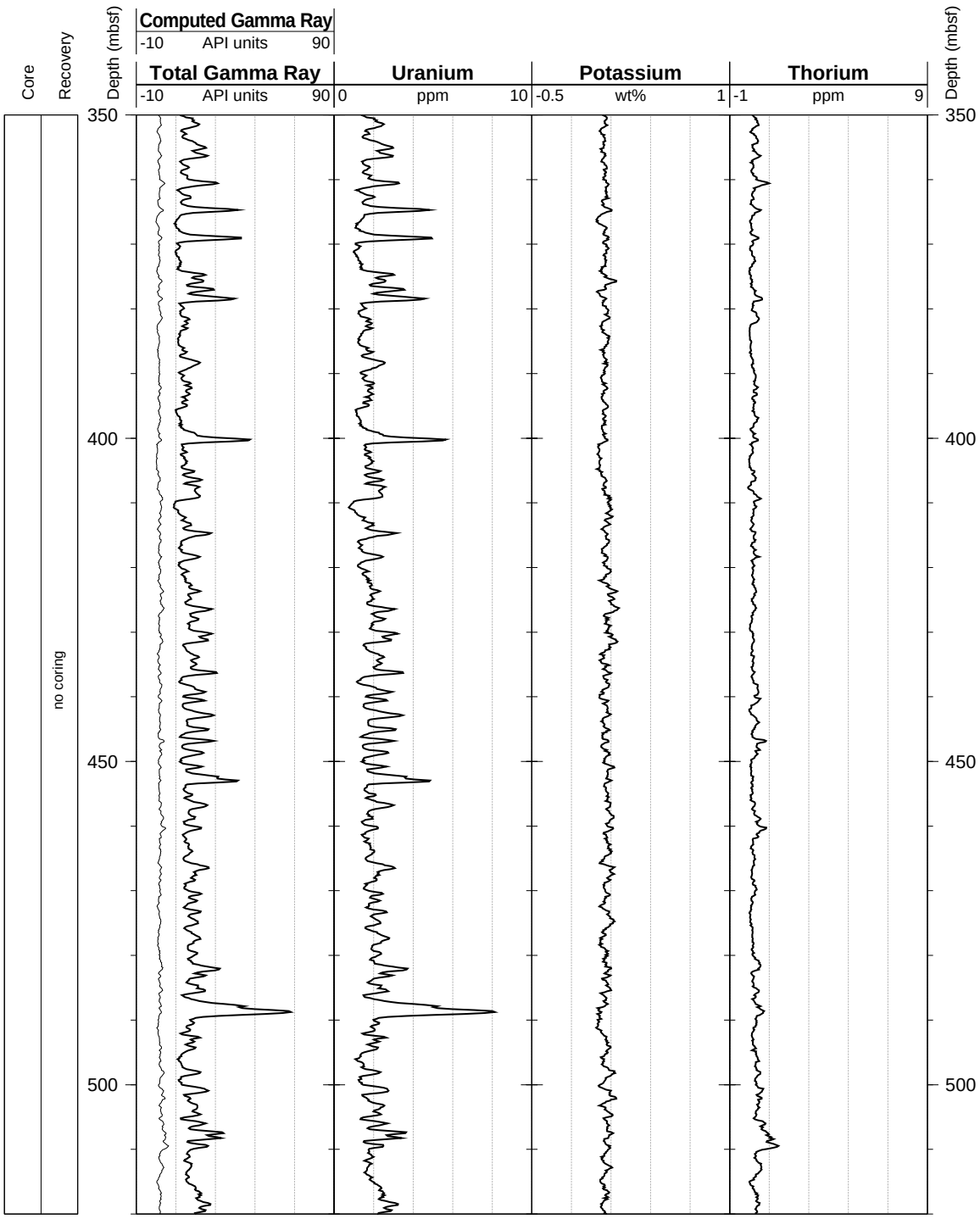

Hole 1003D: Natural Gamma Ray Logging Data (cont.)

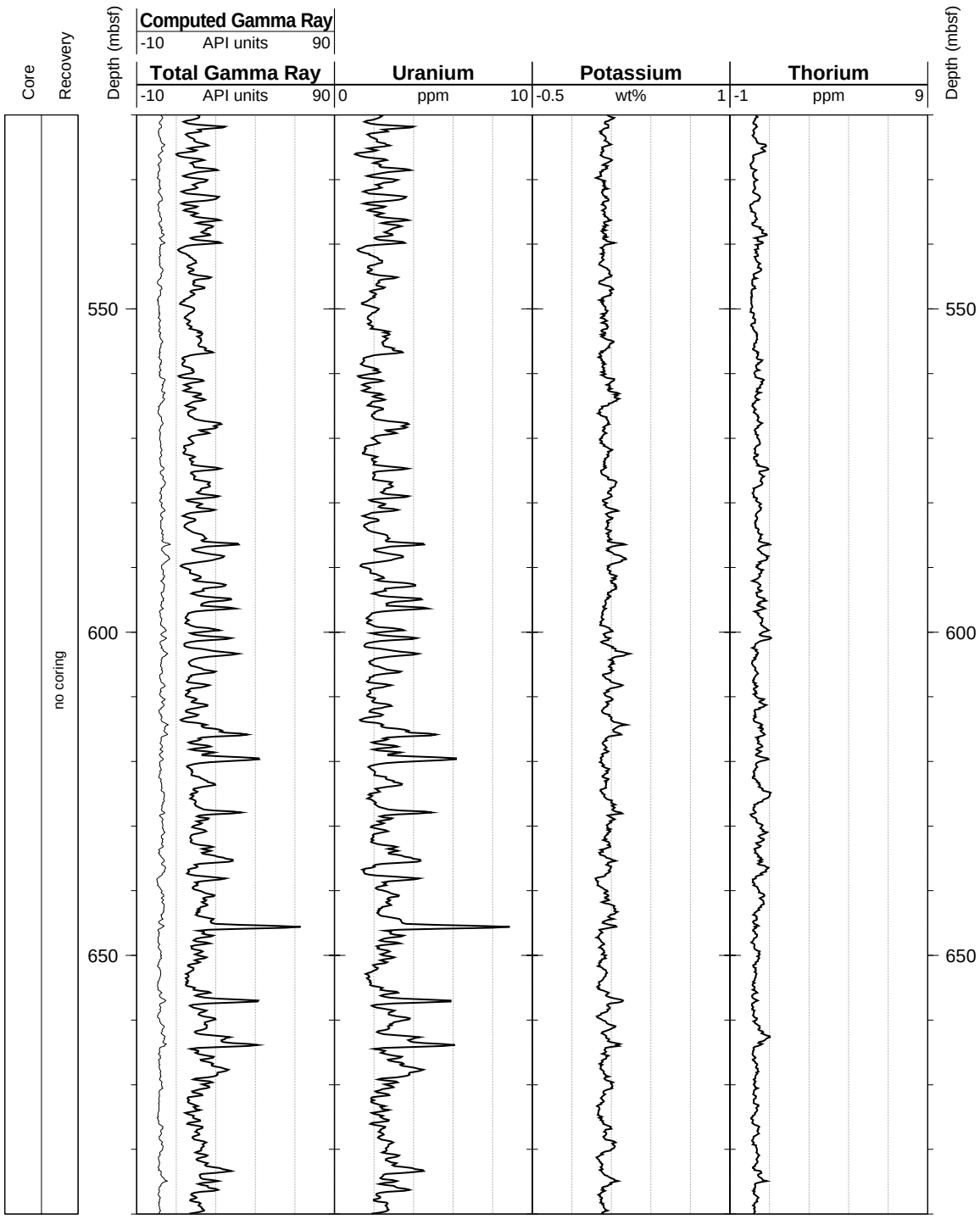

Hole 1003D: Natural Gamma Ray Logging Data (cont.)

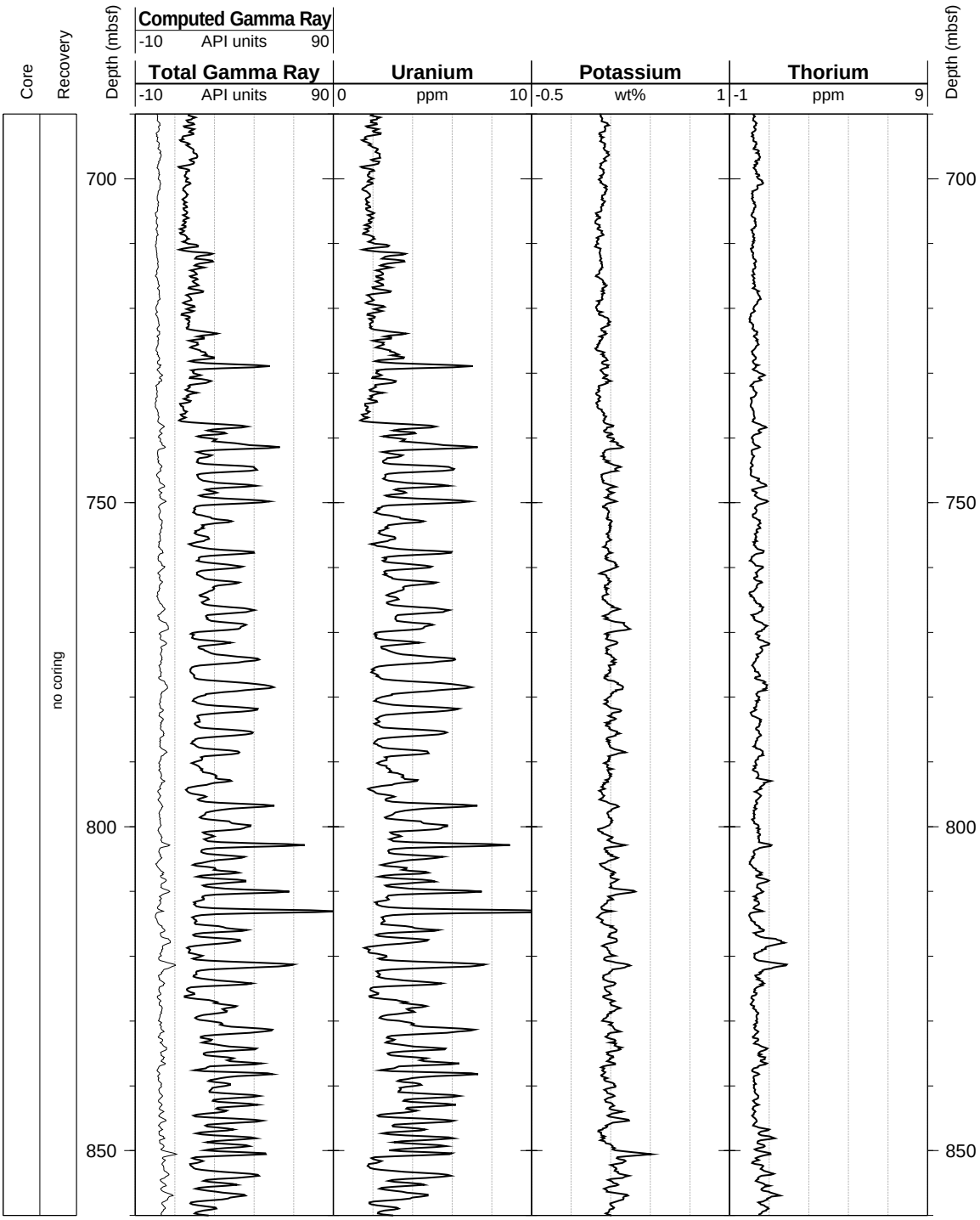

Hole 1003D: Natural Gamma Ray Logging Data (cont.)

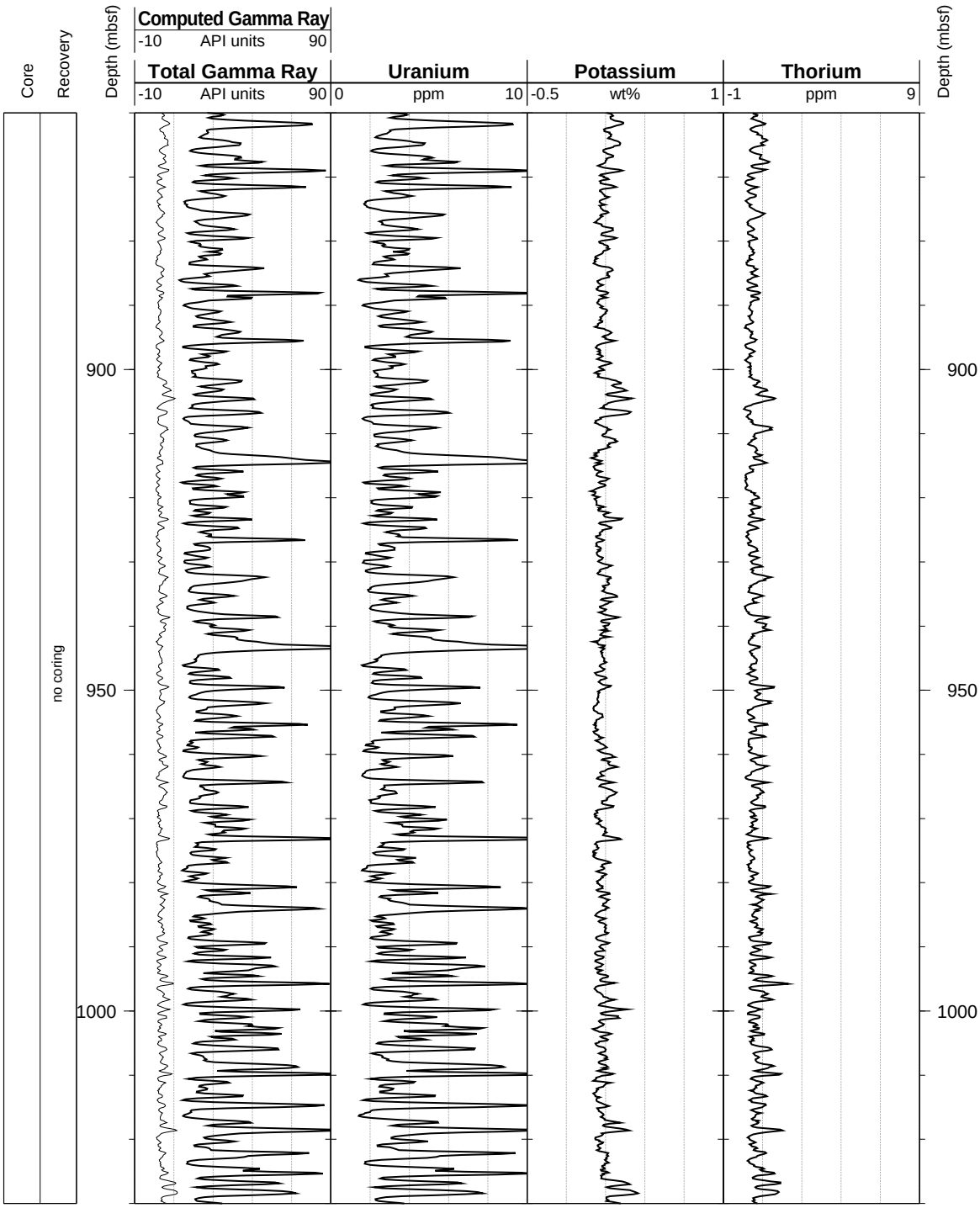

Hole 1003D: Natural Gamma Ray Logging Data (cont.)

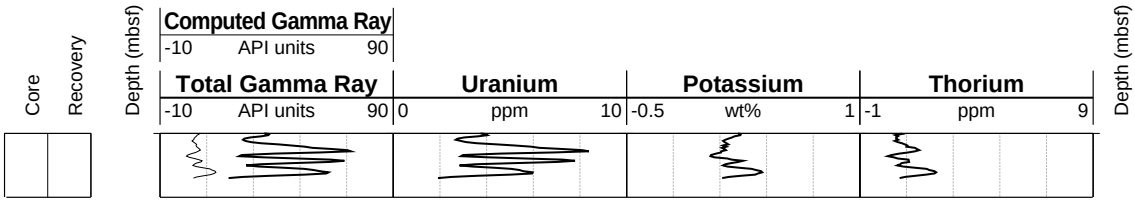

Hole 1003D: Geochemical Logging Data

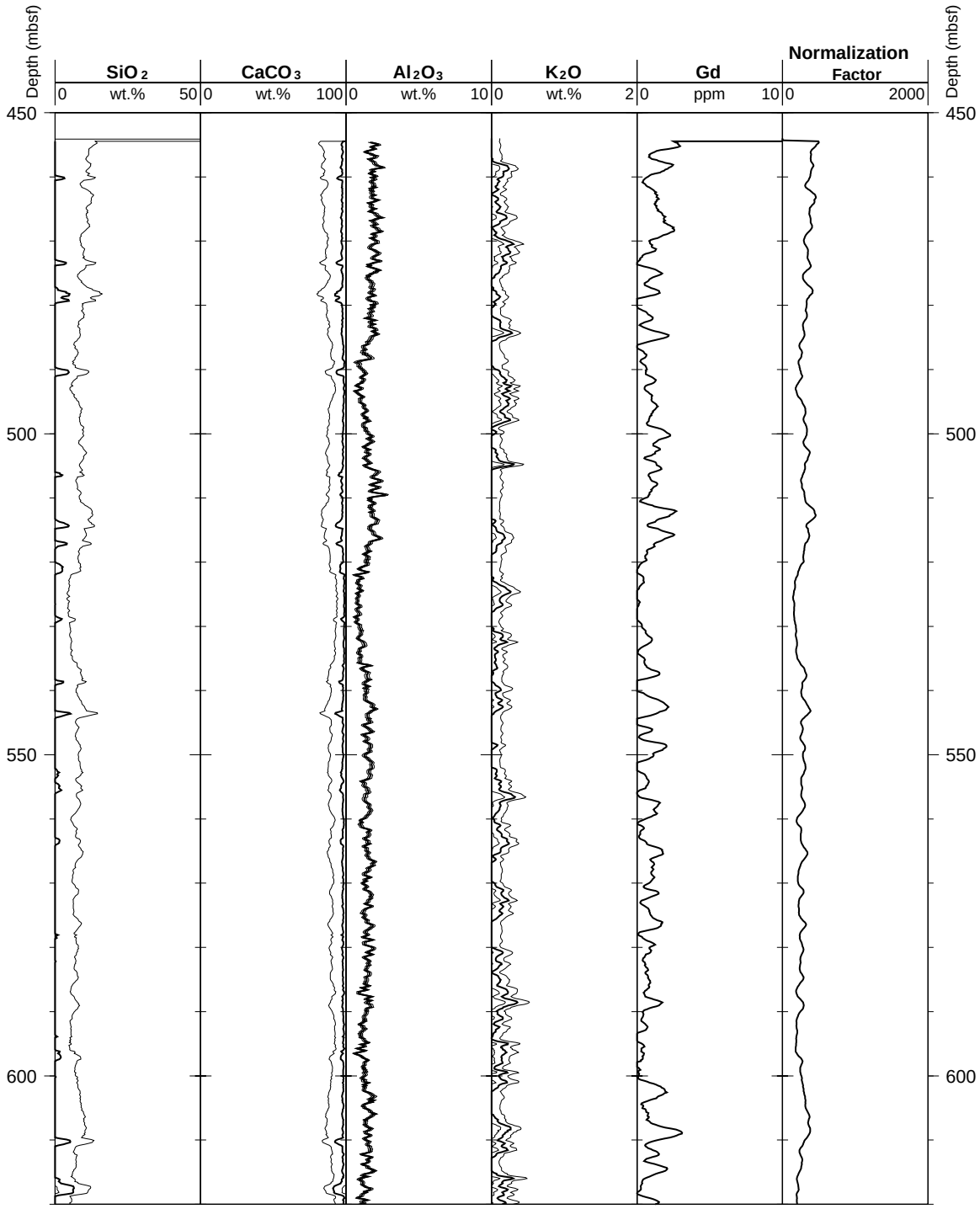

Hole 1003D: Geochemical Logging Data (cont.)

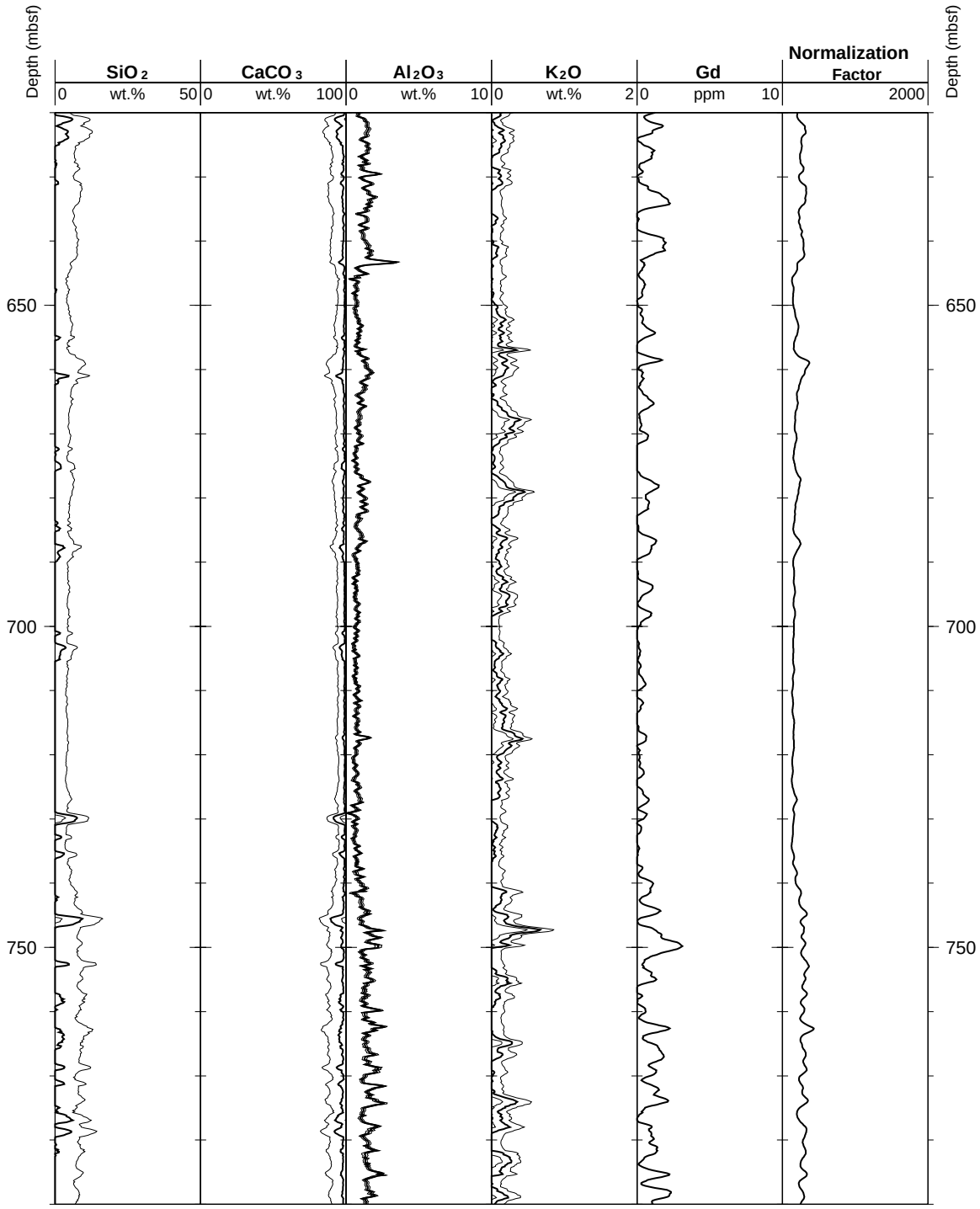

Hole 1003D: Geochemical Logging Data (cont.)

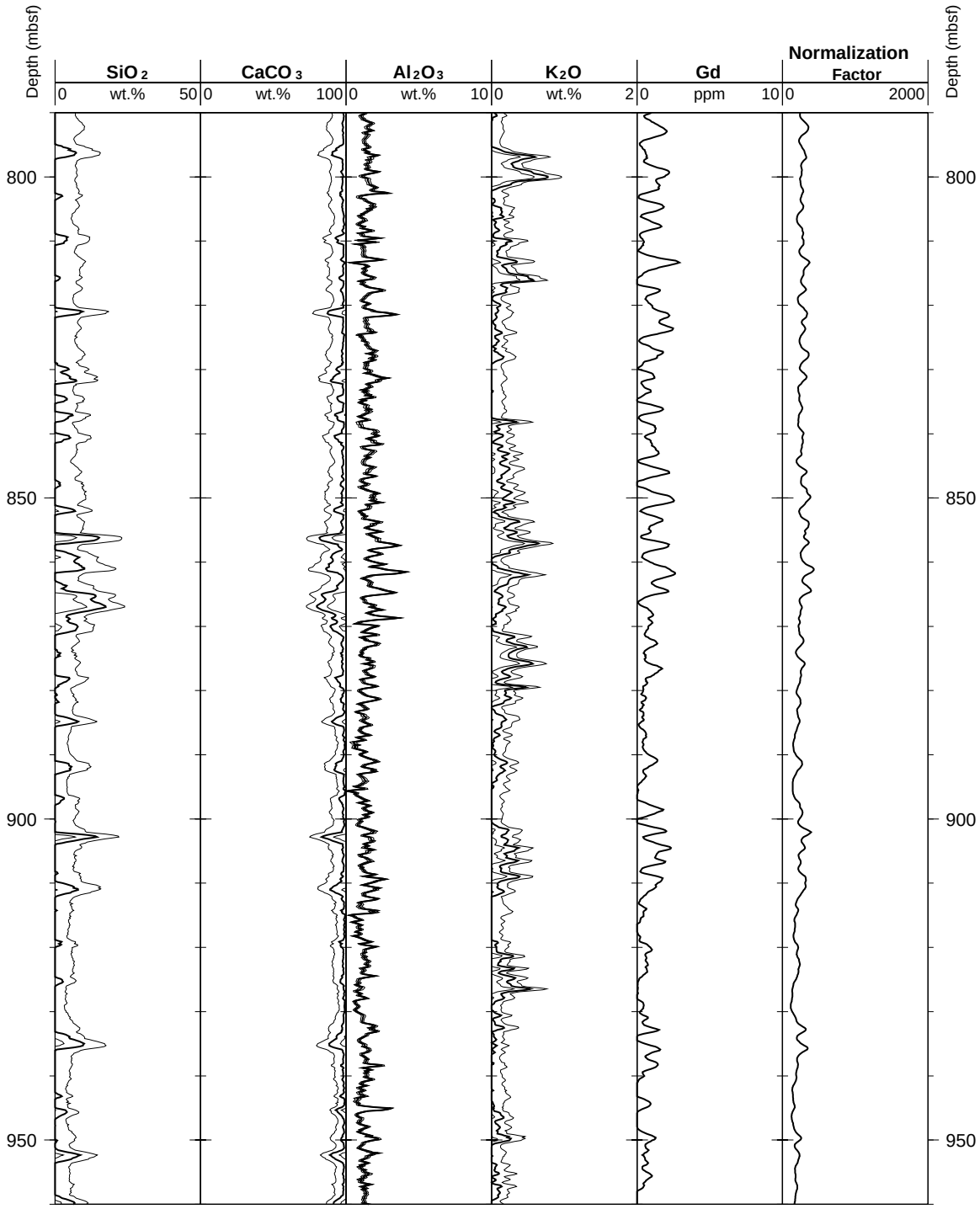

Hole 1003D: Geochemical Logging Data (cont.)

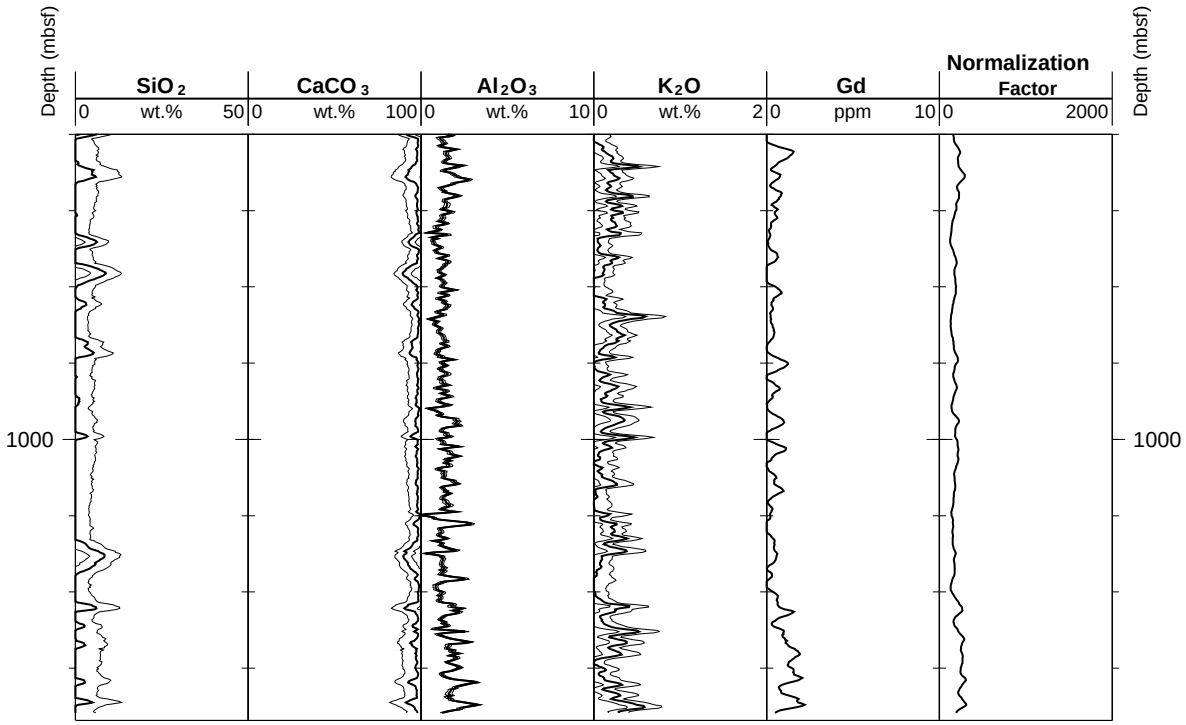

Hole 1003D: Natural Gamma Ray Logging Data

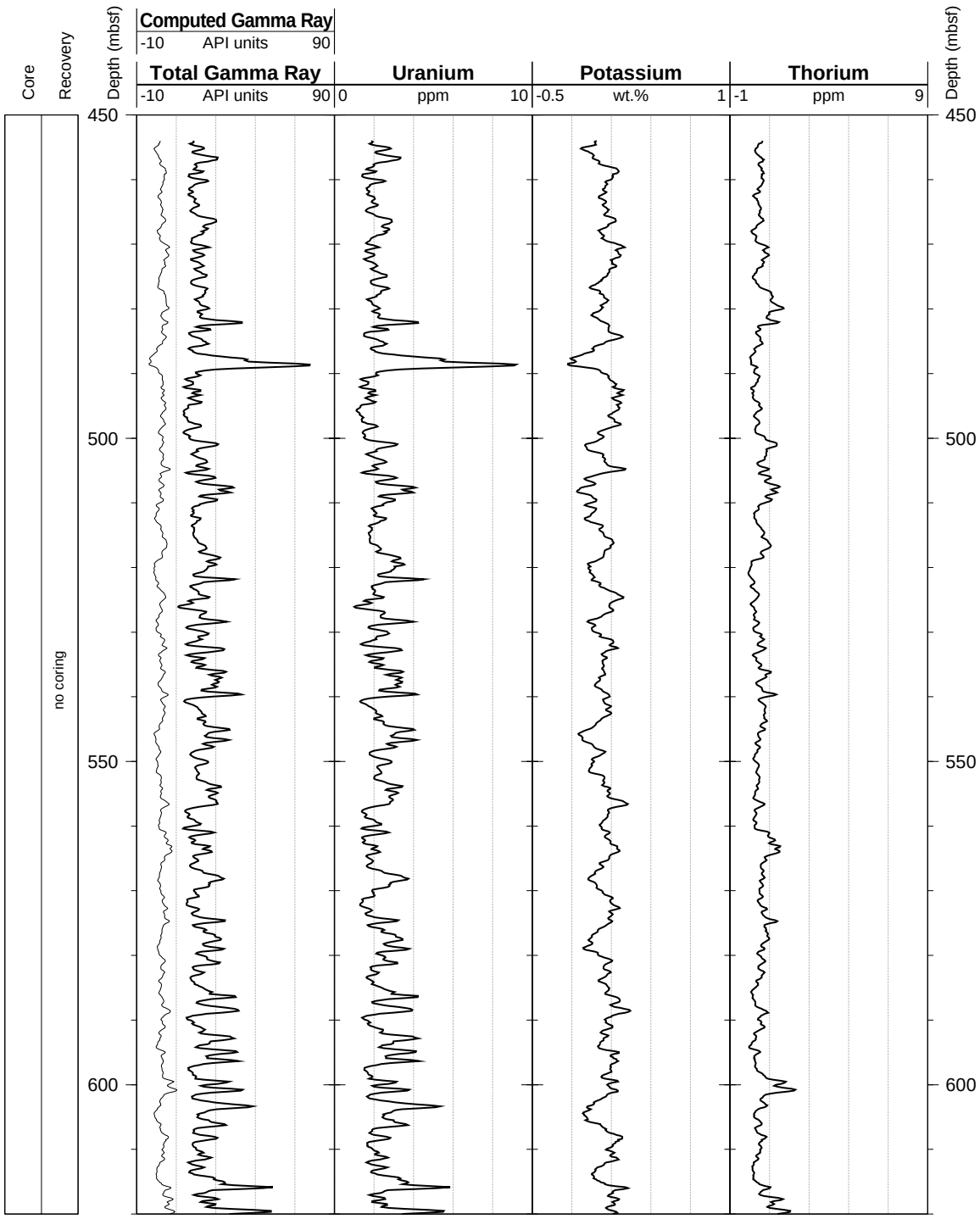

Hole 1003D: Natural Gamma Ray Logging Data (cont.)

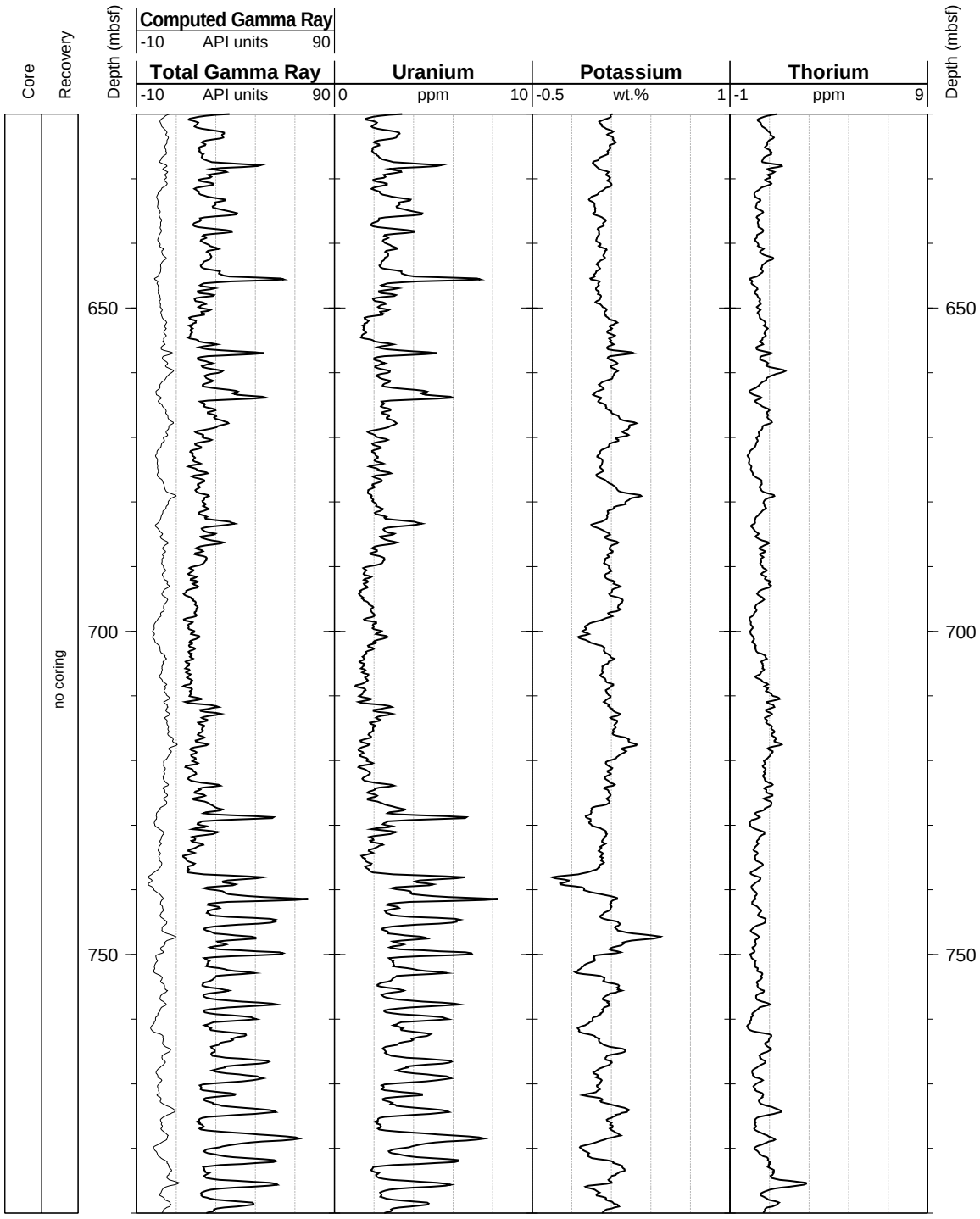

Hole 1003D: Natural Gamma Ray Logging Data (cont.)

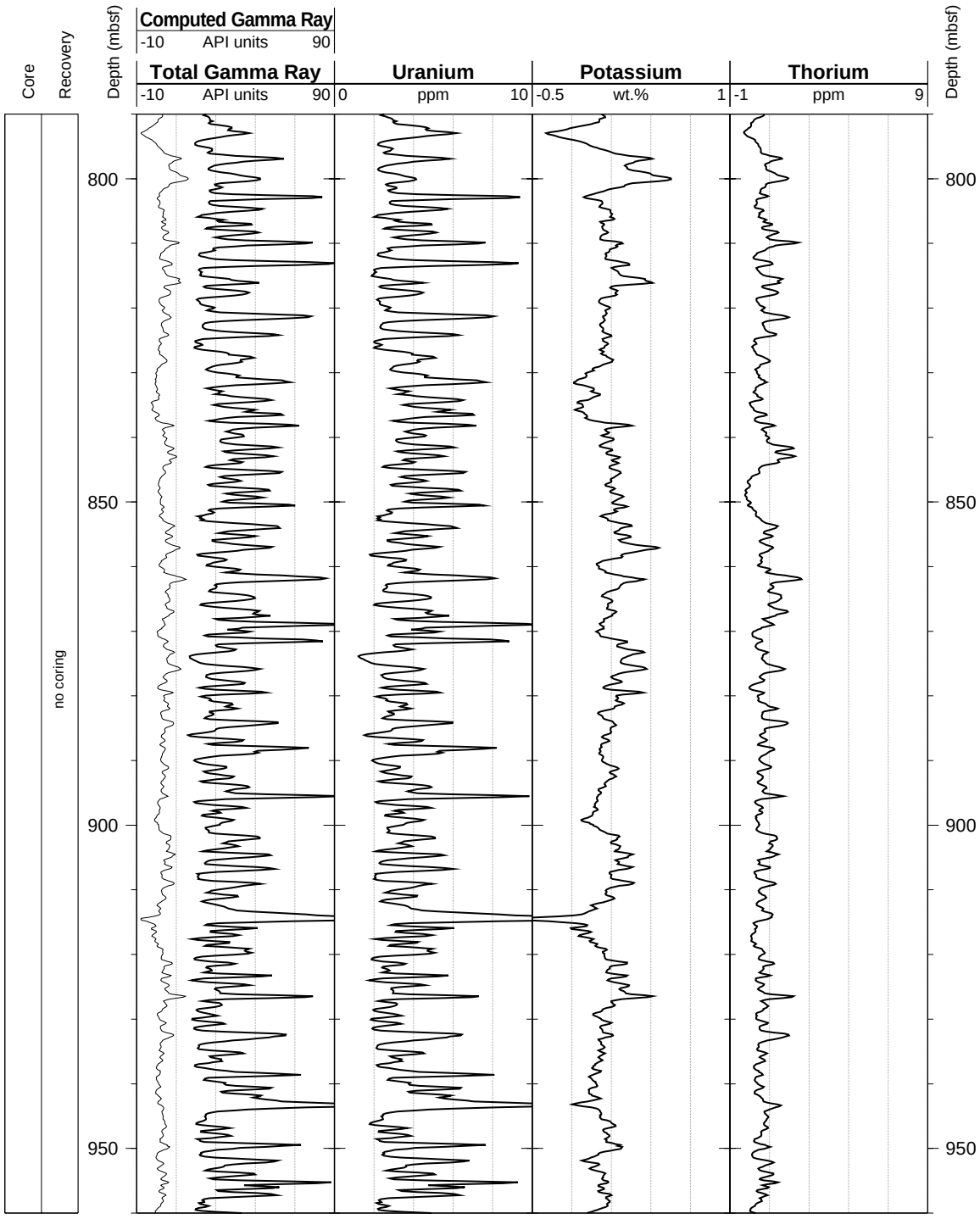

Hole 1003D: Natural Gamma Ray Logging Data (cont.)

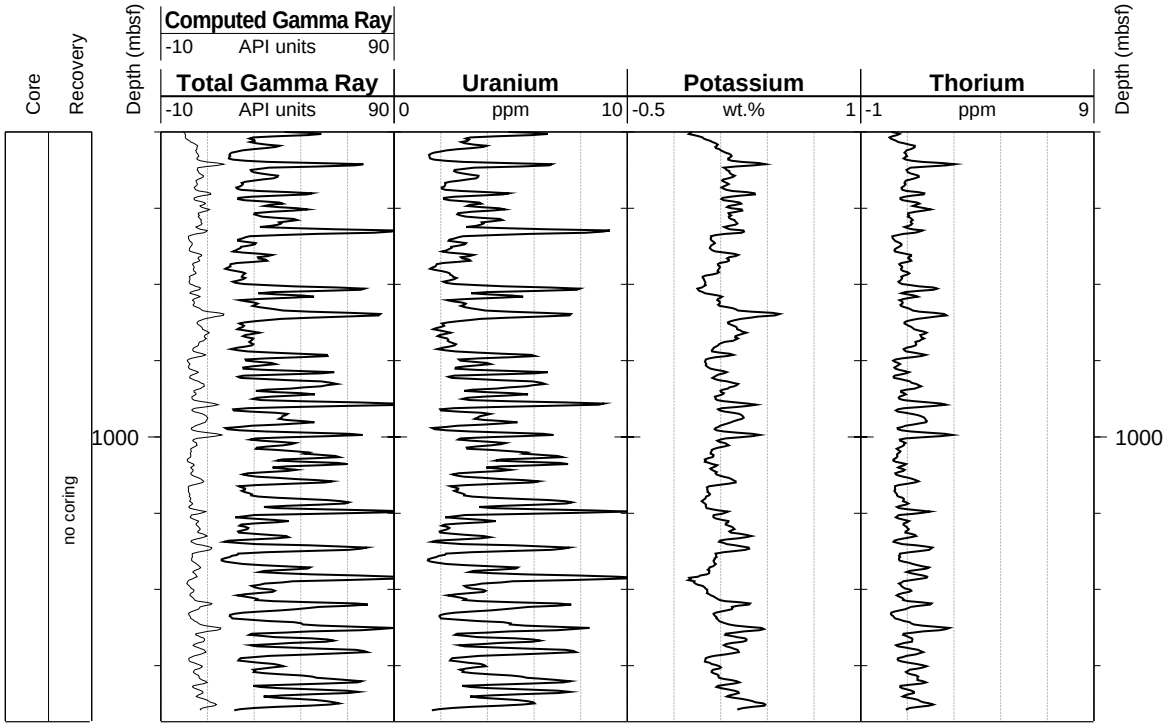

Previous Chapter Table of Contents Next Chapter